WAVE PROPAGATION IN 2D ELASTIC PERIODIC MATERIALS: THEORETICAL AND COMPUTATIONAL ANALYSIS

Camilo Valencia

Advisor:
Prof. Juan David Gomez

A thesis submitted for the degree of Doctor of Philosophy

October 29, 2019

... to Isnelia, Mario and Lina

Acknowledgements

Firstly, I would like to express my sincere gratitude to my advisor Prof. Juan David Gómez for the continuous support of my Ph.D study. During the time working with him, I learned vast technical and personal lessons. Thank you.

Besides my advisor, I would like to thank the rest of my thesis committee: Professors Juan Diego Jaramillo, Alexander Ossa and David Restrepo; for their insightful comments and encouragement. I want to specially thank Juan Diego Jaramillo and David Restrepo, who where involved in this work from an early stage.

Also, I thank Prof. Pablo D. Zavattieri for allowing me to stay at his lab, at Purdue University, during my research visit.

A very special gratitude goes to Colciencias, Universidad EAFIT and Fulbrigth for helping and providing the funding for this work.

I thank my fellow labmates César, Nicolás and Mauricio for the stimulating discussions and for all the fun we have had in the last years.

I would like to thank my family: my parents Mario and Isnelia, my brother Alejo and my lovely nephews Thomas and Ismael. Thank you for supporting me emotionally throughout writing this thesis and in my life in general.

Last and most important, I want to thank my wife Lina. Thank you for being always there during these Ph.D years and for being the main support of my life in every aspect.

Contents

Abstract

During the past 20 years the material science community has seen a tremendous growth in the development of metamaterials. These correspond to man made designed materials which, by virtue of its micro-structure, exhibit exotic effective properties and apparently not available in nature. The common feature, and at the heart of a metamaterial design, is the spatial repetition of a motif which eventually controls its effective behavior. Such spatial periodicity immediately brings Bloch's theorem from solid state physics as the fundamental analysis tool. The application of this theorem allows, in a very economic way, the identification of potential wave propagation modes and directional behavior of the material at the macro-scale. Unfortunately, the false power behind modern numerical methods has promoted an indiscriminate use of computational techniques in the study of periodic materials thus slowing down the development of new designs as new and more difficult challenges arise. This work reviews the fundamental theoretical aspects of Bloch analysis, and with the aid of in-house numerical tools, develops conceptual understanding regarding the response of periodic cellular materials in order to facilitate its future application in emerging fields. To show the effectiveness behind this rational approach these concepts are applied in the study of a novel multi-stable periodic material available in the literature. The work concludes with some ideas, rooted in the simple beam theory from strength of materials which are intended to pave the way to the future study of wave propagation in periodic materials.

Keywords:

Periodic materials, Bloch analysis, User element subroutine, Directional behavior analysis, Timoshenko beams.

Preface

This document summarises the work on wave propagation in periodic media held during some years of research. The main motivation to make the work presented here was to understand the unseen concepts under the analysis of periodic structures. Since the analysis of periodic materials is made through numerical tools, a wide range of problems can be solved. Also, with the high computational resources available nowadays, results can be obtained in reasonably short machine times. These two features about the analysis of periodic materials make it an appealing research area. For instance, if a periodic material with specific dynamical properties are required, one could find a periodic structure that matches those properties by trying hundreds of unit cells, combining different material properties and geometries. At the same time, this ease to get results can be dangerous since the physical phenomena behind the dispersive behavior of a periodic material are not clearly understood. Having that in mind we decided to make an effort to understand Bloch analysis as best as we could. First, we developed a computational tool to analyse periodic materials; such a tool uses a strategy that is general enough to consider any spatial dimension or physical context. Next, we took simple periodic structures, like an infinite unsupported beam, in order to deeply analyse their wave propagation behavior. The results from simple cases, allowed us to understand and predict the results from more complex structures. This work does not contain rare periodic materials or highly computational complex analyses. It contains very simple cases analysed from a conceptual and rational approach.

This document is structured in 5 chapters. Chapter 1 talks about the general aspects regarding Bloch analysis. The objective of this chapter is to explain theoretical and practical concepts about wave propagation in periodic media in a simple way. It covers from the formulation of Bloch's theorem to its usage on some simple geometries. Chapter 2 presents a strategy to implement Bloch analysis using user element subroutines. As it will be shown later, the implementation of Bloch-related problems in commercial finite element packages pose a series of challenges to be solved. The proposed strategy deals with such challenges with a simple procedure to apply Bloch boundary conditions by modifying the assemblage procedure in classic finite element analysis. Chapter 3 proposes a new metrics to compute the directional behavior of periodic materials, which is a measure of the preferred propagation paths of waves when propagating through the material. Chapter 4 presents a practical case of study. The concepts and numerical tools developed in previous chapters are now applied to the analysis of a bi-stable compliant mechanism. The analysis of such mechanism revealed that its dispersive behavior

is independent of the stability position. Some structural components are modified in order to change the mechanism's dispersive behavior. Chapter 5 is a conceptual study of simple two dimensional periodic structures. Some key concepts of periodic structures –like modulation of group speed and appearance of band gaps– are studied using a Timoskenko beam model. The simplicity of a beam model permits to study the phenomenon of dispersion in a clean and analytical way. After studying a single beam, the acquired concepts are applied to more complex structures made of beams and to solid domains under a plain strain idealization. This conceptual analysis finally conduces to a closed-form expression that allows the tuning of a band gap in a predefined design frequency. The main objective of chapter 5 is to explore a rational way to study periodic materials. Several of the ideas exposed in that study require further work and analysis. Finally, the last part of the document encloses all the previous chapters by presenting a general conclusion about this work and gives some insights about future work.

In this document, every chapter has an introduction which is intended to put the reader in context. Sometimes, a short literature review is included depending on the topics covered by the chapter at hand. At the end of each chapter (except chapter 1) there are some specific concluding remarks. The idea is that each chapter can be read independently. They can be thought as independent papers, which are "sewed" to the main document thanks to their introduction and conclusion sections.

Chapter 1

Bloch analysis

Introduction

Periodic materials either in the form of composites, like in the so-called phononic crystals, or those in the more exotic family of metamaterials, have received much attention during the recent years thanks to their various attractive features across different disciplines (Banerjee, 2011). These artificial materials are designed to meet specific functionalities through modifications at the microstructural level thus allowing effective macroscopic responses non-present in nature. Among the most interesting responses one finds, negative mass density, negative refraction, and electromagnetic cloaking (Hussein et al., 2014a; Goldsberry & Haberman, 2018; Norris & Haberman, 2012a), while particular applications are identified in the works of Hiett et al. (2002) in photonic crystals, Porter & Porter (2003) in micro-structured soils and Michel et al. (1999) in composite materials. A particular instance of metamaterials are the so-called periodic materials, which can be characterized through the use of Bloch's theorem, (Bloch, 1929).

Bloch analysis was originally used at atomic scale in solid state physics (Bloch, 1929; Brillouin, 1953; Kittel et al., 1976). It takes advantage of the ordered arrangement of atoms as described by crystal structures; so that, free waves travelling through an infinite material can be characterized by analysing only one crystal. Due to the generality of Bloch's theorem, its use has been extended to elastodynamics. In this context, it is used to analyse general periodic structures, even in the scale of large engineering systems Hussein et al. (2014a); Sigalas & Economou (1992).

Perhaps the most useful concept when studying periodic materials is that of the band structure; a diagram that represents a relation between frequency (or energy) and wave number along multiple directions in the material. In elastodynamics, the band diagram is a representation of the dispersion relation describing the nature of free wave propagation in an elastic (or acoustic) medium (Hussein et al., 2014a). The band diagram of a material has essential information like the energy distribution of waves in different directions of propagation; or the ranges of frequency where propagation is forbidden in one or more directions.

This chapter aims at explaining fundamental concepts of wave propagation in periodic media in simple terms. It covers some theoretical concepts about Bloch analysis and explains how to read and interpret a band or structure diagram. The chapter concludes with the dispersion results for some unit cells.

1.1 Wave propagation in periodic media

A periodic material is defined as the repetition of a given motif in one, two or three space dimensions. This motif refers to heterogeneities at the micro-structural level and it may contain several materials and geometric features. Figure 1.1(a)-(c) show a three dimensional material with periodicity in one, two and three dimensions. Such periodic materials are completely described by a lattice and an elementary unit, termed *elementary or unit cell*. The lattice is defined by a set of *base vectors* (fig. 1.1(d)), which allow construction of the whole material through successive applications of translation operations of the unit cell (Brillouin, 1953).

The occurrence of band gaps in periodic materials is controlled by two fundamental mechanisms. Brag scattering, appearing when the wavelength λ of the propagating field assumes values close to the characteristic size of the material miscroscructure, and by local resonance induced by the combination of materials with strong impedance contrasts (Hussein et al., 2014a). The intrinsic periodicity of the material facilitates the characterization in terms of its dispersion relationships or band structure through Bloch's theorem as stated in Brillouin (1953) and discussed next.

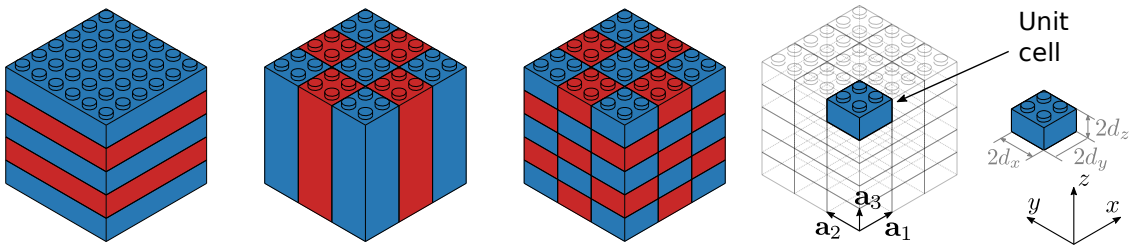

Figure 1.1. 3D periodic material with different periodicities. Even though a material can be three dimensional, its periodicity could be (a) one, (b) two or (c) three dimensional. (d) Definition of the unit cell of a periodic material. The material is constructed applying translation operations to the unit cell following the lattice vector **a**.

1.1.1 Bloch's Theorem

Let us consider a generalized (reduced) wave equation in the frequency domain

$$\mathcal{L}\mathbf{u}(\mathbf{x}) = -\rho\omega^2\mathbf{u}(\mathbf{x})\,, \tag{1.1}$$

valid for a given field $\mathbf{u}$ at a spatial point $\mathbf{x}$ and where $\mathcal{L}$ is a positive definite differential operator (Reddy, 1986; Kreyszig, 1978; Johnson, 2010), while ρ is the mass density and ω the corresponding angular frequency. Bloch's theorem from solid state physics (Brillouin, 1953) establishes that a solution to eq. (1.1) is of the form

$$\mathbf{u}(\mathbf{x}) = \mathbf{w}(\mathbf{x})e^{i\mathbf{k}\cdot\mathbf{x}}\,, \tag{1.2}$$

where $\mathbf{w}(\mathbf{x})$ is a Bloch function carrying with it the same periodicity of the material. Since the spatial period in $\mathbf{w}(\mathbf{x})$ is the lattice parameter $\mathbf{a}$, it follows that

$$\mathbf{w}(\mathbf{x}+\mathbf{a}) = \mathbf{w}(\mathbf{x}).$$

Accordingly, 1.2 is the product of a spatially periodic function $\mathbf{w}(\mathbf{x})$, with the periodicity of the lattice, and a plane wave (of wave vector $\mathbf{k}$), which is also periodic. As a result, field variables $\mathbf{\Phi}$ at opposite sides of the unit cell and separated by the lattice vector $\mathbf{a}$ are related through

$$\mathbf{\Phi}(\mathbf{x}+\mathbf{a}) = \mathbf{\Phi}(\mathbf{x})e^{i\mathbf{k}\cdot\mathbf{a}}. \tag{1.3}$$

In this case, $\mathbf{\Phi}$ refers to the principal variable involved in the physical problem, or to any of its spatial derivatives. From a physical point of view, eq. (1.3) means that a field variable $\mathbf{\Phi}$ at points $\mathbf{x}$ and $\mathbf{x}+\mathbf{a}$ differ only by the phase shift $e^{i\mathbf{k}\cdot\mathbf{a}}$.

In the particular case in which $\mathcal{L}$ is of order 2, the generalized Boundary Value Problem (BVP) conisdering Bloch boundary conditions (BBCs) takes the form:

$$\mathcal{L}\mathbf{u}(\mathbf{x}) = -\rho\omega^2\mathbf{u}(\mathbf{x})\,, \tag{1.4a}$$
$$\mathbf{u}(\mathbf{x}+\mathbf{a}) = \mathbf{u}(\mathbf{x})e^{i\mathbf{k}\cdot\mathbf{a}}\,, \tag{1.4b}$$
$$\nabla\mathbf{u}(\mathbf{x}+\mathbf{a})\cdot\hat{\mathbf{n}} = -\nabla\mathbf{u}(\mathbf{x})\cdot\hat{\mathbf{n}}\,e^{i\mathbf{k}\cdot\mathbf{a}}\,, \tag{1.4c}$$

where $\mathbf{u}(\mathbf{x}+\mathbf{a})$ and $\mathbf{u}(\mathbf{x})$ give the field at $\mathbf{x}+\mathbf{a}$ and $\mathbf{x}$ respectively while $\mathbf{a} = \mathbf{a}_1 n_1 + \mathbf{a}_2 n_2 + \mathbf{a}_3 n_3$ is the lattice translation vector shown in fig. 1.1(d).

Note that the BVP encompassed by 1.4 simultaneously describes the space-time periodicity of the solutions in the cellular material. Time periodicity is present in the frequency-domain nature of the reduced wave equation, while space periodicity explicitly appears in the wave number representation of the boundary conditions. The periodic relationship between opposite sides of the fundamental cell, present in the boundary terms, allows characterization of the fundamental properties of the material with the analysis of a single cell. At the same time wave vector $\mathbf{k}$ in eq. (1.4) simultaneously describes: (i) the propagation direction of a plane wave traveling through

the unit cell and (ii) the spatial periodicity of the plane wave. In consequence, finding solutions to the Bloch BVP amounts to finding those $\omega - \mathbf{k}$ pairs satisfying 1.4 when $\mathbf{k}$ is varied in the dual Fourier based representation of the fundamental material cell. This dual space corresponds to the *reciprocal space* and since it carries with it the periodic character of the physical space it suffices to consider values (and directions) of $\mathbf{k}$ within this reciprocal space representation of the unit cell.

1.1.2 A simple one-dimensional periodic array

The fundamental idea behind Bloch analysis is now described with a simple discrete one-dimensional problem. Consider the periodic mass-spring system shown in fig. 1.2. The system is composed by infinite point masses m connected by springs with stiffness K.

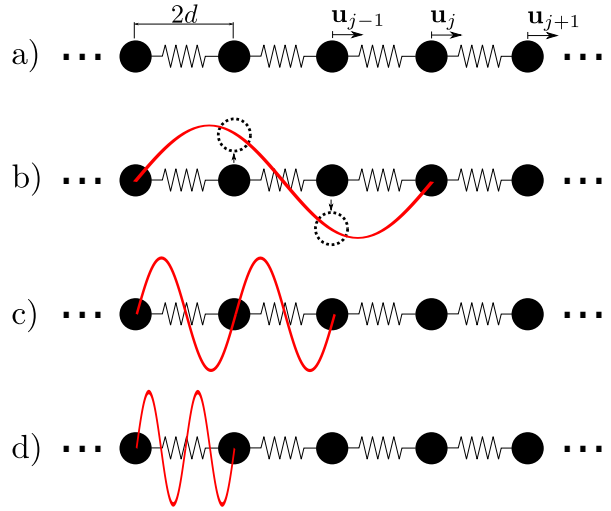

Figure 1.2. Example of 1D periodic structure and illustration of harmonic waves of different sizes propagating along the material. (a) Periodic array. (b) $\lambda > 2d$. (c) $\lambda = 2d$. (d) $\lambda < 2d$.

Assume that the fundamental cell encloses a typical mass j and its boundaries with masses $j-1$ and $j+1$. Since the inter-mass distance is $2d$ this is the cell parameter analogous to $\mathbf{a}$ in eq. (1.3). The equation of motion of the $j-$th mass reads

$$K(\mathbf{u}_{j+1} - \mathbf{u}_j) - K(\mathbf{u}_j - \mathbf{u}_{j-1}) = m\ddot{\mathbf{u}}_j \tag{1.5}$$

while its reduced frequency domain form is

$$K(\mathbf{u}_{j+1} - \mathbf{u}_j) - K(\mathbf{u}_j - \mathbf{u}_{j-1}) = \omega^2 m\ddot{\mathbf{u}}_j. \tag{1.6}$$

Bloch boundary conditions for the $j-$th mass follow from eq. (1.3):

$$\mathbf{u}_{j-1} = \mathbf{u}_j e^{-i2\mathbf{k}d}, \qquad \mathbf{u}_{j+1} = \mathbf{u}_j e^{i2\mathbf{k}d}. \tag{1.7}$$

Replacing these Bloch boundary conditions into eq. (1.6) leads, after some manipulations, to

$$\omega(\mathbf{k}) = 2\sqrt{\frac{K}{m}}|\sin(\mathbf{k}d)| \tag{1.8}$$

which is the dispersion relation or band structure of the one-dimensional periodic array. This ω vs $\mathbf{k}$ relationship contains all the information relevant to all the possible solutions to the equation of motion considering the periodic nature of the system.

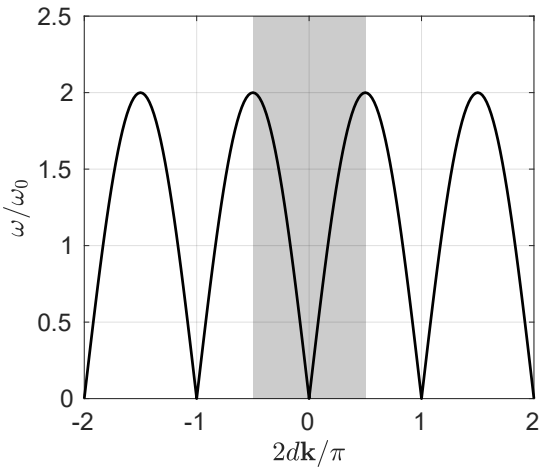

Figure 1.3. Dispersion relation of a mass-spring periodic array. $\omega_0 = \sqrt{K/m}$.

The dispersion relation is plotted in fig. 1.3. It shows ω as a periodic function of $\mathbf{k}$ with all the information of the dispersion relation being contained in the interval $\mathbf{k} = [-\pi/d, \pi/d]$. This is the *reciprocal space* or wave number domain representation of the unit cell which in the physical space lies in the range $\mathbf{k} = [-d, d]$. Furthermore, $\mathbf{k}$ can be restricted to the range $\|\mathbf{k}\| = [0, \pi/d]$ since positive and negative values of $\mathbf{k}$ mean waves propagating in opposite directions. The range $\|\mathbf{k}\| = [0, \pi/d]$ is equivalent to the range $\lambda = [2d, \infty]$ since $\lambda = 2\pi/\kappa$. This range of possible wavelengths implies that waves of length smaller than $2d$ do not appear in the specific material model. Furthermore, since the motion in the periodic array is controlled by the displacements of the different masses, a propagating wave with a wavelength smaller than the mass separation distance ($2d$) cannot be spatially described (see Figure 1.2b-d). It is evident that wave lengths $\lambda < 2d$ are not captured by the masses in the periodic array. The determination of the limit values of $\mathbf{k}$ is a topic of major importance in analysis of periodic structures, since it defines the domain of existence of the possible wave vectors in a periodic structure. This problem is the subject of the following section for the case of two-dimensional materials.

1.1.3 Domain of $\|\mathbf{k}\|$ in 2D periodic materials

This section describes the steps required in the determination of the reciprocal space description of the unit material cell. Since periodicity exists in both spaces, knowing such description of the unit cell is convenient as it reduces the space of search for valid wave vectors. Here, we first formalize the definition of the reciprocal space and then we show the proper and required restrictions for the values of $\|\mathbf{k}\|$.

Reciprocal space

Consider the Fourier expansion of the periodic Bloch function $\mathbf{w}(\mathbf{x})$ (Kittel et al., 1976)

$$\mathbf{w}(\mathbf{x}) = \sum_G \mathbf{w_G} \mathrm{e}^{i\mathbf{G}\cdot\mathbf{x}},$$

and where $\mathbf{G}$ is a set of vectors carrying with it the periodicity of $\mathbf{w}$ into the Fourier domain. Evaluation of $\mathbf{w}(\mathbf{x}+\mathbf{a})$ gives

$$\mathbf{w}(\mathbf{x}+\mathbf{a}) = \sum_G \mathbf{w_G} \mathrm{e}^{i\mathbf{G}\cdot\mathbf{x}} \mathrm{e}^{i\mathbf{G}\cdot\mathbf{a}}.$$

Since by definition $\mathbf{w}(\mathbf{x}+\mathbf{a}) = \mathbf{w}(\mathbf{x})$ the set of vectors $\mathbf{G}$ satisfy the condition $\mathrm{e}^{i\mathbf{G}\cdot\mathbf{a}} = 1$. $\mathbf{G}$ can be expressed as

$$\mathbf{G} = m_1\mathbf{b}_1 + m_2\mathbf{b}_2 + m_3\mathbf{b}_3,$$

in terms of a set of vectors $\mathbf{b}_i$ that satisfy the condition $\mathrm{e}^{i\mathbf{G}\cdot\mathbf{a}} = 1$, and are constructed according to (Kittel et al., 1976)

$$\mathbf{b_1} = 2\pi \frac{\mathbf{a_2}\times\mathbf{a_3}}{\mathbf{a_1}\cdot\mathbf{a_2}\times\mathbf{a_3}}, \qquad \mathbf{b_2} = 2\pi \frac{\mathbf{a_3}\times\mathbf{a_1}}{\mathbf{a_1}\cdot\mathbf{a_2}\times\mathbf{a_3}}, \qquad \mathbf{b_3} = 2\pi \frac{\mathbf{a_1}\times\mathbf{a_2}}{\mathbf{a_1}\cdot\mathbf{a_2}\times\mathbf{a_3}}. \tag{1.9}$$

The base vectors $\mathbf{b}_i$ existing in the spatial Fourier domain define the reciprocal lattice for the two-dimensional material. To further clarify note that while $\mathbf{a_i}$ are the primitive vectors for the physical lattice, $\mathbf{b}_i$ are the primitive vectors of the reciprocal lattice. Both sets of base vectors satisfy the condition

$$\mathbf{b}_i \cdot \mathbf{a}_j = 2\pi\delta_{ij},$$

where δ_{ij} is the Kronecker delta.

Restriction of $\|\mathbf{k}\|$ and the Brillouin zones

Bloch's theorem relates opposite sides of the unit cell. This can be used to establish a relation between the wave vector $\mathbf{k}$ and the primitive vectors of the reciprocal lattice $\mathbf{G}$ in terms of the Bragg or diffraction condition as (Kittel et al., 1976):

$$2\mathbf{k}\cdot\mathbf{G} = \|\mathbf{G}\|^2 \qquad \text{or} \qquad \mathbf{k}\cdot\frac{1}{2}\mathbf{G} = \left(\frac{1}{2}\|\mathbf{G}\|\right)^2 \tag{1.10}$$

which can be graphically understood with the aid of fig. 1.4b.

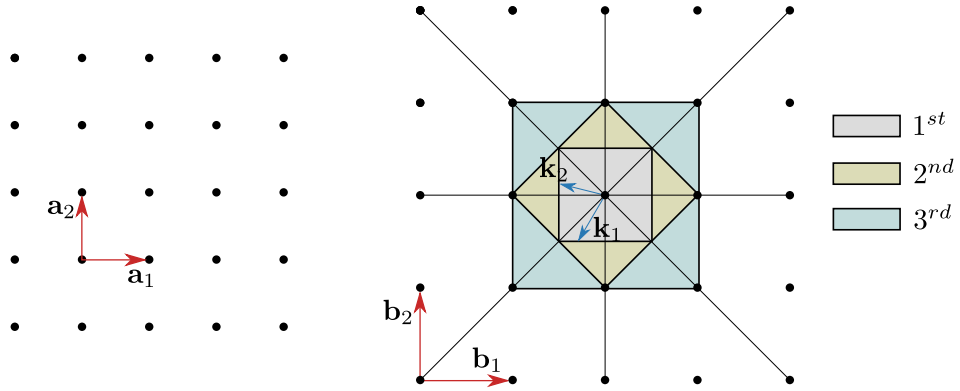

Figure 1.4. Schematic example of a 2D lattice in physical and reciprocal spaces. (a) Physical lattice showing the primitive vectors $\mathbf{a}_i$. (b) Reciprocal lattice showing the primitive vectors $\mathbf{b}_i$ and the first three Brillouin zones. The zones are constructed in the reciprocal space and they do not intersect. Each zone represents a set of wave vectors $\mathbf{k}$ that hold eq. (1.10). $\mathbf{k}_1$ and $\mathbf{k}_2$ are drawn as an example.

Select a point from the reciprocal lattice and draw vectors $\mathbf{G}$ to neighbor points. Draw a perpendicular bisector for each vector $\mathbf{G}$. The smallest closed area created by those bisectors is known as the First Brillouin Zone (FBZ). Every wave vector pointing to the border of the FBZ satisfies eq. (1.10). The additional Brillouin zones shown in fig. 1.4b are conformed by vectors $\mathbf{G}$ pointing beyond the FBZ. Although wave vectors pointing to the borders of those additional Brillouin zones equally satisfy eq. (1.10), they do not provide additional information as all the periodicity has already been captured by the FBZ. In summary, the limits of the FBZ define the values of $\|\mathbf{k}\|$ required to fully characterize the periodic material.

The irreducible Brillouin zone

Further reductions to the FBZ can be obtained after considering possible (rotation or mirror) symmetries. The resulting and smallest domain is now termed the Irreducible Brillouin Zone (IBZ). Such a zone in the reciprocal lattice contains all the necessary information concerning the wave number domain. Every point in the reciprocal lattice can be represented using the IBZ and the primitive reciprocal vectors $\mathbf{G}$. Figure 1.5 presents a series of 2D unit cells and their FBZ and IBZ where the FBZ is calculated using eqs. (1.9) and (1.10) for each cell.

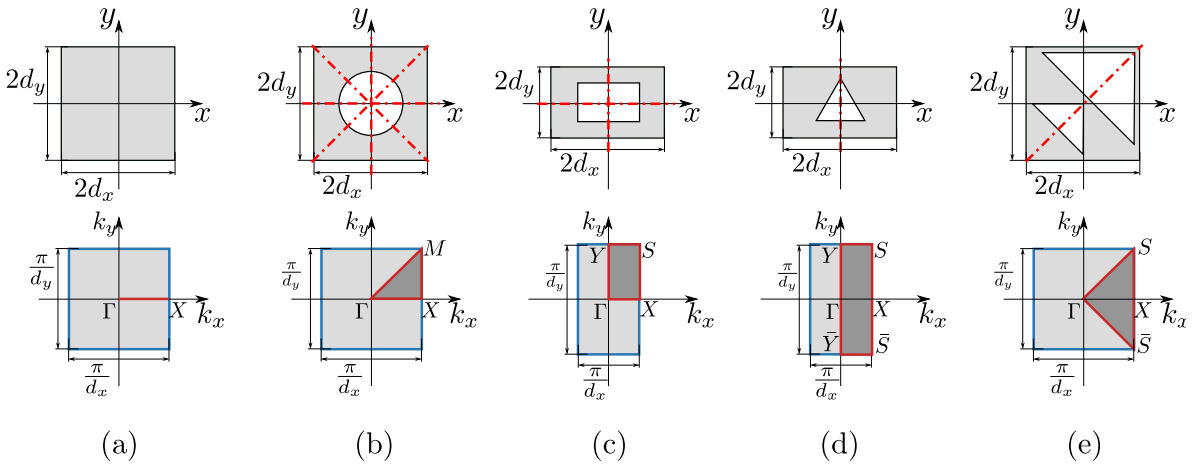

Figure 1.5. FBZ and IBZ for some 2D unit cells. The first row corresponds to the unit cells and their symmetry axes, depicted in dotted red lines. The second row shows the FBZ (region inside blue border) and IBZ (region inside red border) for each cell. Note that the exterior shape of the unit cell determines the shape of the FBZ; whereas a combination of exterior and interior shapes determine the shape of the IBZ. The corners of the IBZ are named after the notation used in solid state physics.

The reduction of FBZ to IBZ can be acomplished in different ways depending upon the existing symmetries. For instance, consider fig. 1.5a,b,e where the FBZ have the same shape while the IBZ is remarkable different due to the symmetries in each case. Figure 1.5a corresponds to the unit cell from a 2D homogeneous material; since it exhibits the same response in every direction, its IBZ reduces to a line in the reciprocal space. Furthermore, any straight line from the origin Γ to any point in the border of the FBZ is a valid IBZ in the homogeneous case. The IBZ has to be always carefully selected since a wrong IBZ can result in misleading conclusions as it skips essential dispersive information from the FBZ. A discussion about the implications of a well-chosen IBZ can be found in Maurin et al. (2018).

To take advantage of the symmetries it is a common practice to present the dispersion results just over the contour of the IBZ. Such practice assumes that the extreme points of the dispersion relations are always in that contour. In general, this assumption is true (Harrison et al., 2007) however there are specific cases in which those extreme points are at interior points of the FBZ (Craster et al., 2012; Maurin et al., 2018). There are two critical cases in which results along the contour of the IBZ are not reliable: (i) when the unit cell under study does not have too many symmetries, see fig. 1.5e; and (ii) when the selected unit cell is not the minimum possible unit cell, i.e., the primitive cell of the periodic material.

1.2 The band structure and its interpretation

The dispersion relation or band structure of a periodic material is a $\omega = \omega(\mathbf{k})$ relation that describes the behavior of waves when propagating through a periodic material. It is obtained after the application of Bloch's theorem to the reduced, frequency domain based equations of motion related to the kinematics and material model of the unit cell. As a reference example of a band structure, we considered a homogeneous material unit cell. The solution is shown along the FBZ and its reduced version along the contour of the IBZ.

1.2.1 A 2D homogeneous material unit cell

Valid unit cells for the homogeneous material model are shown in fig. 1.6. The current analysis considers a squared unit cell, fig. 1.5a.

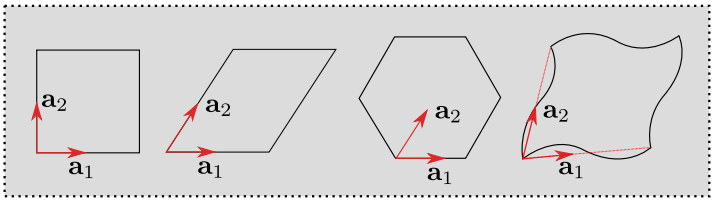

Figure 1.6. Some valid unit cells for a homogeneous material unit cell.

Dispersion relationships for the homogeneous material models can be written solely as closed-form frequency relationships with a functional dependence upon the magnitude of the wavenumber like

$$\omega \equiv \omega(\mathbf{k})\,.$$

However, when these relationships are obtained from direct application of Bloch's theorem the resulting relationships will also contain information from different Brillouin zones leading to more general expressions of the form:

$$\omega_{m,n} \equiv \omega(\mathbf{k}_{m,n})\,, \tag{1.11}$$

where the subscripts m, n refer to integer numbers related to waves coming from adjacent Brillouin zones. In the case of a square cell the following generalized definition of the wave number applies (Langlet, 1993):

$$\mathbf{k}_{m,n} = \sqrt{\left(k_x + \frac{m\pi}{d}\right)^2 + \left(k_y + \frac{n\pi}{d}\right)^2}$$

and where k_x and k_y are the horizontal and vertical normal components of the wave vector.

In classical elastodynamics, described separately in terms of out-of-plane (SH) waves and in-plane (P, SV) waves, the dispersion relations for a homogeneous material cell assume analogous linear forms in terms of phase speeds c_T and c_L given by:

$$\omega^{SH}_{m,n} = c_T \mathbf{k}_{m,n} \,, \tag{1.12a}$$
$$\omega^{P}_{m,n} = c_L \mathbf{k}_{m,n} \,, \tag{1.12b}$$
$$\omega^{SV}_{m,n} = c_T \mathbf{k}_{m,n} \,. \tag{1.12c}$$

where $c_T^2 = \mu/\rho$ and $c_L^2 = (\lambda + 2\mu)/\rho$ are the speeds of S and P waves respectively. In the above λ and μ are the first and second Lamé parameters, while ρ is the volumetric mass density. Making $m = n = 0$ in eq. (1.12), renders the dispersion relations for S and P waves in those of two cones, fig. 1.7.

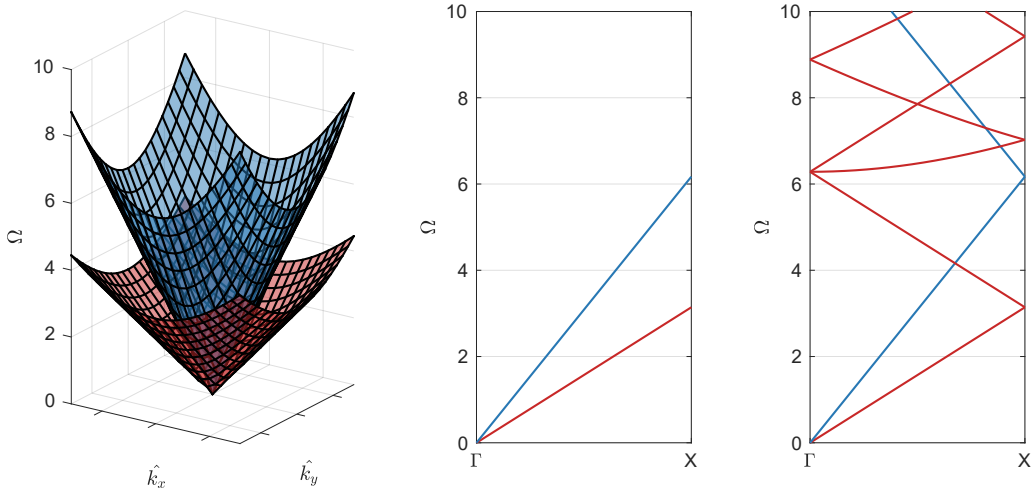

Figure 1.7. Dispersion relations for a homogeneous material unit cell. (a) Dispersion surfaces with $m = n = 0$ over the FBZ. (b) Dispersion curves with $m = n = 0$ along the IBZ. (c) Dispersion curves over the IBZ with various values of m and n.

Figure 1.7 presents the dispersion relations for a homogeneous material unit cell made of aluminium with $\lambda = 5.12 \times 10^{10}$Pa, $\mu = 2.76 \times 10^{10}$Pa and $\rho = 2770$kg/m^3. The frequency axes uses the dimensionless frequency $\Omega = 2\omega d/c_T$. Those dispersion relations can be presented over the FBZ (fig. 1.7a) as dispersion surfaces or just along the contour of the IBZ (fig. 1.7b-c) as dispersion curves. The red curves and surface correspond to S waves while the blue ones represent P waves. The curves are often easier to interpret and understand as they are a projection of the 3D dispersion surfaces. Note that fig. 1.7c contains several curves not present in fig. 1.7b. These must not be confused with additional waves propagating through the material but they correspond to dispersion information coming from adjacent unit cells.

Note that the IBZ for the homogeneous material unit cell is just a line (ΓX) in the FBZ. In most general cases, as shown in fig. 1.5, the IBZ is a region of the FBZ. In those cases, the dispersion curves are depicted along the contour of the IBZ and they look as those in fig. 1.8. The resulting dispersion diagrams are the unfolded curves of the intersection of dispersion surfaces and vertical planes. For this homogeneous material it is not necessary to depict the dispersion curves in a direction other than ΓX.

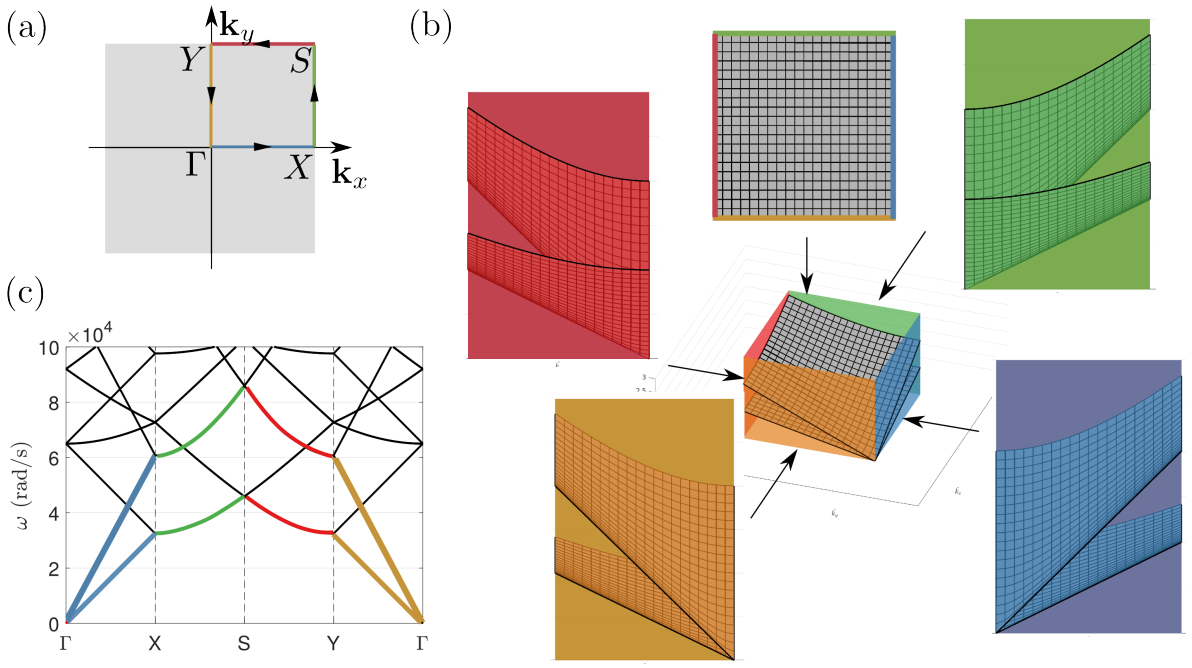

Figure 1.8. Example of the representation of dispersion curves along the contour of the IBZ and their counterpart in the dispersion surfaces. (a) IBZ following directions $\Gamma XSY\Gamma$ in the FBZ. (b) Dispersion surfaces in a section of the FBZ. (c) Dispersion curves. Each color (blue, green, red and yellow) covers an edge of the IBZ.

1.2.2 The inherent spatial aliasing in Bloch analysis

Figures 1.7c and 1.8c are examples of general dispersion curves. The first branches of these diagrams (coloured lines in fig. 1.8c) correspond to S and P waves. Figure 1.9 explains graphically the source of the extra branches in the band diagram. The central set of cones is the same as in fig. 1.7a, corresponding to S and P waves starting from $\Omega = 0$. Due to the spatial periodicity of the material, an equivalent set of cones is generated at every point of the reciprocal lattice, corresponding to adjacent cells. When these cones intersect the IBZ, they appear like straight lines or hyperbolas, depending on their original coordinates in the reciprocal space.

Since the reciprocal space results from the Fourier expansion of the Bloch function $\mathbf{w}(\mathbf{x})$, it unavoidably exhibits inherent spatial aliasing. This effect is reduced if the analyst effectively selects the smallest possible unit cell in the periodic material (Haque & Shim, 2016). When using numerical tools like the finite element method to find the band diagram of a material, results from the central unit cell and adjacent cells are

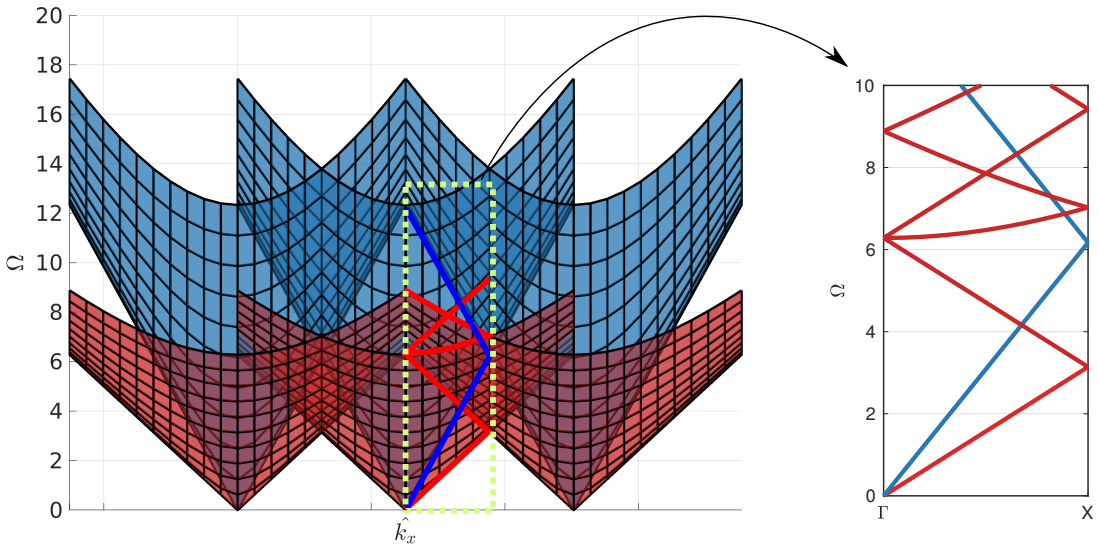

Figure 1.9. Graphical explanation of dispersion surfaces intercepting the IBZ in a homogeneous material. Left: extended wave number domain to show how information from adjacent cells gets into the FBZ. Right: Dispersion curves along the contour of the IBZ.

mixed (like in fig. 1.8c) and it is not possible to separate the actual and spurios (aliased generated) information.

1.2.3 Some dispersion curves for simple unit cells

Examples of typical features of band diagrams are shown in fig. 1.10. These results are for a bilayer and for a circular porous material cell. The bilayer material is conformed by aluminium and brass whereas the porous material has an aluminium matrix. The elastic properties for brass are $\lambda = 6.45\times10^{1}0\text{Pa}$, $\mu = 3.47\times10^{1}0\text{Pa}$ and $\rho = 8270\text{kg/m}^3$. Both models used plane strain assumptions. The dispersion diagrams in each case were computed via the finite elment method after varying the wave vector over the contour of the IBZ and finding the associated solving frequencies.

The regions of fig. 1.10a which are highlighted in blue represent gaps or stop bands in the diseprsion relation and correspond to frequency ranges where free waves are forbidden (i.e., are not allowed to propagate). The existence of band gaps makes periodic materials a very attractive option for a variety of engineering applications, since they behave as mechanical filters working at certain frequencies. On the other hand the dispersion relations in fig. 1.10 reveal a linear behavior for low frequency values ($\Omega < 2.0$) in both cases. This is a natural and expected result since very long waves do not interact with the microstructure of the unit cell but it propagates as in a homogeneous material at a constant speed. The linear response ceases at high frequencies, and the material behaves dispersively as the propagation velocity becomes frequency dependent. Results in the high frequency regime in fig. 1.10b are hard to interpret due, most of all, to the

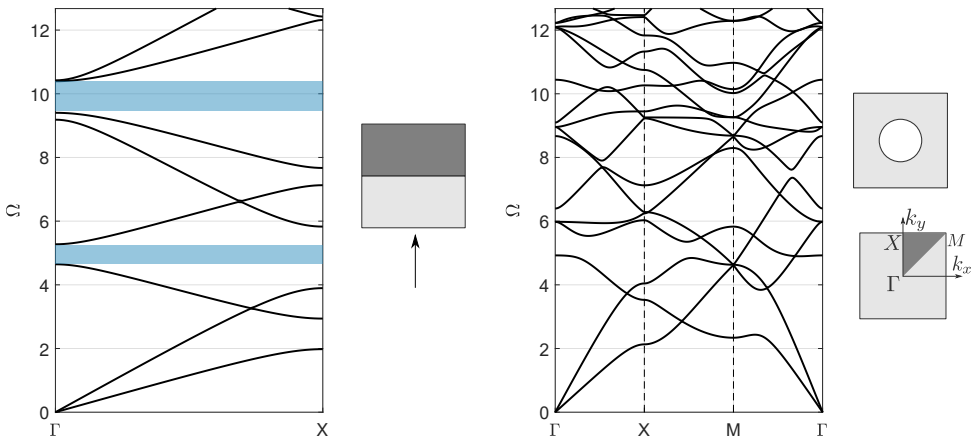

(a) (b)

Figure 1.10. Dispersion relations for some unit cells. (a) Bilayer material made with aluminium and brass. Each layer has a thickness $t = d$. The analysis was made considering only the direction in which the material is periodic. (b) Circular pore. In this case the diameter of the pore is half of the unit cell length.

aliasing of Bloch analysis.

Conclusion

The fundamental conceptual tools requiered in the analysis of periodic cellular materials have been presented starting with the definition of periodic materials and its basic mathematical framework. Within this context Bloch's theorem arises as the main theoretical artefact for the analysis of periodic media. The theorem combines space-time periodicity into frequency-wave number domain periodicity. The time periodic nature of the problem is considering by formulating the problem as reduced frequency domain boundary value problem, while the space periodicity is introduced through the boundary conditions which are relationships between oposite sides of a fundamental material element cell. Several conceptual aspects of solutions of the equivalent BVP are also discussed aimed at providing supporting information for the interpretation of dispersion diagrams descriptive of periodic materials.

Chapter 2

A novel user element subroutine to calculate dispersion relations of periodic materials

Introduction

There are several issues that must be solved when computing band diagrams or dispersion relationships for periodic media with commercially available finite element codes. First, the wide majority of general purpose finite element packages available in the market are not equipped with the intrinsic functionality required to conduct the so-called Bloch analysis. Secondly, the imposition of Bloch periodic boundary condition (henceforth referred to like BBCs), implies the modification of global coefficient matrices by transformation arrays (McGrath & Pyati, 1994) which perform row-column operations (McGrath & Pyati, 1996). Such access and manipulation of the global coefficient matrix, is not only cumbersome but also prohibited in most commercial packages. Here we propose a novel, yet simple technique to compute dispersion relations in periodic materials with commercial finite element codes with intrinsic user-element functionalities. The main distinguishing, and most appealing feature in our method is the fact that all manipulations are conducted directly at the element level thus allowing for the treatment of a wide variety of physical contexts and problem dimensions. The proposed approach is motivated by the work from Pask & Sterne (2005) who used a similar technique to solve one dimensional problems after transforming the differential equation not to consider Bloch's theorem but the simpler case of periodic boundary conditions. That idea was later extended by Sukumar & Pask (2009) who incorporated BBCs although in problems restricted to scalar fields. The method proposed in this work extends these ideas but it is valid for both, periodic and Bloch periodic boundary conditions, in addition to the possibility of considering general problems regardless of their dimensionality and kinematic assumptions. Thus it is valid for a wide variety of scalar and vector valued functions belonging to different physical contexts. Furthermore, the numerical consideration of Bloch's theorem in periodic media requires the

solution of a complex-valued eigenvalue problem which can be solved using a 2-mesh approach as proposed by Åberg & Gudmundson (1997) or through the direct implementation of the numerical scheme in a complex-algebra-based finite element code (Langlet et al., 1995). Our element-based procedure can be implemented in both formats.

This chapter contains two sections. Section 1 formally introduces the proposed strategy to apply BBCs directly into the local elemental-based arrays. In the second section we conduct several verification exercises intended to show the generality of the numerical tool. Particularly, we solved elastodynamic problems for classical and Cosserat or micropolar based materials. This last cases is intended to show the possibility of implementing different kinematic assumptions. We considered, scalar problems corresponding to out-of-plane waves and vector-valued problems for in-plane waves. Additionally we also conducted numerical exercises to test the sensitivity of the implementation to the cell-size. In the different verification problems considered we used analytic and numerical results reported in the literature. As a complement we also included a package of supplementary material consisting of: (i) a fully functional version of FEAPpv to calculate the dispersion relations from a periodic material and (ii) a document explaining the usage of this version of FEAPpv with an example of a homogeneous material unit cell.

2.1 Finite element formulation of Bloch analysis

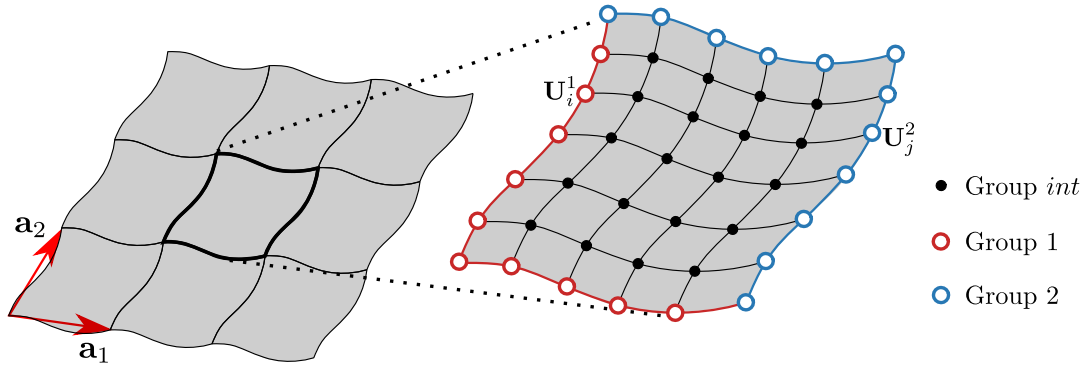

Figure 2.1. (a) Schematic 2D periodic material and its lattice translation vectors $\mathbf{a}_1$ and $\mathbf{a}_2$. (b) FE mesh from the unit cell and division in groups of nodes. Nodes in group 2 (blue) are equivalent to nodes in group 1 (red) in an adjacent unit cell. A pair of nodes are equivalent if their coordinates can be expressed as $\mathbf{x}_j^2 = \mathbf{x}_i^1 + m\mathbf{a}_1 + n\mathbf{a}_2$ for integers m and n.

Figure 2.1a shows an schematic representation of the unit cell in a periodic material. The corresponding finite element discretization of the BVP stated in eq. (1.4) as shown in the mesh in fig. 2.1b takes the form

$$\left[K - \omega^2 M\right] \{\mathbf{U}\} = \mathbf{0} \tag{2.1}$$

where in the context of elastodynamics, K and M would correspond to global stiffness and mass matrices respectively. Note that eq. (2.1) constitutes an eigenvalue problem in the eigenvalues ω. The schematic mesh contains also two different sets of nodal points corresponding to (i) interior nodes, labeled as *int*; and (ii) exterior nodes, labeled as 1 and 2. Nodes from groups 1 and 2 are represented in red and blue colors respectively. Imposition of Bloch periodic boundary conditions to the nodal sets 1 and 2 is dictated by the boundary conditions specified in eq. (1.4)b, (Guarín-Zapata & Gomez, 2014). In general, two equivalent nodes i, j in different adjacent cells can be related with the BBCs by

$$\mathbf{U}_j^2 = \mathbf{U}_i^1 \times \mathbf{PS}_{i\to j}, \tag{2.2}$$

where $\mathbf{U}_i^1$ is the field of node i belonging to group 1, $\mathbf{U}_j^2$ is the field of node j (equivalent to i in a different periodic cell) belonging to group 2, and $\mathbf{PS}_{i\to j}$ is the phase shift between the nodes i and j, with $\mathbf{PS}_{i\to j} = e^{i\mathbf{k}\cdot\mathbf{a}}$. The imposition of the BBCs to the complete system and the subsequent removal of redundant equations belonging to nodes in group 2, yields the reduced version of eq. (2.1) in terms of reduced matrices K_R and M_R as:

$$\left[K_R - \omega^2 M_R\right] \{\mathbf{U}_R\} = \mathbf{0} \quad . \tag{2.3}$$

The periodicity condition is ilustrated in fig. 2.2 for the periodic material displayed in the rectabgular domain. Periodicity along the vertical direction is equivalent to folding the rectangular sheet onto itself forming the cylender at the top. Similarly, considering also periodic variations in the horizontal direction converts the cylinder into a torus as shown in the right. Note that K_R and M_R in eq. (2.3) depend upon the wave vector $\mathbf{k}$. Accordingly, for a given $\mathbf{k}$ eq. (2.3) gives a particular instance of the eigenvalue problem. The band structure of the material is thus built after progressively covering the first Brillouin zone (Brillouin, 1953) in the wave-number domain representation of the unit cell. Each solution to the generalized eigenvalue problem given in eq. (2.3) represents a free wave propagating at frequency ω, moreover each corresponding solution gives all frequencies ω at which propagation of the specific free wave is possible and the dispersion relation ω vs $\mathbf{k}$ is then constructed.

2.1.1 Imposition BBCs in global matrices

Figure 2.3a shows a 4-bilinear-elements mesh corresponding to the discretization of a fundamental unit cell in a periodic material. The discrete equations from the general mesh are assembled into global stiffness and mass matrices K and M respectively as shown in the graphic description from fig. 2.3b and where each square section represents the sub-matrix associated to the set of degrees of freedom (DOF) at a specific node. In

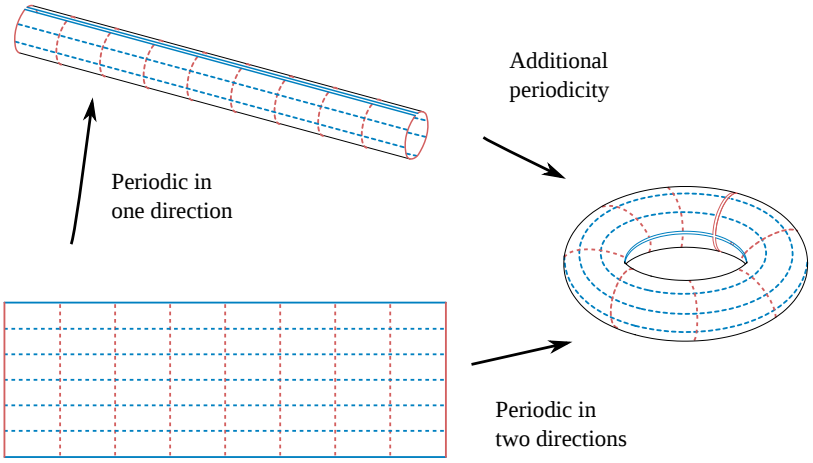

Figure 2.2. Topology for a rectangular region with periodicity in two directions. When periodicity in one direction is applied the mesh can be thought as laying on the surface of a cylinder. In the case of periodicity in two direction the mesh can be thought as laying on the surface of a torus.

this case, and just for illustration purposes, we assume 1-DOF per node as in a scalar problem so each element contributes to the global system with 4×4 global matrices G_M.

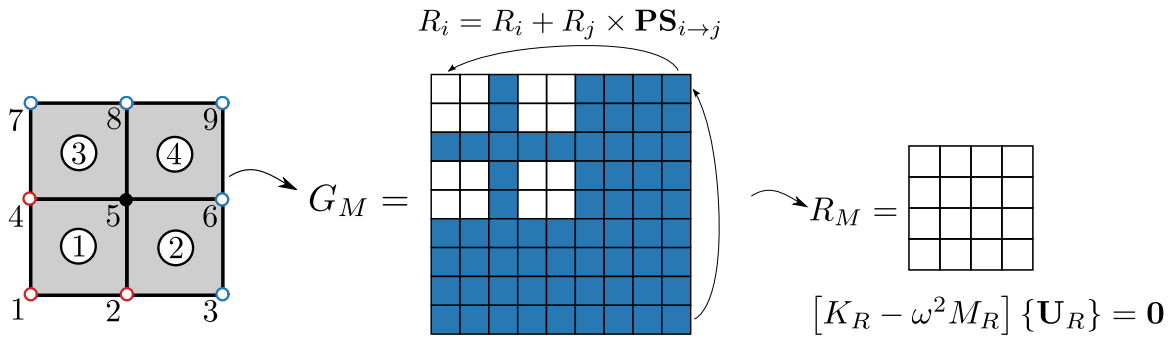

(a) Meshed unit cell

(b) Global matrix scheme

(c) Reduced matrix scheme

Figure 2.3. Schematic of the reduced eigenvalue problem after applying BBCs to the global matrices. The squares in the global matrix represent sub–matrices with equations from nodes in the mesh. After application of BBCs, blue squares collapse into the white squares. Namely, equations from nodes in group 2 collapse into equations from nodes in group 1. Finally, the redundant (blue) equations are removed from the matrices resulting in a reduced set of matrices.

Now, imposition of the required BBCs implies collapsing into a single equation those of nodes related as in eq. (2.2). For instance, nodes 9 and 1 at opossite corners of the unit cell satisfy:

$$R_1 = R_1 + R_9 \times \mathbf{PS}_{1\to 9}, \tag{2.4}$$

with R_n denoting a row (or a column) of sub-matrices in the general system G_M associated to node n. This means that equations from node 9 will collapse into those from node 1 after imposition of BBCs. Final application of BBCs to all relevant nodes trhough a process of removing redundant equations from K and M leads to reduced matrices K_R and M_R forming the generalized eigenvalue problem given in eq. (2.3). With reference to the schematic example of fig. 2.3 note that equations from nodes $3, 6, 7, 8, 9$ (blue squares in fig. 2.3b) were properly collapsed into those of nodes $1, 2, 4$ (white squares in fig. 2.3b) producing the reduced matrices in fig. 2.3c. This row-and-column operation scheme is widely used in Bloch analysis but it is difficult if not ipossible to apply in finite element codes that restrain access to the global coefficient matrices. Some available codes allow the manipulation to the global system as required in Bloch analysis through the imposition of Multi-Point constraints (Hibbett et al., 1998; Mazzoni et al., 2006). In these cases however, the analysis is restricted to the physical context available in the code.

2.2 Procedure to impose BBCs with user element subroutines

The implementation of Bloch analysis in commercial software, always require the manipulation of global arrays after the assemblage process; as shown in the previous chapter. The manipulation is normally carried out through row-and-column operations or transformation matrices. In this section we introduce our alternative method to implement BBCs as required in the analysis of periodic media. The proposed approach does not require access to the global arrays but it conducts all modifications at the element level. As such, the method is suitable for codes allowing the implementation of user element subroutines. In these codes, the main program acts as a solver of a system of equations where the user provides the contribution from each element to the global system. Here we take advantage of these features and instead of conducting the typical row-column operations leading to K_R and M_R onto the global arrays, we compute these matrices directly at the element level just by varying the standard assembly procedure available in FE codes.

2.2.1 Imposition BBCs in elemental matrices

Let us denote the set of connectivity nodes for a typical element m as C_m. Generally, C_m is used to carry out two tasks: (1) to define the coordinates of the nodes in element m which are required in the computation of elemental matrices; (2) to assemble these elemental matrices into the global arrays at positions defined by the equations' identifiers associated to these nodal points. In a classic FE problem, those two tasks are performed with the same nodal set C_m; however, in the case of periodic materials

with BBCs the assembly process proceeds differently. Here we define two kinds of connectivity operators corresponding to the classical coordinate-connectivity C_m^c, and an assemblage-connectivity set C_m^a. The first operator is used to compute the elemental matrices as in the standard approach while the second is used to conduct the assembly operation thus delivering global matrices where BBC have already been applied depending on the definition of C_m^a . In this approach, C_m^c and C_m^a are defined only for those elements containing nodes belonging to group 2 as described in fig. 2.1 while in the remaining elements, C_m^c and C_m^a are identical.

Consider element 2 in the mesh shown in fig. 2.3a. Due to the periodicityfor this specific cell, nodal pairs 6 and 4 and 3 and 1 are related by BBCs in such a way that in the global matrices, equations from node 6 will collapse into those from node 4, while equations from node 3 will collapse into equations from node 1. As a result, we define connectivity operators $C_2^c = [2\ 3\ 6\ 5]$ and $C_2^a = [2\ 1\ 4\ 5]$. This process must also incorporate the phase shifts corresponding to the impositions $\mathbf{PS}_{1\to3}$ and $\mathbf{PS}_{4\to6}$ to the equations of nodes 3 and 6 respectively in the local matrix. At the end of the procedure, equations from nodes in element 2 would have the proper phase shift and would be assembled in the proper global positions as pointed out by C_2^a. This process is explained graphically in fig. 2.4.

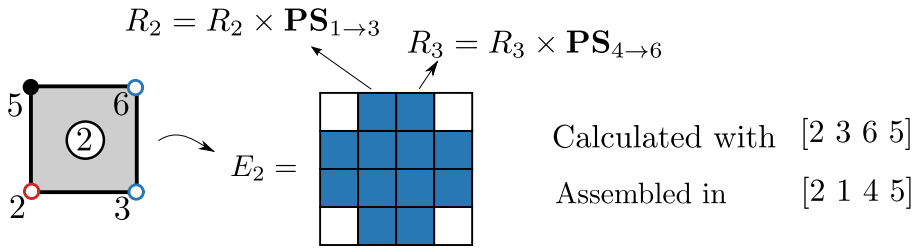

Figure 2.4. Application of BBCs to local matrices corresponding to element 2. Equations from nodes 3 and 6 are represented as blue sub-matrices and these include their proper phase shift and will be assembled in the positions dictated by $C_2^a = [2\ 1\ 4\ 5]$. The phase shifts are inferred locally from a comparison between assemblers C_2^a and C_2^m.

The next step in the assembly of the final global arrays is the elimination of redundant equations (in this case those in nodes 3, 6, 7, 8, 9) to obtain reduced arrays K_R and M_R. Here, this is achieved by restraining the degrees of freedom associated to these redundant equations. That process guarantees that K_R and M_R are assembled considering the required BBCs and that they are ready for solution of the generalized eigenvalue problem. Since this strategy to apply BBCs to a discretized unit cell proceeds at the element level and it is independent of the problem at hand, it can be straightforwardly used for one-, two- or three-dimensional periodic materials, using any kinematic model or interpolation scheme. Furthermore, it can be easily added to existing user element subroutines by making just subtle changes.

2.2.2 Reformulation in real algebra

An additional difficulty that appears often when conducting Bloch analysis with commercial finite element codes, is the fact that the resulting generalized eigenvalue problem given by eq. (2.3) is a complex-valued system. This is a consequence of the phase shifts of the general form $e^{i\mathbf{k}\cdot\mathbf{a}}$ explicitly appearing in BBCs. Most codes have powerful and efficient real-algebra-based built-in eigensolvers. To take advantage of these numerical features, we have followed Åberg & Gudmundson (1997), who split eq. (2.3) into two real problems as elaborated next.

Consider once again the 4-noded quadrilateral element showed in fig. 2.4 and repeated with additional information in fig. 2.5. Recall that nodal pairs 6 and 4 are related by $U_6 = U_4 \times \mathbf{PS}_{4\to6}$, with $\mathbf{PS}_{4\to6} = e^{i\mathbf{k}\cdot\mathbf{a}}$ and where U_6 and U_4 are the set of equations from nodes 6 and 4 respectively. These are complex valued terms which can be split like $U_\bullet = U_\bullet^R + iU_\bullet^I$, with $U_\bullet^R$ and $U_\bullet^I$ being respectively the real and imaginary components of U while $i = \sqrt{-1}$ is the imaginary unit. The original mesh can be interpreted now as a duplicated mesh where each part handles the real and imaginary component of the equations. This is explained in fig. 2.5, where we show the full-matrix E_2^A composed of the double consideration of the matrix E_2 like:

$$E_2^A = \begin{bmatrix} [E_2] & 0 \\ 0 & [E_2] \end{bmatrix}.$$

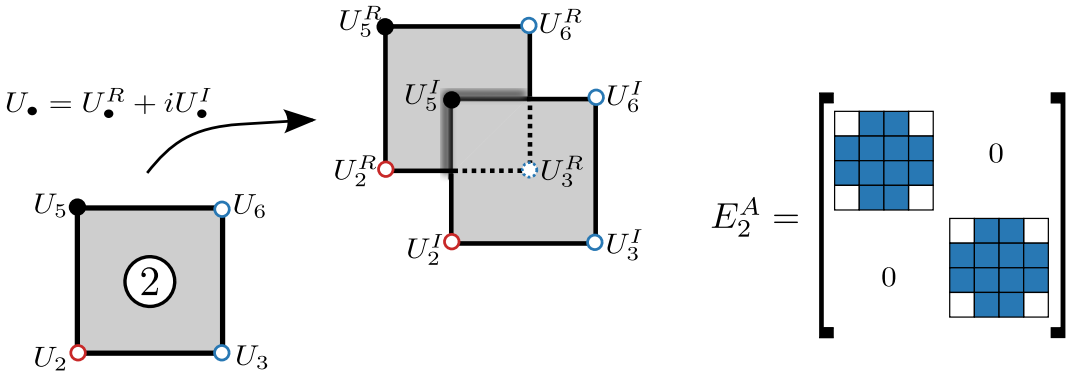

Figure 2.5. Application of BBCs to element 2 following the real algebra splitting proposed in Åberg & Gudmundson (1997). The equations from the element are separated into real and imaginary parts, producing an augmented elemental matrix. BBCs are then applied to both parts of the new matrix.

Consideration of all nodes in element 2 satisfying Bloch periodic boundary conditions, leads to a relation between real and imaginary meshes as stated by Åberg & Gudmund-

son (1997) and given by:

$$U_6^R = U_4^R \cos(\mathbf{k}\cdot\mathbf{a}) + U_4^I \sin(\mathbf{k}\cdot\mathbf{a}) \tag{2.5a}$$
$$U_6^I = U_4^I \cos(\mathbf{k}\cdot\mathbf{a}) - U_4^R \sin(\mathbf{k}\cdot\mathbf{a}) \tag{2.5b}$$
$$U_3^R = U_1^R \cos(\mathbf{k}\cdot\mathbf{a}) + U_1^I \sin(\mathbf{k}\cdot\mathbf{a}) \tag{2.5c}$$
$$U_3^I = U_1^I \cos(\mathbf{k}\cdot\mathbf{a}) - U_1^R \sin(\mathbf{k}\cdot\mathbf{a}) \tag{2.5d}$$

These sets of DOF modified by BBCs are represented in the schematic matrix representation of fig. 2.5 as sub-matrices in blue rows and columns. Those specific sub-matrices are to be assembled in the positions given by $C_2^a = [2\ 1\ 4\ 5]$. Note that although BBCs, like those in eq. (2.5) are just applied to local matrices from elements containing at least one node from group 2, the dual-mesh representation has to be applied for all elements in the mesh. According to the color scheme in fig. 2.5, local matrices from elements containing any node from group 2, have blue equations; while the rest of elements have white equations. The result is therefore a duplicated mesh where real and imaginary parts from BBCs are applied to both real and imaginary portions of the mesh. Figure 2.6 shows a schematic illustration of the separation process over a general mesh and the application of BBCs to the global terms of the mesh. The final assembly can be thought as corresponding to two identical superimposed meshes, where the blue border collapses into the red border. Finally, the positions from the blue border are removed from the global arrays as indicated previously.

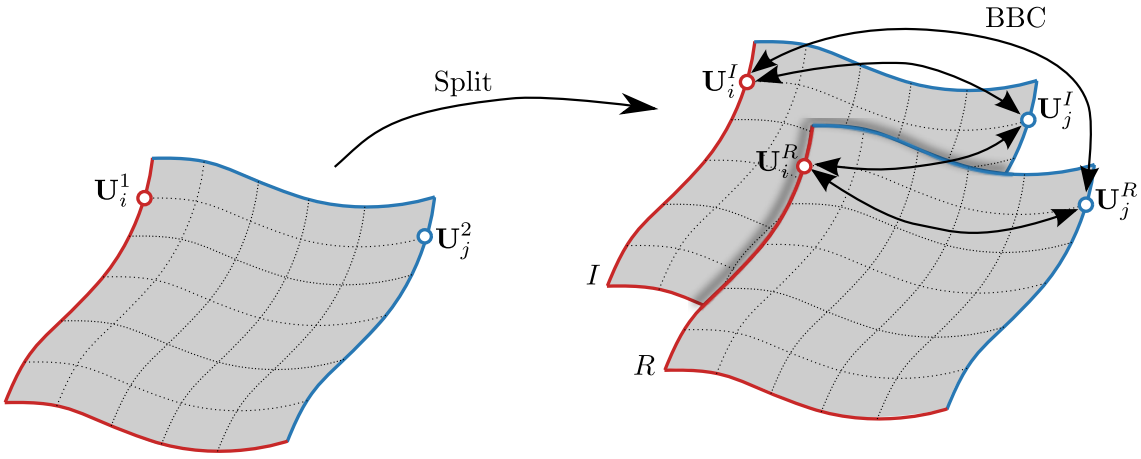

Figure 2.6. Schematic description of the splitting process. The mesh and BBCs are split into real and imaginary parts. These real and imaginary components from BBCs are then combined and applied to each part of the mesh following a procedure similar to the one in eq. (2.5) for every pair of related nodes. The new mesh can be thought as conformed by two identical meshes attached along the borders.

2.3 Verification

To test the generality of our implementation, we computed the dispersion relations in the context of elastodynamics for three classes of media with different kinematic assumptions. However, the proposed methodology to impose BBCs is independent of the physical context of the problem at hand and it can be equivalently applied to scalar problems (e.g., linear acoustics); quantum mechanics; or to vector problems (e.g., electrodynamics or elastodynamics). In the case of mechanical waves propagating in unbounded domains, the problem can be separated in 2 two-dimensional problems considering in-plane and out-of-plane wave polarization (Achenbach, 2012; Auld, 1973). In this study we consider waves propagating in the xy plane for the cases considered next.

Out-of-plane waves in elastic media: The simplest case corresponds to the out-of-plane horizontally polarized shear waves (or SH waves). These are governed by displacement equations of motion involving only the displacement in the z-direction u_z, with reduced wave equation of the form:

$$\frac{\mu}{\rho}\left[\frac{\partial^2 u_z}{\partial x^2}+\frac{\partial^2 u_z}{\partial y^2}\right]=-\omega^2 u_z\,,$$

where μ and ρ are: the second Lamé parameter (or shear modulus) and the volumetric mass density. These two are typically combined in terms of the squared phase speed $c_T^2=\mu/\rho$.

In-plane waves in elastic media: The vector displacement field in elastic media is completed considering in-plane polarization in terms of two degrees of freedom, corresponding to the horizontal and vertical components u_x and u_y at each material point. The wave motion in this case is described by the following specific form of the reduced wave equation:

$$\begin{aligned}
\frac{\lambda+2\mu}{\rho}\left[\frac{\partial^2 u_x}{\partial x^2}+\frac{\partial^2 u_y}{\partial y\partial x}\right]-\frac{\mu}{\rho}\left[\frac{\partial^2 u_y}{\partial y\partial x}-\frac{\partial^2 u_x}{\partial y^2}\right]&=-\omega^2 u_x\,,\\
\frac{\lambda+2\mu}{\rho}\left[\frac{\partial^2 u_x}{\partial y\partial x}+\frac{\partial^2 u_y}{\partial y^2}\right]-\frac{\mu}{\rho}\left[\frac{\partial^2 u_x}{\partial y\partial x}-\frac{\partial^2 u_y}{\partial x^2}\right]&=-\omega^2 u_y\,,
\end{aligned}$$

where now λ and μ are the first and second Lamé parameter respectively, while ρ is the volumetric mass density. These parameters are also typically combined into squared phase speeds $c_L^2=(\lambda+2\mu)/\rho$ and $c_T^2=\mu/\rho$ corresponding to two different wave modes.

In-plane waves in micropolar media: Micropolar media, inspired by contributions from Cosserat et al. (1909), correspond to a continuum model where each material

point is endowed with six degrees of freedom in the form of three displacements — as in classical elasticity — and three rotations. In this resulting micropolar elasticity theory the transmission of loads through surface elements, is now described by force and couple stress vectors. As a consequence of these additional kinematic interactions, waves in (homogeneous, isotropic) micropolar continua are inherently dispersive even in the absence of explicit micro-structural details. Under two-dimensional idealizations micropolar media is defined in terms of two displacements and one rotation leading to the following form of the reduced wave equation representative of the motion for such a class of media:

$$\begin{aligned}
&\frac{\lambda+2\mu}{\rho}\left[\frac{\partial^2 u_x}{\partial x^2}+\frac{\partial^2 u_y}{\partial y \partial x}\right]-\frac{\mu+\mu_c}{\rho}\left[\frac{\partial^2 u_y}{\partial y \partial x}-\frac{\partial^2 u_x}{\partial y^2}\right]+\frac{2\mu_c}{\rho}\frac{\partial \phi_z}{\partial y}=-\omega^2 u_x\,,\\
&\frac{\lambda+2\mu}{\rho}\left[\frac{\partial^2 u_x}{\partial y \partial x}+\frac{\partial^2 u_y}{\partial y^2}\right]-\frac{\mu+\mu_c}{\rho}\left[\frac{\partial^2 u_x}{\partial y \partial x}-\frac{\partial^2 u_y}{\partial x^2}\right]-\frac{2\mu_c}{\rho}\frac{\partial \phi_z}{\partial y}=-\omega^2 u_y\,,\\
&\frac{2\mu_c}{J}\left[\frac{\partial u_y}{\partial x}-\frac{\partial u_x}{\partial y}\right]+\frac{\xi}{J}\left[\frac{\partial^2 \phi_z}{\partial x^2}+\frac{\partial^2 \phi_z}{\partial y^2}\right]-\frac{4\mu_c}{J}\phi_z=-\omega^2 \phi_z\,,
\end{aligned}$$

and where in addition to the first and second Lamé parameters λ and μ from classical mechanics, there are also two new moduli μ_c and ξ with no classical counterparts. Also in these equations ρ and J are the volumetric and rotational mass density. Under this non-classical kinematic model there are three wave modes with a volumetric wave with phase speed $c_L^2=(\lambda+2\mu)/\rho$ and two dispersive modes with phase speeds that depend on the frequency (Nowacki, 1986).

All of the above kinematic models are particular instances of the generalized wave equation in the frequency domain. In this study, we take as base materials aluminum and brass with the following set of values for its mechanical properties:

	Material properties					
	λ (Pa)	μ (Pa)	ρ (kg/m^3)	μ_c (Pa)	ξ (N)	J (kg/m)
Aluminum	5.12×10^{10}	2.76×10^{10}	2770	3.07×10^{9}	7.66×10^{9}	306.5
Brass	6.45×10^{10}	3.47×10^{10}	8270	8.65×10^{9}	1.73×10^{9}	691.7

Table 2.1. Mechanical properties for the materials used in the verification study conducted to test the element-based approach to conduct Bloch analysis.

2.3.1 Test of generality about physics

The first set of analyses is aimed at testing the capabilities of our strategy to describe new waves appearing into the material as we increase the complexity of the kinematic model. The first problem is a comparison between numerical and analytical results for a homogeneous material unit cell. We computed the dispersion relations using the three different kinematic assumptions described previously, where in each case there are additional degrees of freedom added to the model.

Analytic dispersion relations for a homogeneous material

Dispersion relationships for the homogeneous material models can be written solely as frequency relationships with a functional dependence upon the magnitude of the wavenumber like

$$\omega \equiv \omega(k)\,.$$

However, when these relationships are obtained from Bloch's theorem the dispersion relationships also contain information from different Brillouin zones leading to more general relations of the form:

$$\omega_{m,n} \equiv \omega(k_{m,n})\,, \tag{2.6}$$

where the subscripts m, n correspond to integer numbers referring to waves coming from adjacent Brillouin zones. In the case of a square unit cell we have the following generalized definition of the wave number (Langlet, 1993):

$$k_{m,n} = \sqrt{\left(k_x + \frac{m\pi}{d}\right)^2 + \left(k_y + \frac{n\pi}{d}\right)^2} \tag{2.7}$$

where k_x and k_y are the horizontal and vertical normal components of the wave vector.

Classical elastodynamics: In classical elastodynamics, described separately in terms of out-of-plane SH waves and in-plane P, SV waves, the dispersion relations for a homogeneous material cell take the analogous linear forms in terms of phase speeds c_T and c_L as given by:

$$\begin{aligned}
\omega^{SH}_{m,n} &= c_T k_{m,n}\,,\\
\omega^{P}_{m,n} &= c_L k_{m,n}\,,\\
\omega^{SV}_{m,n} &= c_T k_{m,n}\,.
\end{aligned}$$

Micropolar elastodynamics: In this model, in addition to the P- and S-waves in-plane propagation modes there is also an in-plane transverse rotational wave (TR). Furthermore, in the micropolar model transverse S-waves are dispersive as can be seen in the following dispersion relations:

$$\begin{aligned}
\omega^{P}_{m,n} &= c_L k_{m,n}\,,\\
\omega^{S}_{m,n} &= \sqrt{\frac{A}{2} - \frac{1}{2}\sqrt{A^2 - 4B}}\,,\\
\omega^{TR}_{m,n} &= \sqrt{\frac{A}{2} + \frac{1}{2}\sqrt{A^2 - 4B}}\,,
\end{aligned}$$

with

$$A = 2Q^2 + (c_2^2 + c_4^2)k_{m,n}^2\,,$$
$$B = 2Q^2 c_2^2 k_{m,n}^2 - K^2 Q^2 k_{m,n}^2 + c_2^2 c_4^2 k_{m,n}^4\,,$$

and

$$c_2^2 = \frac{\mu + \mu_c}{\rho}, \quad c_4^2 = \frac{\xi}{J},$$
$$K^2 = \frac{2\alpha}{\rho}, \quad Q^2 = \frac{2\alpha}{J}\,.$$

Numerical results

To test the proposed strategy, we implemented the elemental-based approach for the kinematic models described previously into the finite element code FEAP (Taylor, 2011). The supplementary material of this work contains a complete version of the algorithm as a FEAPpv binary file together with a fully defined test problem. The files also include subroutines to read the required C_m^c and C_m^a operators and peripheral codes to cover the cell representation in the reciprocal wave number domain. All the dispersion graphs use the dimensionless frequency

$$\Omega = \frac{2\omega d}{c_T}\,, \tag{2.8}$$

for the vertical axis, where $2d$ is the dimension of the unit cell and $c_T^2 = \mu/\rho$ is the speed of the shear wave.

Figure 2.7 compares the closed-form dispersion relations with those obtained numerically with the user-element subroutine. Note that each dispersion plot contains an additional degree of freedom with respect to the previous model. This is evidenced by an increasing number of dispersion branches in the figure. In the SH model there is a single branch corresponding to the horizontally polarized shear wave. The model for the in-plane material cell has an additional branch corresponding to the longitudinal P mode with a larger phase speed. Finally, examination of the results for the micropolar cell not only show an expected third branch corresponding to the rotational wave, but they also reveal a dispersive shear wave mode. The microrotational wave, denoted as the TR-mode appears after the cut–off frequency $\Omega = 2$. This limited existence of the microrotational model implies that there is a (microrotational) band-gap in the range $0 < \Omega < 2$. This is an interesting feature of the micropolar model which introduces a micro-structural effect inherently contained into the kinematics of the model. This effect is triggered for wavelengths $\lambda > c_T/\Omega_0$, where Ω_0 is the cut-off frequency. As a final observation it is worth mentioning that the comparison between numerical and

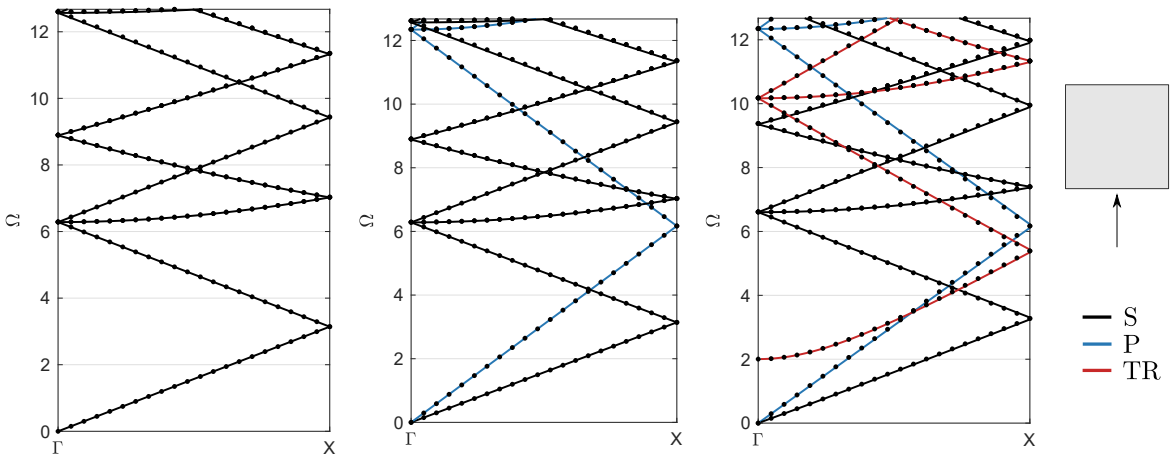

(a) Out-of-plane (b) In-plane (c) Micropolar

Figure 2.7. Dispersion relations for a homogeneous material with mechanical properties corresponding to aluminum as per table 2.1 under different kinematic models. Solid and dotted lines show the analytic and numerical solution respectively. In all cases the wave vector was assigned the particular value $\mathbf{k} = \langle 0, \kappa_y \rangle$.

the analytical results show a good agreement in every considered kinematic model, i.e., out-of-plane, in-plane and micropolar. Moreover, the maximum observed relative error between numerical and analytical results which occur near $\Omega = 12$ is less than 0.5%, which shows that the subroutine is suitable for computing dispersion relationships under different kinematic assumptions.

2.3.2 Test of generality about unit cell geometry and materials

As a second example to show the versatility of the proposed approach, we considered unit cells of different geometries and material properties. The first problem is that of a skewed unit cell made of a homogeneous material with properties corresponding to those of aluminum, as presented in fig. 2.8. This analysis was later extended to the case of a bi-layer material where we introduced brass in addition to an aluminum layer. For the in-plane kinematic assumptions both cases have closed-form solutions providing a useful basis to compare with numerical results.

The lattice vectors ($\mathbf{a}_i$) and reciprocal lattice vectors ($\mathbf{b}_i$) for the skewed unit cell are given by (Kittel et al., 1976):

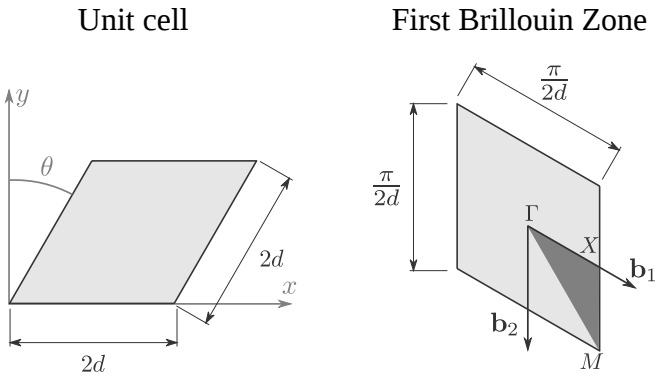

Figure 2.8. Unit cell (physical space) and first Brillouin zone (reciprocal space) for a skewed unit cell used to test the generality of the approach in modeling unit cells of different geometry.

$$\mathbf{a}_1 = 2d(1,0)\,, \quad \mathbf{a}_2 = 2d(\sin\theta, \cos\theta)\,,$$
$$\mathbf{b}_1 = \frac{\pi}{d}(1, -\tan\theta)\,, \quad \mathbf{b}_2 = \frac{\pi}{d}(0, \sec\theta)\,,$$

while the wavenumbers for the first Brillouin zone in the homogeneous material model read:

$$k_{m,n} = \sqrt{\left(k_x + \frac{m\pi}{d}\right)^2 + \left(k_y + \frac{m\pi\tan\theta}{d} + \frac{n\pi\sec\theta}{d}\right)^2}\,. \tag{2.9}$$

Similarly, the dispersion relations for the bi-layer material model under in-plane waves traveling perpendicularly to the layers is given by the following implicit equation (Langlet, 1993):

$$\cos(2dk) = \cos\left(\frac{\omega d}{c_1}\right)\cos\left(\frac{\omega d}{c_2}\right) - \frac{(\rho_1 c_1)^2 + (\rho_2 c_2)^2}{2\rho_1\rho_2 c_1 c_2}\sin\left(\frac{\omega d}{c_1}\right)\sin\left(\frac{\omega d}{c_2}\right)\,,$$

where c_i refers to the transverse or longitudinal wave of each layer, and ρ_i refers to the mass density of each layer.

Figures 2.9a and 2.9b show the results for the 2D homogeneous material under plane strain idealization computed with the squared and the skewed unit cell respectively. As shown in these plots, the results from the numerical implementation are in good agreement with those predicted by the closed-form dispersion relationships regardless of the geometry considered for the unit cell.Similarly, fig. 2.9c shows the results for the bi-layer material with vertical wave incidence (i.e., perpendicular to the layers). As indicated previously the material properties in each layer are those of aluminum and brass. From the dispersion diagrams, it is observed that in the low frequency regime ($\Omega < 1$), the bi-layered material behaves as a homogeneous material with a linear group velocity. This effective velocity is in fact an average between the wave propagation velocities of aluminum and brass. The results show once again a very good agreement in comparison to the analytic solution. In all cases shown in fig. 2.9 we found a relative error under 0.5% near $\Omega = 12$.

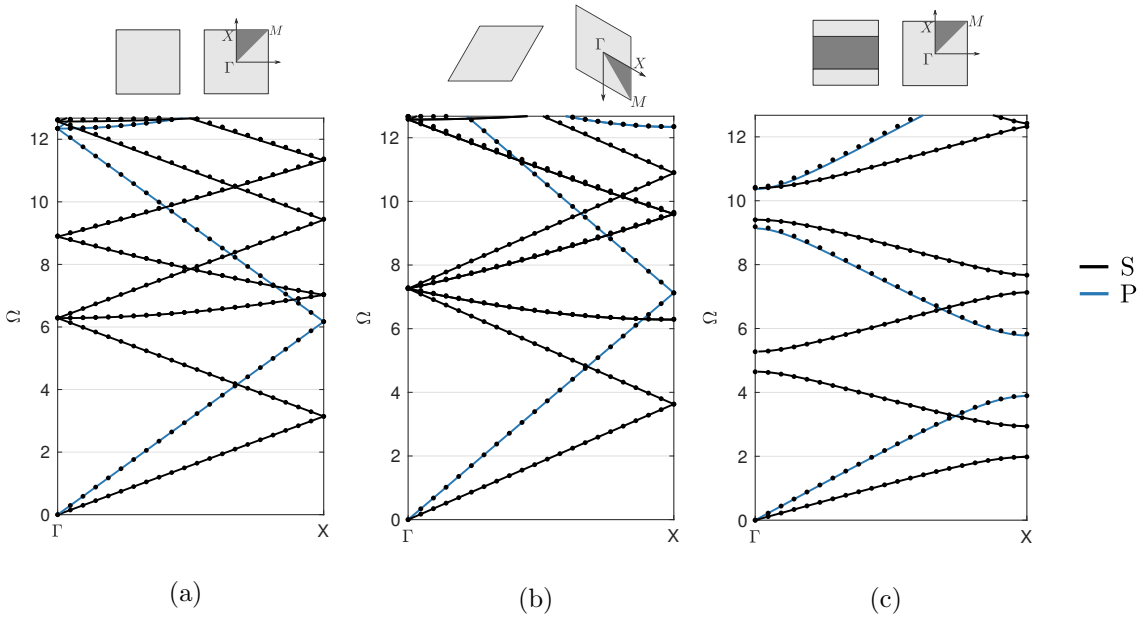

Figure 2.9. Dispersion relations for unit cells and material models with closed-form band structures under in-plane waves and a classic continuum mechanics model. Solid and dotted lines in each figure represent the analytic and numeric solution respectively. (a) Homogeneous material square unit cell with $\mathbf{k} = \langle 0, \kappa_y \rangle$. (b) Homogeneous material skewed unit cell with ΓX direction defined in fig. 2.8). (c) Bilayer material unit cell with $\mathbf{k} = \langle 0, \kappa_y \rangle$.

2.3.3 Verification against external numerical results

In order to increase the level of complexity in the analysis conducted with the element-based approach, we studied several unit cells reported in the literature and with dispersion relations computed numerically. Particularly, we considered symmetric cells corresponding to a square brass inclusion embedded in an aluminum matrix and a circular pore embedded in the same aluminum matrix. Both cases are reported in reference Langlet (1993). As a third case we also included the asymmetrical unit cell conformed by the Sierpinski right-angles isosceles triangles reported in Maurin et al. (2018). In this case, the porosity corresponds to a volume fraction of 40% with respect to an aluminum matrix. In all cases we used in-plane waves and a classic Cauchy model under plane strain idealization.

Squared inclusion and circular pore

The comparison for the dispersion relations obtained numerically with our proposed technique and those by the implementation reported in Langlet (1993) are displayed in Figure 2.10 and they clearly show to be in excellent agreement. The ratio between the characteristic dimensions of the inclusion and the side of the unit cell corresponds to $a_s/2d = 1/3$ for the brass inclusion and of $a_p/2d = 1/2$ for the circular pore. In the low frequency regime both materials exhibit a linear dispersion relationship highlighting the

fact that at long wave lengths (i.e., $\lambda >> 2d$) both materials behave as homogeneous non-dispersive materials with a group speed being an average from both materials present in the cell. This effect is however stronger in the case of the brass inclusion which, even at this low frequency regime, exhibits a higher group velocity than the material with the circular pore for both P and S waves. This is a rather obvious and expected result due to the lack of material continuity of the circular pore. Notice also that there is a small partial band-gap appearing in the porous unit cell right above the value of the dimensionless frequency of 3. This band-gap could be associated to the loss of material continuity caused by the pore.

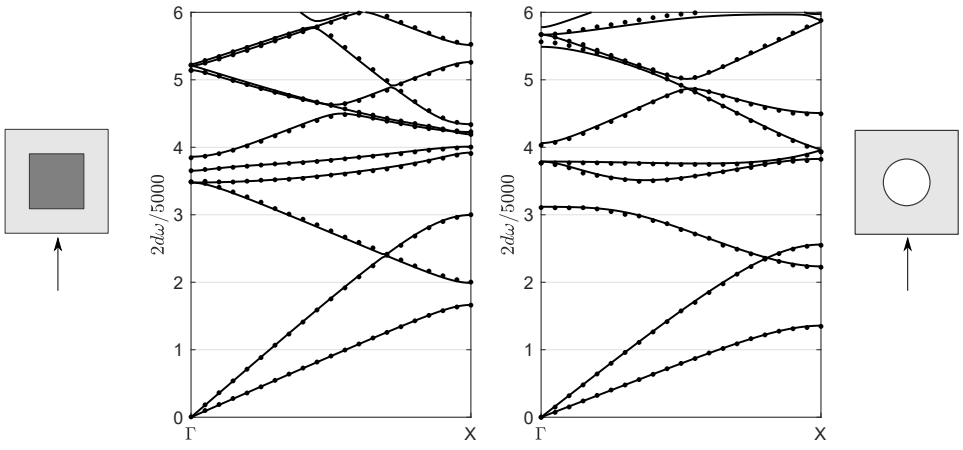

(a) Squared inclusion (b) Circular pore

Figure 2.10. Dispersion relations for unit cells conformed by (a) a squared inclusion and (b) a circular pore embedded in a homogeneous matrix. Solid line: Current strategy solution. Dotted line: results from Langlet (1993). For both cases $\mathbf{k} = \langle 0, \kappa_y \rangle$.

Asymmetrical unit cell

The results for the periodic Sierpinski right-angles isosceles triangles reported in Maurin et al. (2018) are shown and compared to those obtained with our approach in Figure 2.11. We computed the band structure over the complete Brillouin zone and over an additional arbitrary contour, and compare them with those reported in Maurin et al. (2018). As expected, the group speeds for the P ans S modes have linear non-dispersive behavior in the low frequency regime (see fig. 2.11c) showing once again the averaging effect upon the effective group speed introduced by the pores and without any significant effect of their shape. This cell also shows an interesting result which is observed when comparing low-frequency group speeds along the ΓX and ΓM directions. While P ans S waves have similar group speeds in the ΓM direction, they significantly differ along the ΓX direction. This particular aspect of the response can also be intuitively associated to the rupture of material continuity along particular propagation directions of the unit cell. It must also be observed that the asymmetry of the unit cell trans-

lates into asymmetries for the dispersion surfaces which are shown for completeness in fig. 2.11b. These surfaces have also been included, in an interactive visualization in the supplementary material of this article. In summary from the comparison between numerical results obtained via our element based approach and those reported in the literature it is concluded that the proposed technique allows also the computation of dispersion relations over arbitrary regions of the Brillouin Zone

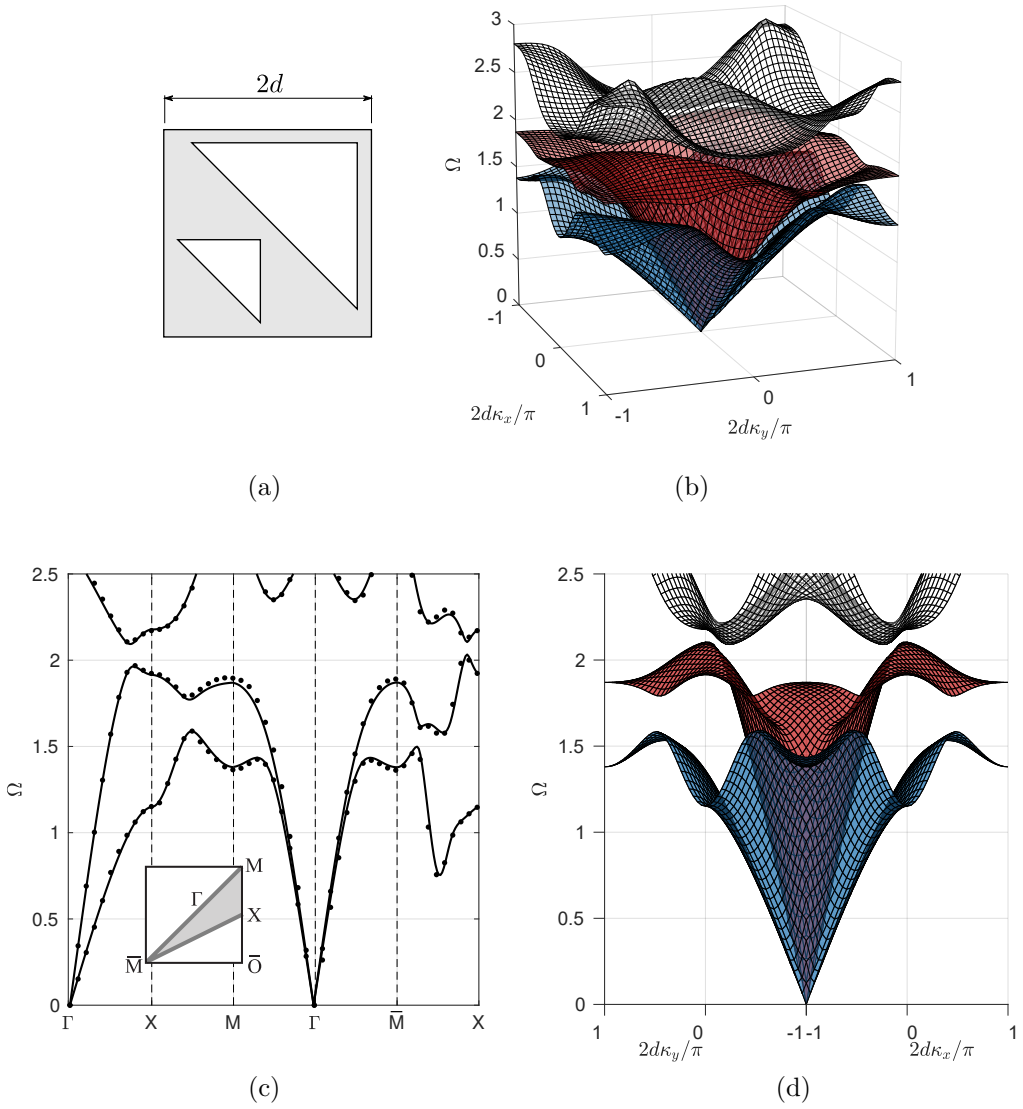

Figure 2.11. Dispersion relations for a periodic Sierpinski right-angled isosceles triangles with a porosity of 40%, under in-plane waves and a classic Cauchy model. (a) Sierpinski unit cell. (b) Dispersion relations surfaces for the first Brillouin zone. (c) Dispersion relations through an arbitrary contour in the first Brillouin zone. Solid line: current strategy solution. Dotted line: results from Maurin et al. (2018). (d) Detail on the dispersion relations surfaces.

2.3.4 Additional results

As a final test to show the versatility of our element-based approach to conduct Bloch analysis in periodic materials, we combined the three different kinematic models discussed previously with various microstructural configurations. We included the cases of a bi-layer material, a circular pore and a square and a checkerboard inclusion. Due to the common symmetry of these unit cells they all shared the same irreducible Brillouin zone (see fig. 2.12).

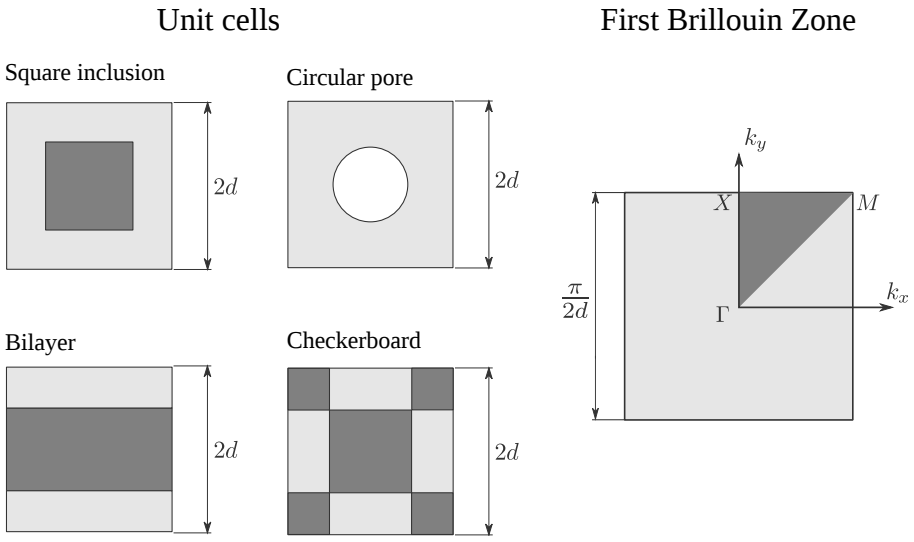

Figure 2.12. (Left) Unit cells used in the analyses. Light gray: Aluminum, dark gray: Brass. (Right) Illustration of first Brillouin zone and the irreducible Brillouin zone for the considered analyses. The unit cells were selected to have the same irreducible Brillouin zone.

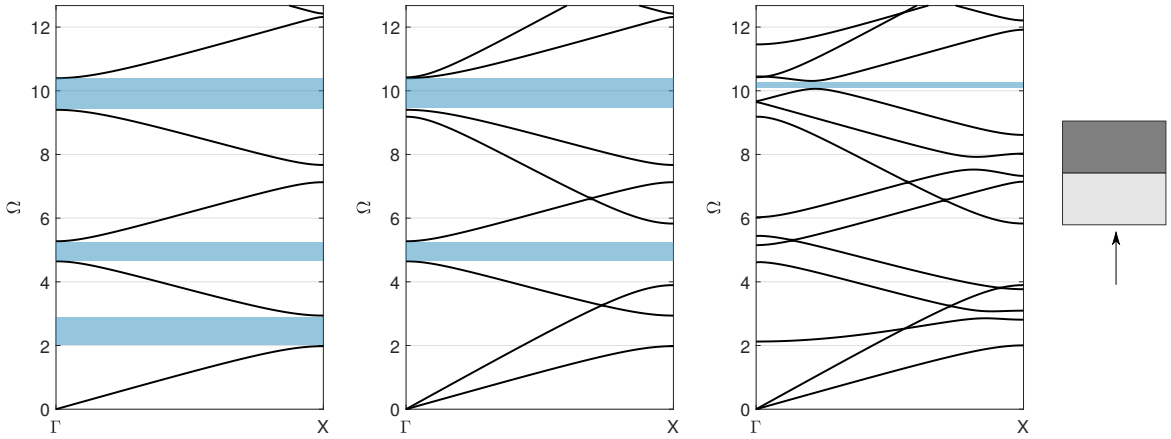

(a) Out-of-plane (b) In-plane (c) Micropolar

Figure 2.13. Dispersion relations for a bilayer material made with aluminum and brass under different kinematic models. Each layer has a thickness $t = d$. The analysis was made considering only the direction in which the material is periodic.

Figure 2.13 shows the results for the bi-layer material with base properties as per table 2.1. There are three S wave band gaps (shown by the shaded rectangle) in the out-of-plane kinematic model and all of them occurring along the vertical (ΓX) direction. Note that this is precisely the direction of periodicity of the microstructure. The lower frequency bandgaps are interrupted by the arising of the P wave modes after we consider the in-plane kinematic behavior. This pattern of elimination of bandgaps with the introduction of additional degrees of freedom, is also observed in the micropolar case shown in fig. 2.13c.

Similarly, fig. 2.14 presents the results for the circular pore, and square and checkerboard inclusions. In all unit cells, the out-of-plane case exhibits partial band gaps along the ΓX direction. As observed previously, these gaps are progressively eliminated as we introduce additional degrees of freedom into the model. For the micropolar model the rotational wave has a bandgap in the range $0 < \Omega < 2$, but for $\Omega < 2$, the responses with the micropolar and classical model are equivalent. The results for this last set of microstructures and kinematic assumptions are physically consistent as indicated by the additional branches obtained as we increased the number of degrees of freedom. Also, in the low frequency regime (under $\Omega = 1$), the group speed has a linear behavior which implies that waves with wavelength values $\lambda >> 2d$ (i.e., propagating at low frequencies), any microstructure will be blind to the propagating disturbance.

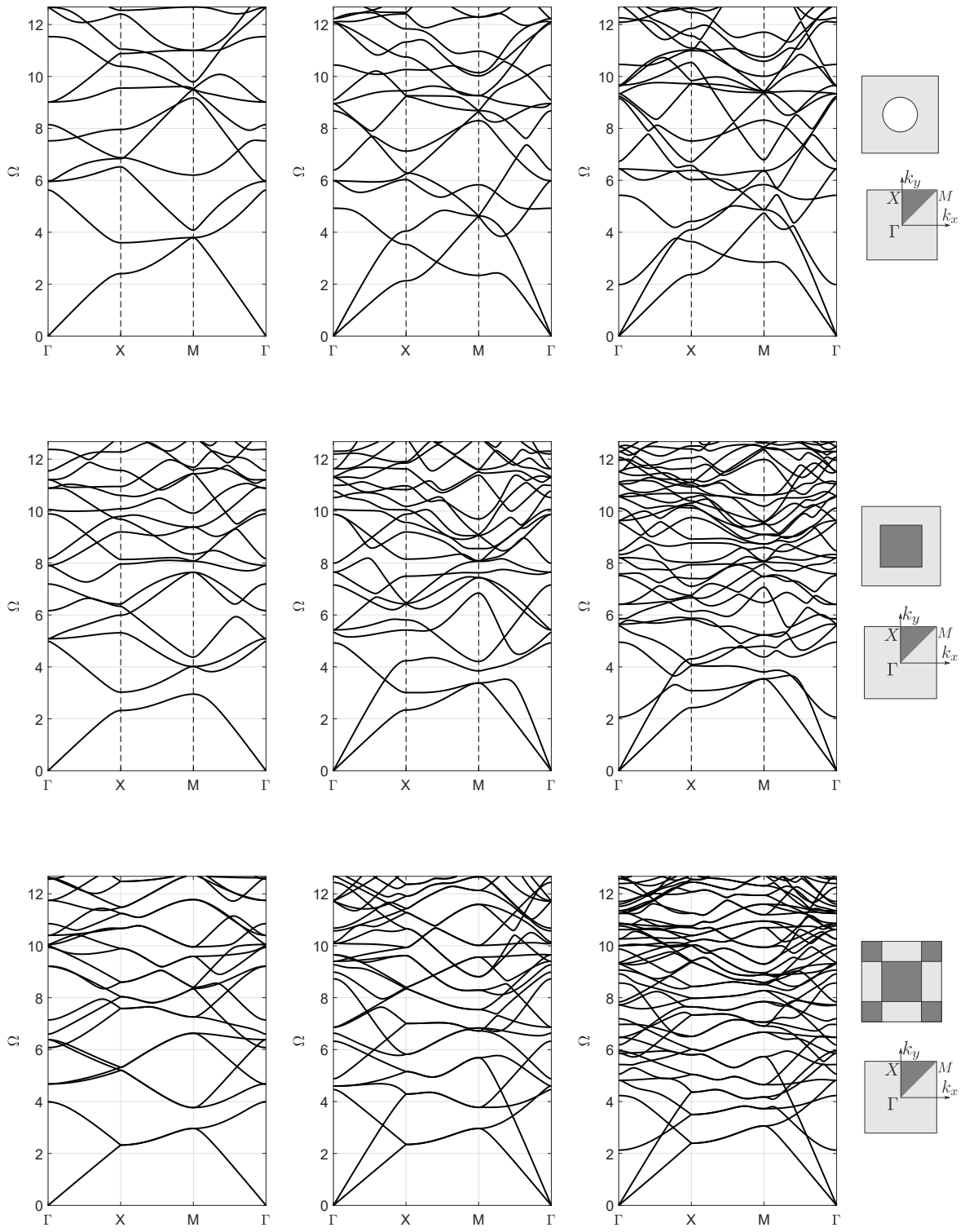

Out-of-plane In-plane Micropolar

Figure 2.14. Dispersion relations for different unit cells under different kinematic models. First row: Circular pore. Second row: Square inclusion. Third row: checkerboard. Columns 1 to 3 correspond to out-of-plane, in-plane and micropolar kinematic models respectively.

Conclusion

We have presented a novel and easy-to-implement computational alternative to obtain dispersion relationships in periodic phononic crystals using commercial (or already existing) finite element codes. The proposed approach has two basic appealing features: first, it avoids manipulating the global arrays, which is a forbidden operation in most codes; and second, Bloch periodic boundary conditions are imposed at the element level thus allowing for the consideration of problems belonging to different physical contexts. The approach is based on the creation of two assembly operators for those elements m subjected to Bloch boundary conditions, namely a C_m^c operator, which is used to retrieve element nodal coordinates and other relevant geometric information; and an operator termed C_m^a which assembles the element into the global arrays considering the proper boundary conditions at the onset. At the same time, the generality in the proposed technique makes the implementation to 2D and 3D problems equally easy. Moreover, the proposed strategy can be directly incorporated into existing user element subroutines just through subtle changes. Once implemented, the technique is straightforward to use since the user just needs to input the coordinate-connectivity operator C_m^c and the assembly-connectivity operator C_m^a for each element in the mesh. On the other hand, the complex-valued nature of the global arrays arising as a consequence of Bloch periodic conditions is dealt with using a duplicate-mesh approach reported in the literature. The method and its implementation was verified against closed-form solutions for a homogeneous and a bi-layer material under different kinematic assumptions and geometries for the unit cell. We also conducted additional verification exercises using numerical results reported by Langlet (1993) and Maurin et al. (2018). Finally, a detailed description to implement the presented strategy is provided in the supplementary material of this work in terms of a compiled version of FEAPpv with user element subroutines to compute dispersion relations.

Chapter 3

Directional response of periodic materials

Introduction

A second byproduct of the wave propagation analysis of periodic media is the characterization of the directional response of the material. As a fundamental question tere is interest in identifying how the possible wave modes propagate along different space directions. This chapter focuses in those fundamental aspects. It starts by describing the classical approach to conduct directional analysis. After pointing out some limitations of this approach the chapter introduces an alternative, or complementary technique which provides a more objective metric of the directional response. The chapter ends with the discussion and a comparisson through a simple example of both methods.

3.1 Classical metrics of wave directionality

The dispersion relation over the first Brillouin zone gives a set of phase constant (or dispersion) surfaces, where the number of surfaces corresponds to the dimension of the eigenvalue problem in eq. (2.3). When the dispersion surfaces are represented as iso-frequency contour plots, the direction of wave propagation at a given frequency can be calculated as the normal to the corresponding iso-frequency contour line. It is a common practice in the directional analysis of periodic materials to provide results in terms of iso-frequency contour plots Casadei & Rimoli (2013) and group velocity polar histograms based on iso-frequency contour lines (Ruzzene et al., 2003; Ruzzene & Scarpa, 2005). However in most of these analysis typical results are based on the first two modes of wave propagation, namely M_1 and M_2.

The surfaces associated to the modes M_1 and M_2 for wave propagation in a homogeneous material are shown in Figure 3.1(a). The wave propagation characteristics of a material are known to be tightly linked to their mechanical properties; therefore, in a homogeneous isotropic material where wave propagtion is independent of the prop-

agation direction an intuitive and appropriate measure of wave directionality should be in the form of a circle. However, as revealed in the contour plots and the corresponding polar histogram shown in Figure 3.1(c) and (d) respectively, this behaviour is only observed for mode M_1, while in M_2, the contour and radar plots incorrectly show anisotropic response, which is caused by S- and P-waves belonging to different Brillouin zones. Therefore, this approach provides biased results when considering directionality at low and high frequency regimes.

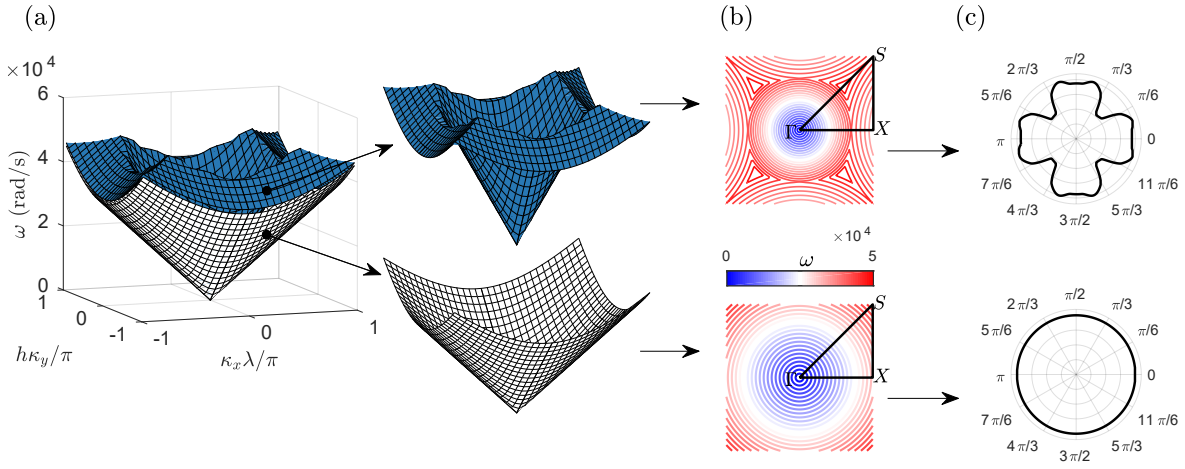

Figure 3.1. Traditional representation of directional behaviour for a homogeneous material unit cell with mechanical properties $E = 1\text{e}9\text{Pa}$, $\nu = 0.3$ and $\rho = 1\text{g/cm}^3$. (a) Surfaces white and blue correspond to modes M_1 and M_2 respectively. (b) Contour plots of modes M_1 and M_2. (c) polar plots showing the directional behaviour of each mode. Mode M_1 (S-wave) has an isotropic directional behaviour, while mode M_2 (P-wave) does not.

3.2 Definition of the new metrics

In this chapter, we propose an alternative strategy to obtain wave propagation directionality, which considers the contribution of multiple modes M_i. The approach provides the opportunity to conduct a more complete and objective description of the directional response of a periodic material valid in the low and high frequency regimes.

The wave propagation directionality, D, is defined here like

$$D = \sum_{\substack{i \\ e>tol}} d_i(\theta) \quad ; \quad d_i(\theta) = C\left(\frac{\nabla M_i}{\alpha}\right) \tag{3.1}$$

where ∇M_i is the gradient of the i-th mode in the dispersion relation, α is the P-wave

speed of the base material, *tol* is a predefined tolerance, $\theta = [0, 2\pi]$ is the angle defining the propagation direction. In this definition, the operator $C(V)$ performs the following operations over every vector v_t in the vector field V:

i Calculates the direction and magnitude of v_t.

ii Normalizes the magnitude of v_t by α.

iii Accumulates the normalized magnitude for all group velocity vectors sharing the same histogram bucket as v_t.

Consequently, $d_i = C\left(\nabla M_i/\alpha\right)$ corresponds to a weighted polar histogram representing the distribution of group velocity for mode M_i in any propagation direction. For instance, fig. 3.2 shows the polar plots resulting after applying the C operator over modes M_1, M_2 and M_3 in a homogeneous material unit cell.

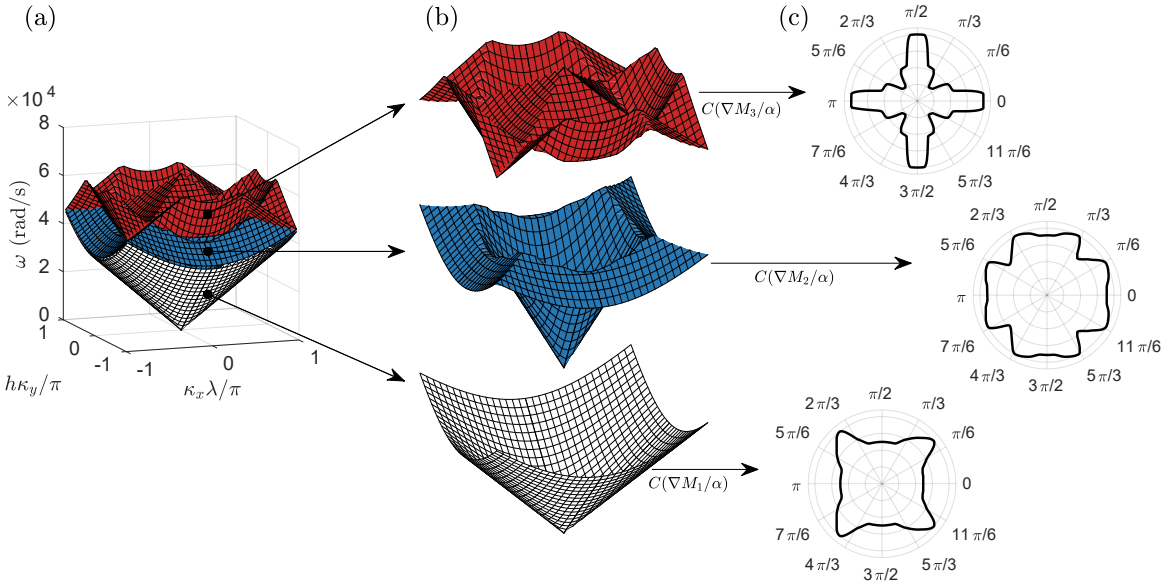

Figure 3.2. Result from appliying C operator to the first three modes from a homogeneous material unit cell with mechanical properties $E = 10^9$Pa, $\nu = 0.3$ and $\rho = 1\text{g/cm}^3$. Surfaces white, blue and red correspond to modes M_1, M_2 and M_3 respectively. On the right hand side: polar representation of d_1, d_2 and d_3; result of applying C operator to modes M_1, M_2 and M_3 respectively.

It should be considered that in this directional descriptor the error, e, is updated after each mode M_i is added to eq. (3.1). Here e is defined as:

$$e = \frac{1}{i} \sum_{\substack{j=2 \\ i>2}}^{i} \sum_{k=1}^{n_\theta} \left(\frac{d_j^k}{d_{j-1}^k} - 1 \right) \frac{1}{n_\theta} \tag{3.2}$$

where d_j^k is the k-th value of $d_j(\theta)$, and n_θ is the number of bins used to calculate the polar histogram charts. This error metric is an average measure of the general

change in directional behaviour produced by the introduction of a new term $d_i(\theta)$ into eq. (3.1). The process of adding modes is stopped when the error parameter e reaches the prescribed tolerance i.e. the marginal contribution from the last mode is smaller than a specified threshold.

3.3 Directinal response of a homogeneous material

Consider the application of eq. (3.1) to the unit cell of a homogeneous and isotropic material. Figure 3.3a shows the evolution of the polar plot describing directionality when considering $7, 14, 40$, and 114 propagation modes. As the number of modes increases, the polar plot approaches a circular shape. In this particular case a tolerance of 0.05 is reached after including 114 modes. For the rest of results reported in this work, *tol* was set to 0.05 and $n_\theta = 32$. The algorithm for this directional analysis approach, is fully detailed in section 3.3.

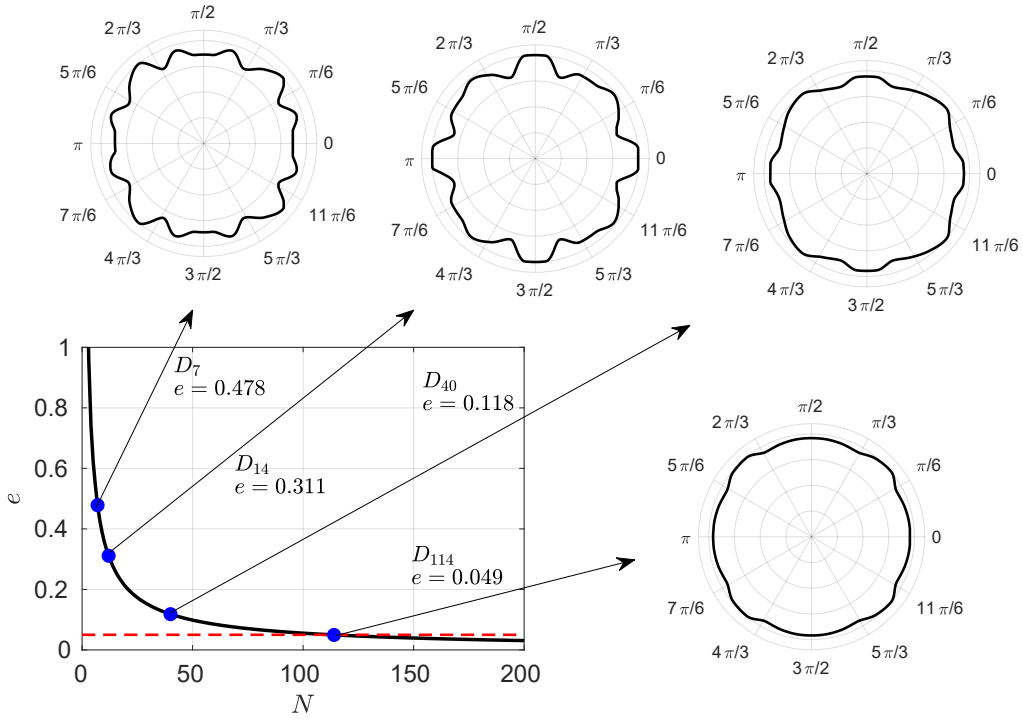

Figure 3.3. Evolution of directionality D and error e for a homogeneous material unit cell with mechanical properties $E = 10^9$Pa, $\nu = 0.3$ and $\rho = 1\text{g/cm}^3$. The terms D_N mean the directionality afer consedering N modes. The predefined tolerance $tol = 0.05$ is reached after 114 modes.

Data: Dispersion surfaces from Bloch analysis, tol, n_θ
Result: Final directional behaviour D
initialization of D, e, i; **Comment:** Arrays size: $D(n_\theta)$, $d(n_\theta)$
while $e > tol$ **do**
    vector field $V \leftarrow \nabla M_i/\alpha$;
    $G \leftarrow$ magnitude of V (group velocity of mode i) ;
    initialization of d;
    Comment: Vector count over the vector field V: $d \leftarrow C(V)$
    for $j \leftarrow$ *every vector* v_t *in* V **do**
        $dir_\theta \leftarrow$ calculate direction of vector v_t and assignment inside one angular section;
        $d(\mathrm{dir}_\theta) \leftarrow d(\mathrm{dir}_\theta) + G_j$;
        Comment: d informs how much group velocity is present inside each angular section
    end
    Comment: Update of D
    $D \leftarrow D + d$;
    Comment: Update of e
    $e \leftarrow$ compute error;
    $i \leftarrow i + 1$;
end

Algorithm 1: Detailed calculation process of directional behaviour

3.4 Comparisson of the studied metrics

Figure 3.4 shows the results of applying the classical and the propossed approach to three different unit cells. From the first row, corresponding to the homogeneous material, it is evident that the classic approach predicts an isotropic directional behavior for the 1^{st} S-wave mode; while the 2^{nd} P wave mode has an anisptropic behavior which is a misleading result. This incorrect directional behavior is due to the presence of branches belonging to adjacent unit cells, as exposed in chapter 1. The inherent mixture of information in Bloch analysis has to be carefully handled and consequently, modes M_1 and M_2 cannot be associated to S and P waves respectively. For the additional cases and due to the same spurious branches, the results from the classic approach are complex to analyse. For instance, the second row shows the results for a small squared pore embeded in a homogeneous material. In this case, mode M_1 predicts that the waves propagate along diagonal paths and it predicts horizontal and vertical paths for mode M_2. Analysing the available propagation paths in th unit cell, mode M_2 has an intuitive directional behavior while mode M_1 does not. For the case depicted in row 3, the results of directional behavior seem to be correct for modes M_1 and M_1 since they match the propagation paths of the unit cell.

On the other hand, the proposed approach always predicts directional behaviors that are in agreement with the propagation paths present in the material. These results show that the directional behavior is easier to analyse when computed with the propossed

approach.

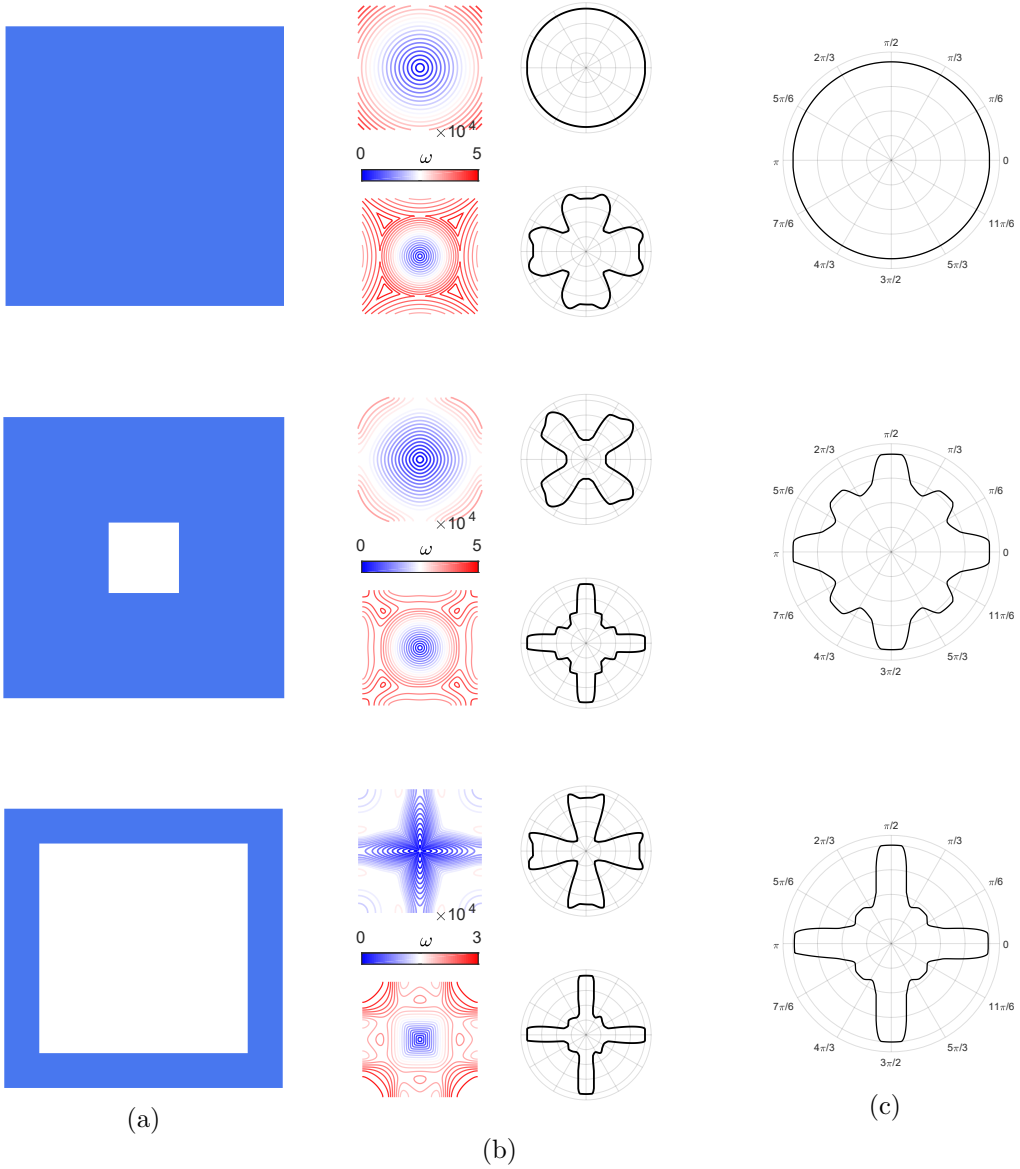

Figure 3.4. Directional behavior measured with two approaches. (a): Geometry of the unit cell. (b): Classic approach. In each subfigure the two rows correspond to the contour and polar histogram of modes M_1 and M_2 respectively. (c) Result with the proposed approach.

3.5 Results of directionality for different geometries and a Micropolar kinematic model

The directionality metrics are now applied to unit material cells whose kinematical behavior is that of a micropolar model. The mechanical properties of the material are

the same as those in the classical material model. In each one of the following figures the unit cell geometry is shown on the left while the right panels describe the evolution of directionality D and error e. The terms D_N inidcate the directionality after considering N modes.

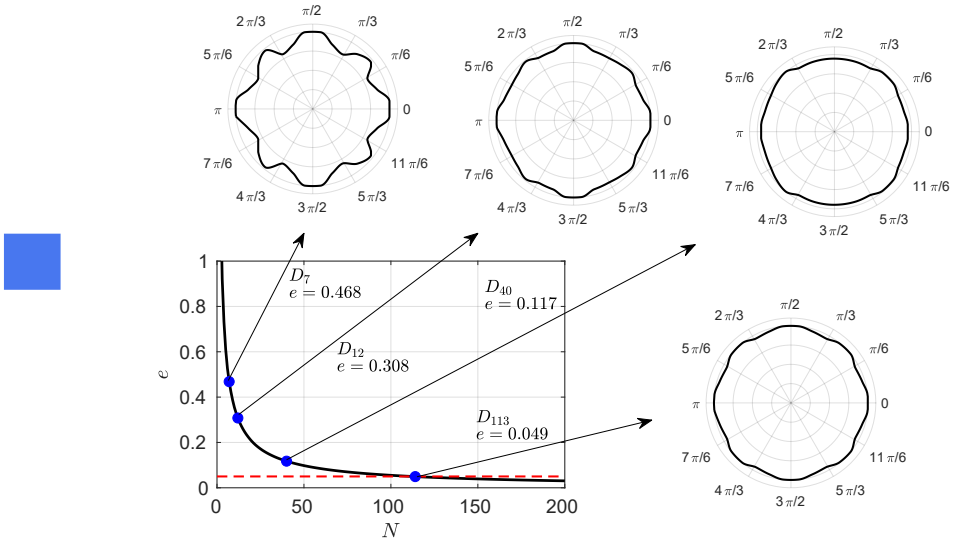

(a)

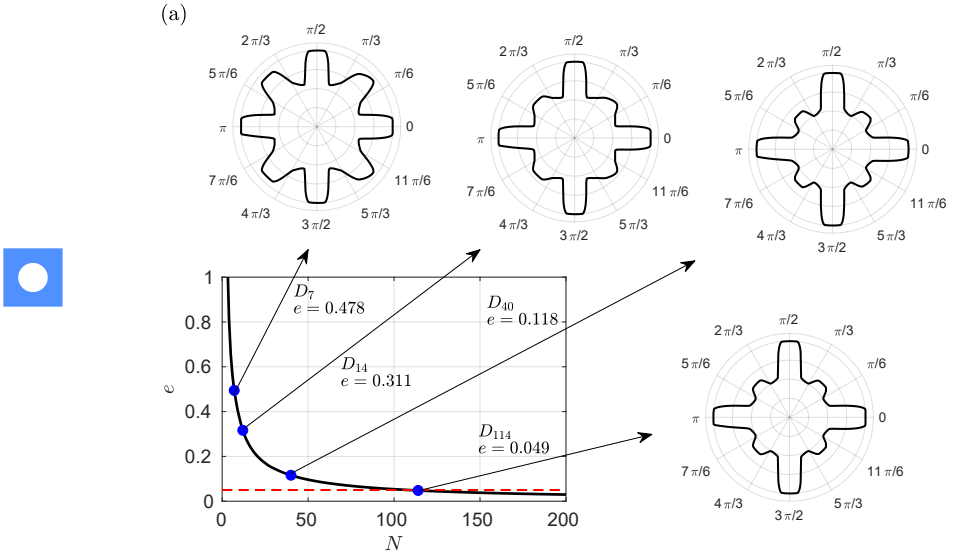

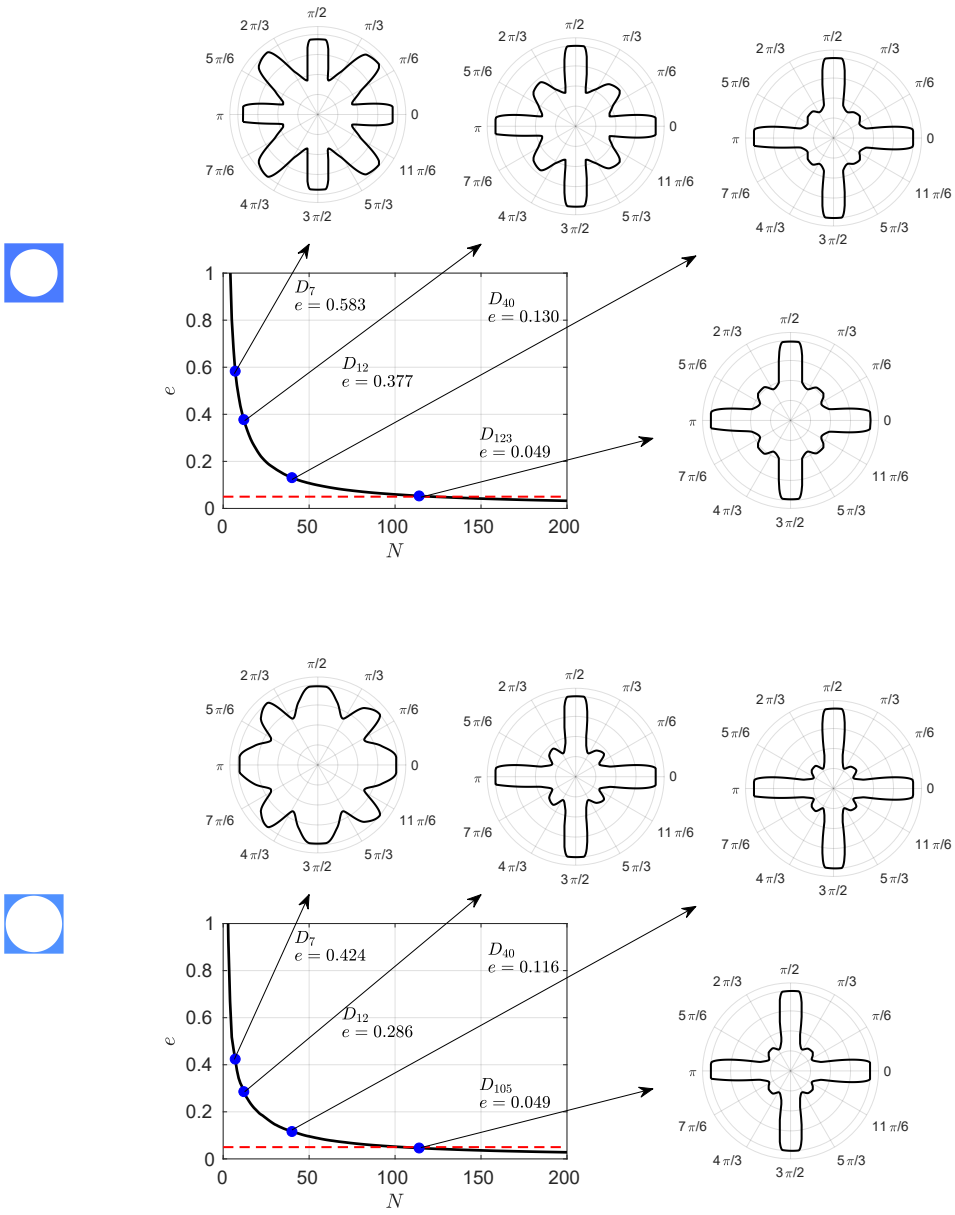

The new approach shows good results for the micropolar model. In the homogeneous case, S waves are dispersive and there is a new rotational wave which is also dispersive. Despite the dispersive nature of waves, we also expect to see a circle in the directionality plot because energy propagates in the same way in any direction. The circular shape in the polar plot becomes more evident as the number of modes considered increases. The rest of cases correspond to a circular pore with different sizes. This results, together with the results using a classical kinematic model shown before, agree with the propagation paths available in each analysed case.

Conclusion

We introduced a new metrics to describe the directional behavior of waves in a periodic material. This approach does not separate modes M_i and wave types (P or S); instead, it deals with several modes and all the wave types present in a periodic material. As seen in the first chapter, Bloch analysis has an inherent spatial aliasing since it contains information from infinite unit cells. Our approach takes advantage of that aliasing and considers all the information contained in Bloch analysis. Then it is not necessary to pre-process the dispersion surfaces before making directionality calculations. It is a qualitative tool, useful to describe the global behavior of waves when propagating through the analysed material; and it is intended to be used as a complement to dispersion curves and surfaces. Additional applications of this metric are shown in chapter 4. The directionality metrics are also tested for some unit cells with a micropolar kinematic model. This new approach is not better nor worse that the classic one, but it just provides different information.

Chapter 4

Analysis of a Phase Transforming Cellular Material

Introduction

Architectured materials offer the possibility of tailoring its macroscopic response to meet prescribed requirements by virtue of its microstructural design. Common examples of this emerging field within the material science community are identified in the strong development of cellular and metamaterials applications (Banerjee, 2011; Hussein et al., 2014b; Norris & Haberman, 2012b). Among the many appealing features of such class of materials, energy dissipation is specially attractive as it can be achieved through the combination of several mechanisms Lu et al. (2009); Kadic et al. (2013); Leroy et al. (2015). In parallel, cellular materials posses intrinsic wave attenuation capabilities introduced by its spatially periodic nature (Hussein et al., 2014b). Moreover, the importance of energy dissipation and wave manipulation in many fields of engineering and physics and the interesting properties associated to metamaterials have motivated the engineering community to embrace in the study, analysis and design of new and novel cellular materials. Restrepo et al. (2015) and Correa et al. (2015) have proposed a phase transforming cellular material (PXCM) which, depending upon the values of its geometrical parameters has the ability to sustain multiple equilibrium configurations and thus to dissipate energy through the change from one stable configuration to the other: interestingly, this energy dissipation occurs while the base material remains elastic as it takes place by large elastic deformations. On the other hand, cellular materials are known by its attractive features to attenuate, forbid or enforce the propagation of waves in certain frequency ranges and directions. The phase change inherent in the mechanics of the PXCM occurring hand-to-hand with the change in the cellular structure raises natural questions regarding the band structure of the periodic arrangement. This paper focuses in the characterization of the dynamic features of PXCMs in connection with its possible stable configurations.

The study of periodic cellular materials from its wave propagation perspective is commonly conducted in terms of its dispersion properties or band structure and direction-

ality description (Gonella & Ruzzene, 2008; Mousanezhad et al., 2015; Trainiti et al., 2016). In the case of spatially periodic materials this can be achieved using numerical methods together with the application of Bloch's theorem (Brillouin, 1953) over the unit material cell. A dispersion analysis for a cellular PXCM material, closely related to the one proposed by Restrepo et al. (2015) has been conducted by Meaud & Che (2017). These authors analyzed the dispersive properties of a multistable architectured mechanism in the direction of bistability. That analysis however focused in the response of the material along a single direction based upon the fact that the material was strictly periodic along that specific direction. Although the one-dimensional periodicity of the PXCM precludes the existence of complete or multi-directional band gaps, the cellular nature of the material introduces additional effects in the propagation characteristics together with its directional behaviour. Some additional analyses of multistable cellular materials can be found in Shan et al. (2015), these authors made numerical and experimental analyses to test the capabilities of a multistable mechanism to trap strain energy. Debeau et al. (2018) analyzed negative stiffness honeycomb materials under quasi-static and impact loads. Schaeffer & Ruzzene (2015) studied the dispersive behaviour of magneto-elastic lattices. Haghpanah et al. (2016) tested a variety of 2- and 3-dimensional multistable Shape-Reconfigurable mechanisms. Finally, Frazier & Kochmann (2017); Nadkarni et al. (2014) performed some theoretical and numerical analyses over mechanisms containing bistable elastic elements.

In this chapter the dispersive properties imposed by the cellular structure of the PXCM are explored from a conceptual point of view and aiming at the identification of mechanisms controlling band gap properties (i.e., width and location); as well as its directional behaviour, computed with the approach proposed in chapter 3. For that purpose, Bloch analysis and transient simulations to determine the response of finite domains are used. All of the concepts and the computational tools developed previously are used in this chapter. To develop conceptual understanding of the cell response we progressively track –from the gap structure perspective– the behaviour of an initially perfect homogeneous material cell and subsequent degenerations until reaching the final configuration of the actual PXCM. The progressive analysis is also conducted for the directional response in terms of an alternative approach which objectively considers the contribution from low and high frequency modes. After identifying some key aspects governing the cell behaviour steaming from the progressive analysis, we also conduct a second study, directly in the time domain and where we impose a displacement-controlled excitation over a finite 10×1 super-cell. To test the effective wave filtering capabilities in the material the excitation to the super-cell is applied as a single-frequency wavelet with characteristic frequencies inside and outside of the previously found band-gaps. As a result, we are able to identify: (i) mechanisms responsible for the presence (or absence) of band gaps in vertical direction; (ii) mechanisms that control the frequency location and bandwidth of the gaps in vertical direction; and (iii) mechanisms that control the directionality properties of the cells. Such conceptual understanding of the problem allows us to develop fine-tuning capability of the unit cell to match a target input.

This chapter is organized in two main sections. The first part discusses fundamental theoretical aspects related to the basic mechanics of the PXCMs. The second part

describes the dispersive analysis of the PXCM per se including the study of the progressive cells conducted upon partial configurations of the unit cell leading to the final geometry of the PXCM together with the full analysis of the super cell in the time domain.

4.1 Mechanics of the phase transforming cellular material

A unit cells of a PXCM comprises two compliant bistable mechanisms. Each of these bistable mechanisms exhibits a force-displacement response that is characterized by two limit points ((d_I, F_I) and (d_{II}, F_{II})) as seen in fig. 4.1a. This allows us to segment the response into three characteristic regimes: regimes I and III that are characterized by a positive stiffness as they represent the deformation of stable configurations of the unit cell, and regime II that is characterized by a negative stiffness (Howell, 2001; Howell et al., 1994). These unit cells are arranged in a space-filling array to make PXCMs. The mechanical response of a two unit cell material is as shown in fig. 4.1(b).

The unit cell configurations corressponding to the two stable equilibria are interpreted as phases of the PXCM, and a change in the configuration of its unit cell between stable configurations is interpreted as a phase transformation (Restrepo et al., 2015). The propagation of the phase transformation corresponds to a progressive change of configurations from one row of bistable mechanisms to the next one, leading to a serrated plateau in the force-dispalcement response. Traversal of the limit points results in the non-equilibrium release of stored strain energy. Thus, PXCMs exhibit hysteresis under mechanical loading and the force-displacement has two finitely separated serrated plateaus that correspond to loading and unloading respectively. is different for loading and unloading; therefore, PXCMs exhibit large hysteresis. If the unit cells are designed such that despite undergoing large deformations the strains in the cell elements do not exceed the elastic limit of the constituent material, there is no irreversible deformation during the loading and unloading of these materials. Hence, the material can be used to dissipate energy multiple times.

In addition to energy dissipation, phase transformations in PXCMs are accompanied by large configurational changes in the unit cell. These changes affect macroscopic properties of the material such as its effective density. In this chapter we investigate the effect of these changes on the wave propagation behavior of the material e.g. changes in the propagation of elastic waves over certain frequency bands (band gaps), and changes in the direction of vibrational energy propagation through the material.

In this part we focus our analysis on the PXCM shown in fig. 4.1c which was introduced by Restrepo et al. (2015). The unit cells of this PXCM are composed of two curved beams that are connected by stiffening walls, which provide local support and prevent transverse displacements. This lateral constraint allows the curved beams to function as bistable mechanisms. The shape of the curved beams is described by $y = (\frac{A}{2})[1 - \sin(2\pi(x - \lambda/4)/\lambda)]$, where λ is the wavelength; and A the amplitude (peak to valley).

Other geometric parameters for the unit cell are the beam thickness t, out of plane depth b and the thickness of the stiffening walls which is set to $1.5t$. The mechanical response of the curved beams is primarily determined by the amplitude to thickness ratio $Q = A/t$; bistable behavior is obtained when $Q \geq 2.41$ (Vangbo, 1998; Qiu et al., 2004; Restrepo et al., 2015). The maximum strain in the beams, $\varepsilon_{max} = 2\pi^2 \frac{tA}{\lambda^2}$, should be kept below the yield strain of the base material to avoid irreversible deformation and allow the material to be used multiple times. In this work the geometric parameters describing the unit cell of the PXCM were kept constant with values corresponding to $A = 9.04$ mm, $\lambda = 60$ mm, $b = 20.576$ mm, and $t = 0.742$ mm.

Although this PXCM is a 2D cellular material, phase transformations take place only for loads in the y-direction and its deformation is mainly governed by the deflection of the curved beams. Three stable configurations can be identified at the unit cell level: open, intermediate, and closed as shown in fig. 4.1d.

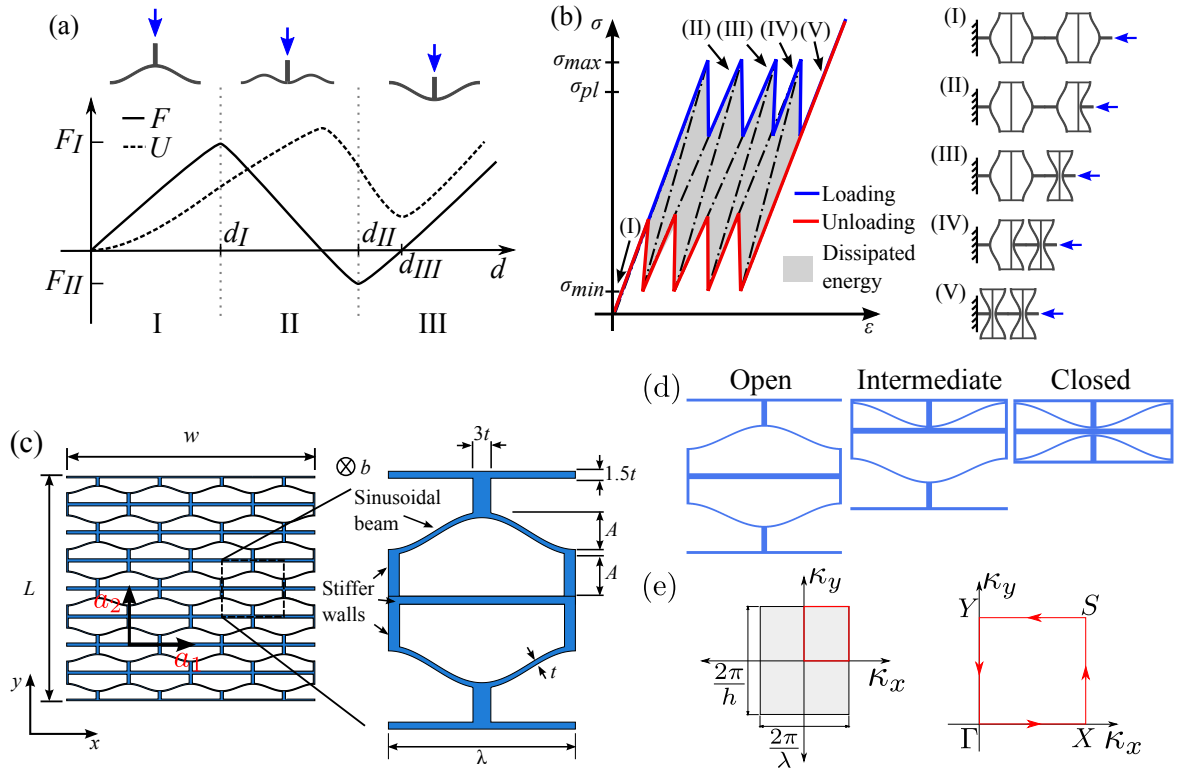

Figure 4.1. Phase Transforming Cellular Materials (PXCM). (a) Schematic representation of the force-displacement ($F - d$) behavior and change of potential energy (U) as function of displacement for a bistable mechanism, (b) force-displacement behavior for a two unit cell PXCM sample, (c) geometric parameters for a PXCM sample and a constituent mechanism and (d) stable phases at the unit cell level. (e) First Brollouin zone and Irreducible Brillouin zone. Parameter h is the total height of the unit cell at hand.

4.2 Dispersive behaviour of a PXCM

We now conduct a series of dynamic analyses aimed at elucidating the most relevant physical aspects governing the dynamic properties of PXCMs. The unit cell and the first Brilloun zone used for this analysis are shown in fig. 4.1. We start by examining the dispersion diagram of a simple homogeneous cell and subsequent states corresponding to perturbations of this base geometry, until obtaining the unit cell corresponding to a PXCM (See Figure 4.2). Since we proceed through a sequential approach in which a given cell is a one-step modification of the previous one, we refer to this as a *progressive cell analysis*. The results from this progressive method of analysis are presented in terms of dispersion relations along the irreducible Brillouin zone $\Gamma XSY\Gamma$ and directional behaviour plots, aiming to provide insights about the contribution of different members forming the PXCM to the dynamics of wave propagation. Subsequently we studied the PXCM in each of its stable configurations (open, intermediate, and closed) using Bloch theory, and complementing with full-scale time domain finite element simulations with the goal of testing the filtering capabilities of these materials resembling conditions corresponding to an actual application. For all results reported in this paper the base material forming the walls of the PXCM is considered to be linear isotropic with properties $E = 10^9$Pa, $\nu = 0.3$, and $\rho = 1\text{g/cm}^3$. It is also noted that self-contact effects are neglected in the simulations.

4.2.1 Progressive construction of the Open PXCM cell

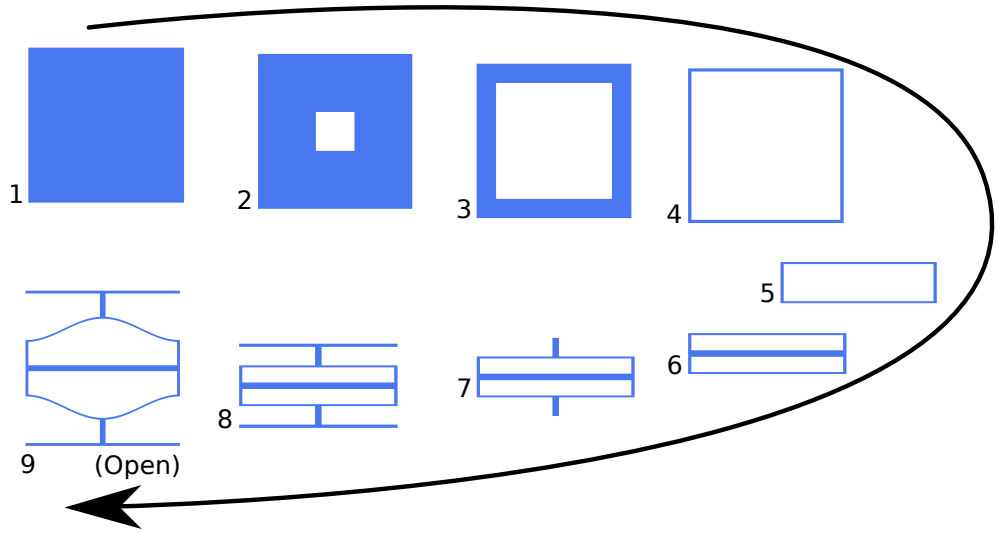

Figure 4.2. Progressive construction of the open PXCM unit cell. Stages 1 to final open configuration.

Figure 4.2 shows the evolution of the geometry to reach the final open configuration in our progressive analysis approach. At stage 1, we started from a squared homogeneous material unit cell, where the Bloch-periodicity response is fully understood as this material only propagates P and S waves with no dispersion. Then, we progressively introduced a variable-sized square pore in the center of the unit cell beginning with a

negligible defect (stage 2) that grows until the unit cell becomes a thin frame (stages 3-4). As a final perturbation we changed the aspect ratio of the cell (stage 5) and added elements to reach the open-cell configuration of the PXCM (stages 6-9). Although, stage 1 can be fully characterized using direction ΓX, and stages 2-4 can be described using $\Gamma XS\Gamma$, in all our analyses we used the IBZ as in the final PXCM, i.e., $\Gamma XSY\Gamma$ in fig. 4.1(e), allowing us to track down the modes and wave-types in the dispersion diagrams, and to relate the cell geometry and topology to group velocity and to the emergence of band gaps. For each configuration we report the dispersion diagram and the directional behaviour (see figures 4.3-4.5). As a physical reference to support the interpretation of results, dashed red lines are overlaid over the dispersion diagrams indicating the P and S-wave speeds in the homogeneous material.

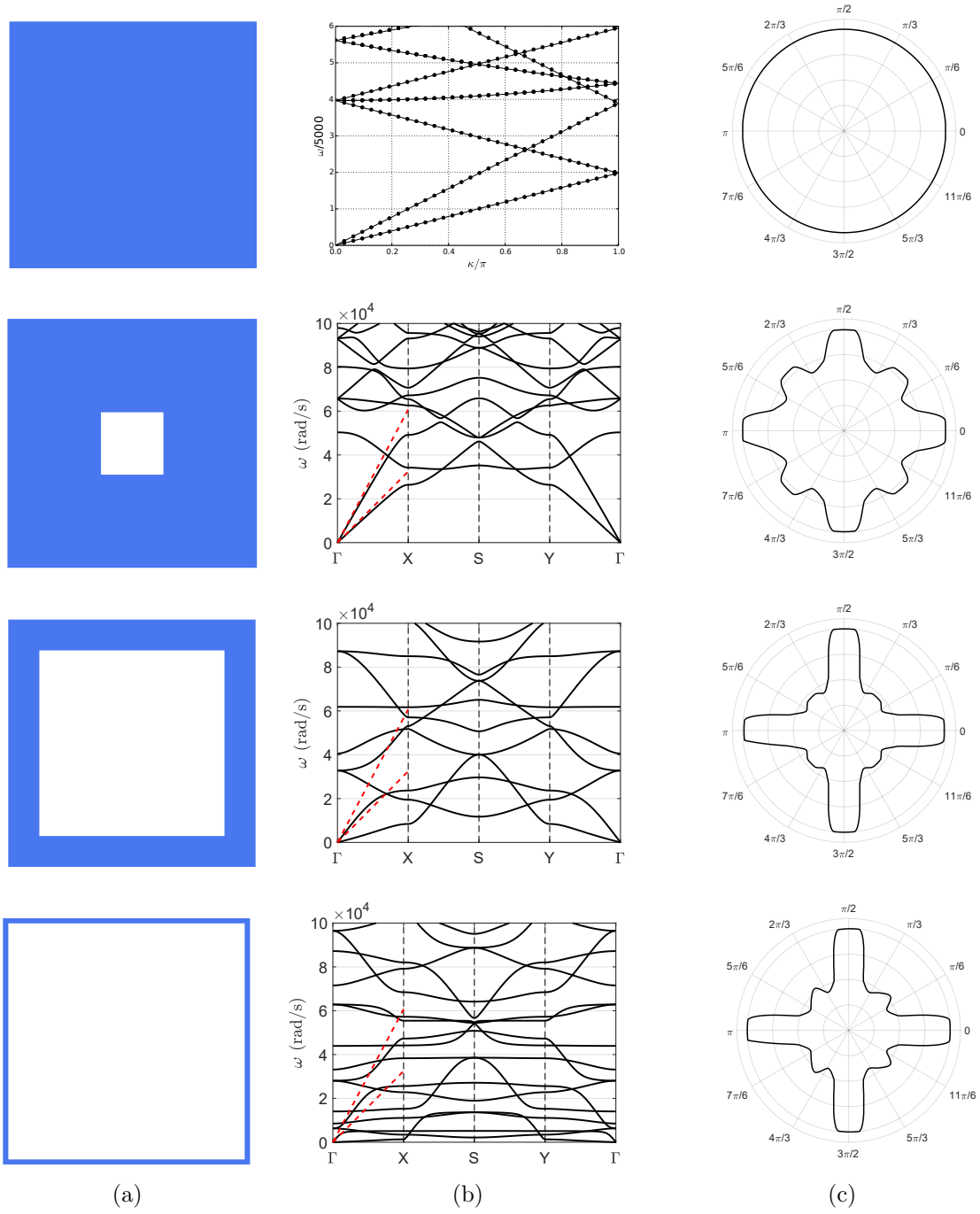

Figure 4.3. Progressive construction of the unit cell. Stages 1 to 4. Column (a) illustrates the unit cell while columns (b) and (c) show the dispersion diagrams along the IBZ and directional behaviour respectively. As a physical reference, dashed red lines are overlaid over the dispersion diagrams indicating the P and S-wave speeds in the homogeneous material.

Figure 4.3 shows the results from the progressive analysis during stages 1 to 4 and corresponding to the introduction and subsequent grow of the square pore in the homo-

geneous unit cell. There are two important observations from these results. First, from the band diagrams along the ΓX and $Y\Gamma$ directions it is evident that group velocity for the P and S-waves decreases as the size of the pore increases. This is a consequence of the wave packages encountering less material to propagate. Second, along the ΓX direction, this decrease occurs at a higher rate for the S-wave than for the P-wave. When the unit cell turns into a thin frame (stage 4) the group velocity of the P-wave is still close to the reference value of the homogeneous cell, while the S-wave is already at a low value of 5% of its homogeneous counterpart. This feature of the response is the result of the horizontal bars along the ΓX direction having a large longitudinal stiffness in comparison with its transverse response thus favoring a higher P-wave velocity. An analogous response is observed along the $Y\Gamma$ direction. Finally, as the pore size increases, the directionality diagrams show that waves tend to propagate in vertical and horizontal directions.

The next steps in the progressive analysis are indicated by stages 5 and 6, corresponding to the flattening of the square cell (stage 5) and to the addition of a horizontal bar (stage 6). The results for these stages are shown in fig. 4.4. From the dispersion diagrams, it is noted that the change in the aspect ratio with respect to the square cell destroyed the symmetry along S in the IBZ. In addition, stage 5 shows a strong directionality of propagation along the vertical direction, associated to the thicker thickness of the vertical walls. This result becomes evident after a comparison of the directionality diagrams in stages 4 and 5. However, this behaviour is reversed after the introduction of the additional horizontal wall in stage 6, which creates more favorable conditions for propagation along the horizontal direction.

In the final steps of the progressive analysis we introduced stiff vertical (stage 7) and horizontal bars (stage 8), and finally, in stage 9 the main horizontal element is deformed into its final sinusoidal shape. The main topological difference between stages 7 to 9, with respect to previous stages, is the rupture of material continuity introduced by the vertical bar added during stage 7. Here we define a material as continuous in a specific direction if a ray can follow an uninterrupted path when traveling along that direction. If such path exists, the material is therefore continuous and a wave would be able to propagate independently of the value of $\mathbf{k}$. This is precisely the case for stages 1 through 6 where there is horizontal and vertical continuity, and therefore, there are neither complete nor partial bandgaps. To clarify this last aspect we define a bandgap as complete when it covers all the IBZ and as partial otherwise. The results for this last set of perturbations are shown in fig. 4.5. According to these results, it is observed that a given direction favors the propagation of a single wave type. For instance, considering the horizontal (ΓX) direction and the fact that the horizontal bars coincide with the polarization direction of P waves, while they oppose that of S waves, favors the transport of energy for the P-wave while it slows down the propagation of the S-mode. The same analysis can be performed onto P and S-waves propagating vertically. The same directional behaviour is also visible in the dispersion relations. Along the ΓX direction there are branches with high group velocity,corresponding to P-waves. On the other hand, along the $Y\Gamma$ direction the P and S-wave group velocities exhibit a considerable decrease as compared with the previous stage. In this case and

due to the interruption in material continuity there are now partial band gaps in the material. They are identified along the XS and $Y\Gamma$ directions. Results from stage 7, 8 and the final open PXCM cell are similar in terms of dispersion relations and directional behaviour. At this point is clear that the progressive analysis has been effective in establishing the connection between the final PXCM geometry and the resulting dispersion diagram.

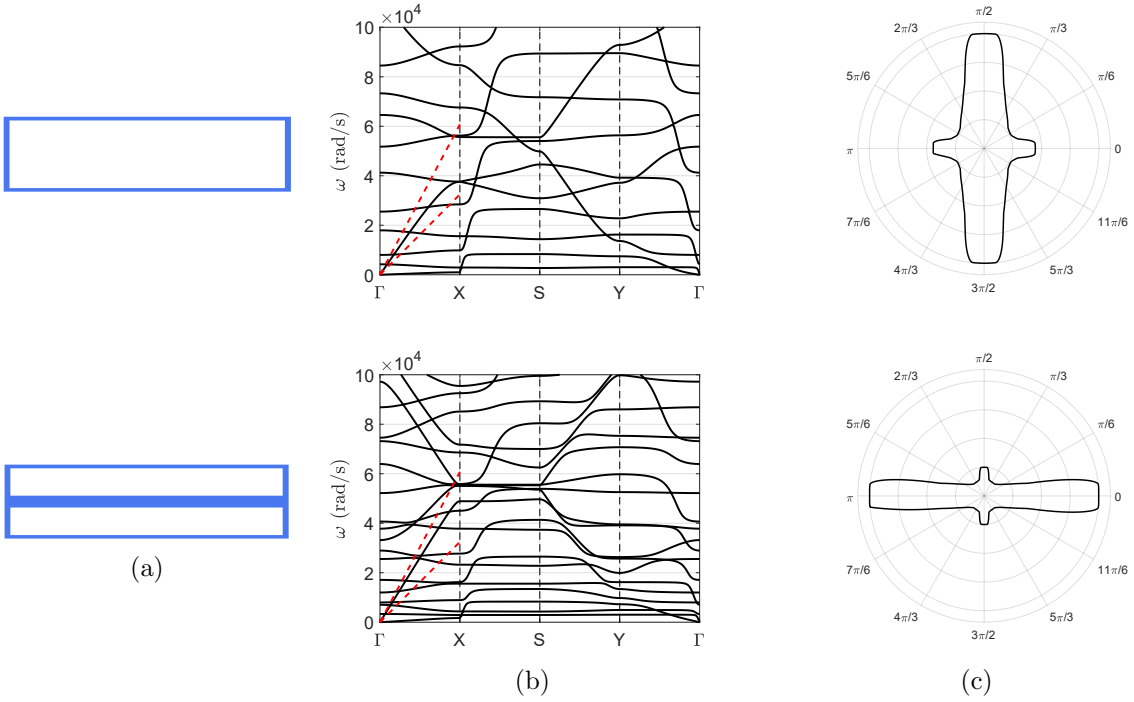

Figure 4.4. Progressive construction of the unit cell. Stages 5 and 6. Column (a) illustrates the unit cell while columns (b) and (c) show the dispersion diagrams along the IBZ and directional behaviour respectively.As a physical reference, dashed red lines are overlaid over the dispersion diagrams indicating the P and S-wave speeds in the homogeneous material.

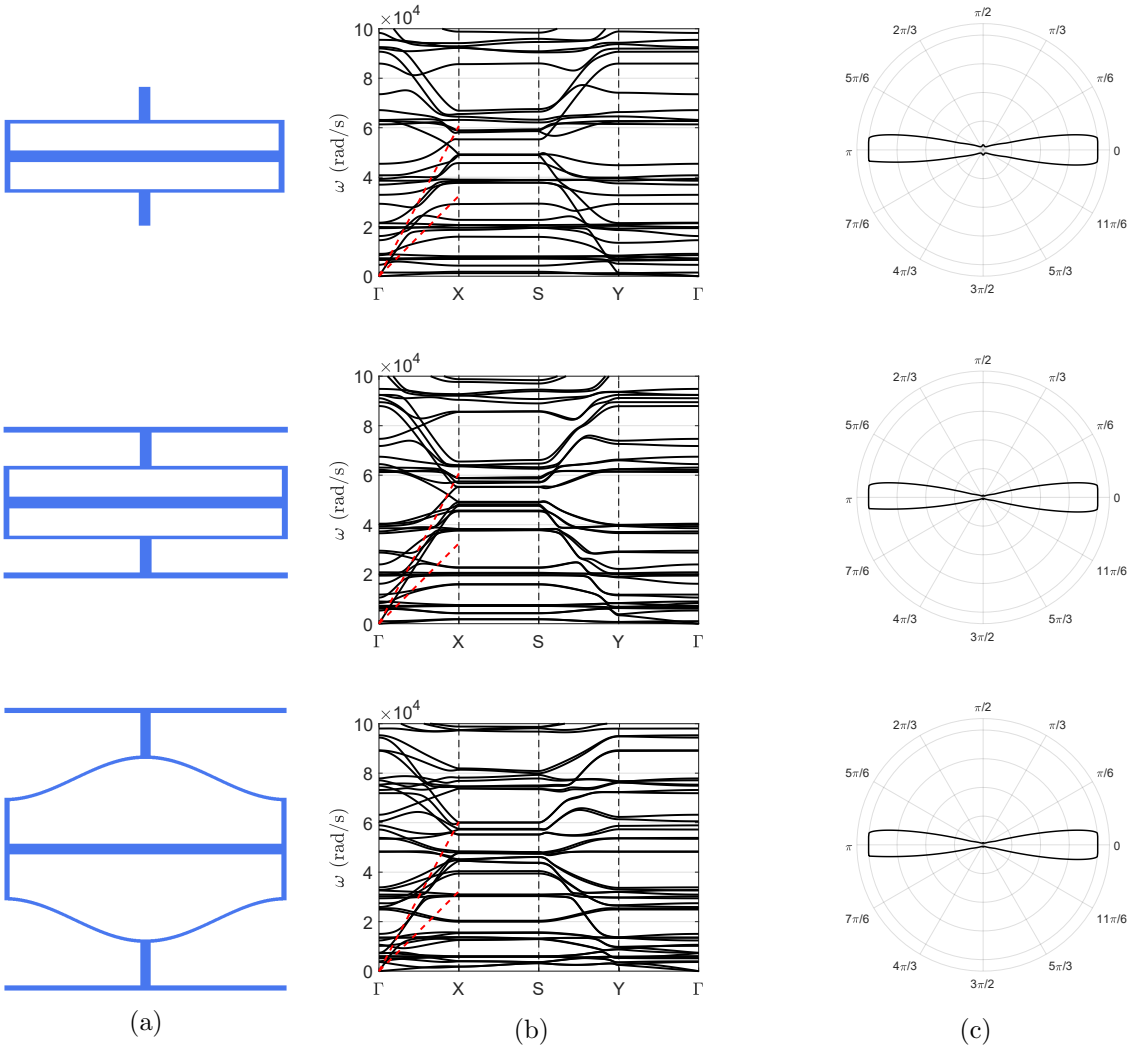

Figure 4.5. Progressive construction of the unit cell. Stage 7 to open configuration. Column (a) illustrates the unit cell while columns (b) and (c) show the dispersion diagrams along the IBZ and directional behaviour respectively.As a physical reference, dashed red lines are overlaid over the dispersion diagrams indicating the P and S-wave speeds in the homogeneous material.

4.2.2 PXCM cell in different stable configurations

For completeness we present the results corresponding to the unit cell of the PXCM in its stable open, intermediate, and closed configurartions. As pointed in the previous section, the wave propagation response is controlled by the directions of continuity in the material; therefore, there are not considerable changes observed in the dispersion diagrams for each of the stable configurations of the PXCM in relation with the results from stages 7 through 9. Moreover, the responses in the open, intermediate, and closed configurations are equivalent as it can be seen from the band diagrams and directionality plots shown in fig. 4.6, where all the partial bangaps observed in the dispersion digrams

occur at near the same frequency values, and the directionality is strongly horizontal in all the three cases. This effect can be understood by considering the concept of material continuity. For instance, a ray traveling along the vertical direction finds the same amount of material interruption regardless of the cell being open or closed. This occurs, because, although the cell geometry changes, the cell topology does not. And consequently, the energy distribution through the cell is not altered in the different configurations.

Finaly, from the progressive analysis and the study of the PXCM cell in its 3 stable configurations, it can be concluded that PXCMs can be effectively used as a low-pass mechanical filter along the vertical direction ($Y\Gamma$) and designed for a determined cut-off frequency. In this sense energy can be attenuated near the same frequencies independently of the cell topology. At the same time the material can be used as a P-wave guide in horizontal direction. These properties of the material due to its periodic nature can additionally be combined with the energy dissipation capability associated to the process of switching between multiple stable configurations previously reported by Restrepo et al. (2015).

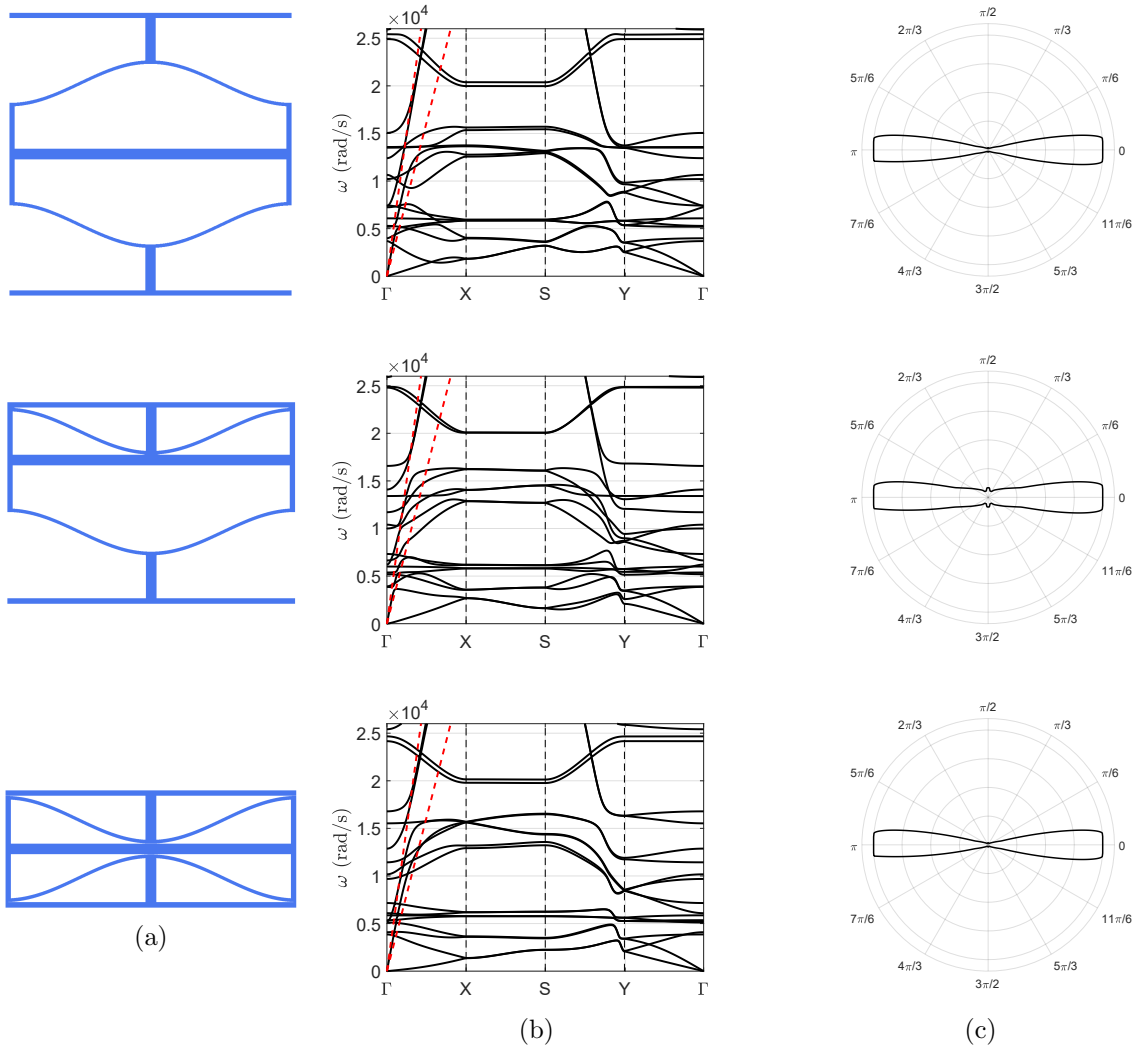

Figure 4.6. Comparison between different configurations. Column (a) illustrates the unit cell while columns (b) and (c) show the dispersion diagrams along the IBZ and directional behaviour respectively. As a physical reference, dashed red lines are overlaid over the dispersion diagrams indicating the P and S-wave speeds in the homogeneous material.

4.2.3 Super cell analysis

To complement the Bloch analyses, we conducted direct time domain analysis of a super-cell with dimension 10 × 1 unit cells for the 3 stable configurations of the PXCM. For each of the simulations, the super-cell model was excited at the bottom with an imposed displacement time history following a harmonic function and producing an incident P-wave traveling along the vertical direction ($Y\Gamma$), corresponding with the direction where phase transformations occur and where partial band gaps were previously identified. We used roller supports on the lateral sides and absorbing boundaries on the top surface. In order to verify the effectiveness of the material in different band gaps, the input

excitation is designed using the dispersion relations shown in fig. 4.7 and corresponding to the dispersion properties along the $(Y\Gamma)$ direction. We used frequencies $f_1 = 2000$ rad/s, $f_2 = 4500$ rad/s, $f_3 = 8000$ rad/s and $f_4 = 20000$ rad/s. Note that f_2 and f_4 are located inside a band gap, whereas f_1 and f_3 are located outside this bandwidth.

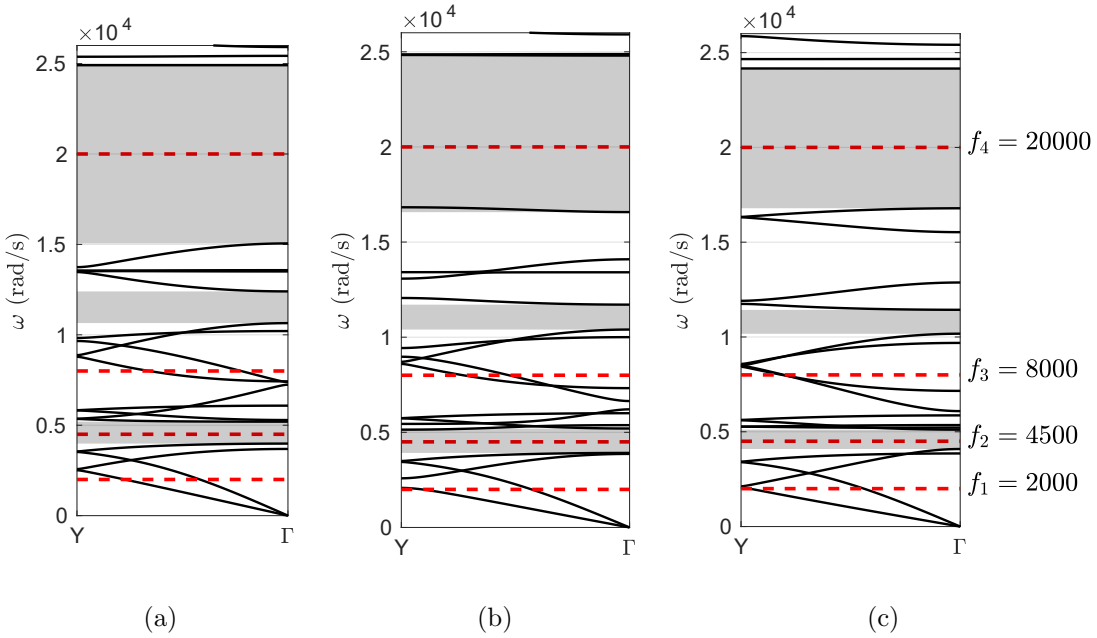

Figure 4.7. Selection of harmonic frequencies for super-cell analysis. f_1 and f_3 are selected outside a band gap, while f_2 and f_4 are selected inside. Dispersion curves in $Y\Gamma$ direction for (a) Open, (b) Intermediate and (c) Closed configurations.

Figure 4.8 shows snapshots of the displacement response of the open supercell under input excitations at different frequencies. For excitation frequencies f_2 and f_4, which are located inside the partial band gaps (see fig. 4.7) there is no energy propagation displaying the filtering capabilities of the material. By contrast, the response to excitations composed by harmonics of frequencies corresponding to f_1 and f_3 allows propagation along the complete domain. From the snapshots, we also observe a difference in group velocity between cases f_1 and f_3 which can also be identified in the dispersion relation shown in fig. 4.7. At frequency f_1 the dispersion curves have a steeper slope than at frequency f_3. It is also evident that since the material is now deployed over a finite domain, there is a limited effectiveness in filtering waves. On the other hand, examination of the snapshots suggests that the central bar plays a fundamental role in the response of the supercell as it prevents the propagation of waves in the frequency range near $f_2 = 4500$ rad/s. Additionally, it is observed that when the propagation is fully developed, the central and bottom bars oscillate 180° out of phase producing destructive interference. This is visible in the frames corresponding to t_2 and t_3. Figures 4.9 and 4.10 show the same set of snapshots for the remaining two configurations of the PXCM although, and as anticipated there are no appreciable differences in the response, as all three configurations are equivalent from the perspective of directional continuity.

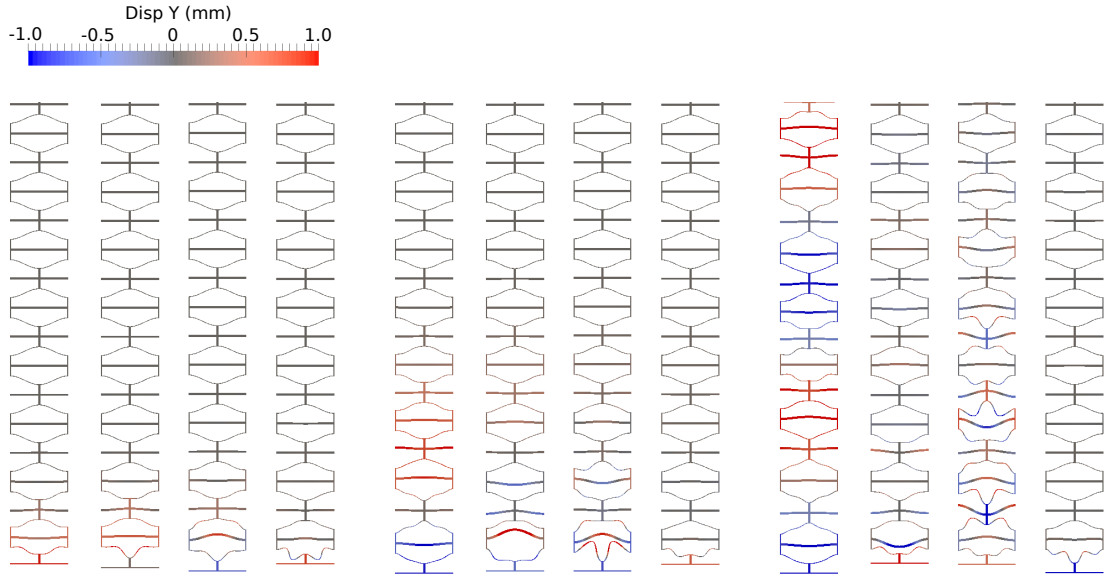

Figure 4.8. Snapshots of the open supercell excited with a harmonic prescribed displacement at times (a) $t_1 = 0.34$ms, (b) $t_2 = 1.12$ms and (c) $t_3 = 4.36$ms. At each time frame, excitation frequencies f_1 to f_4 from left to right.

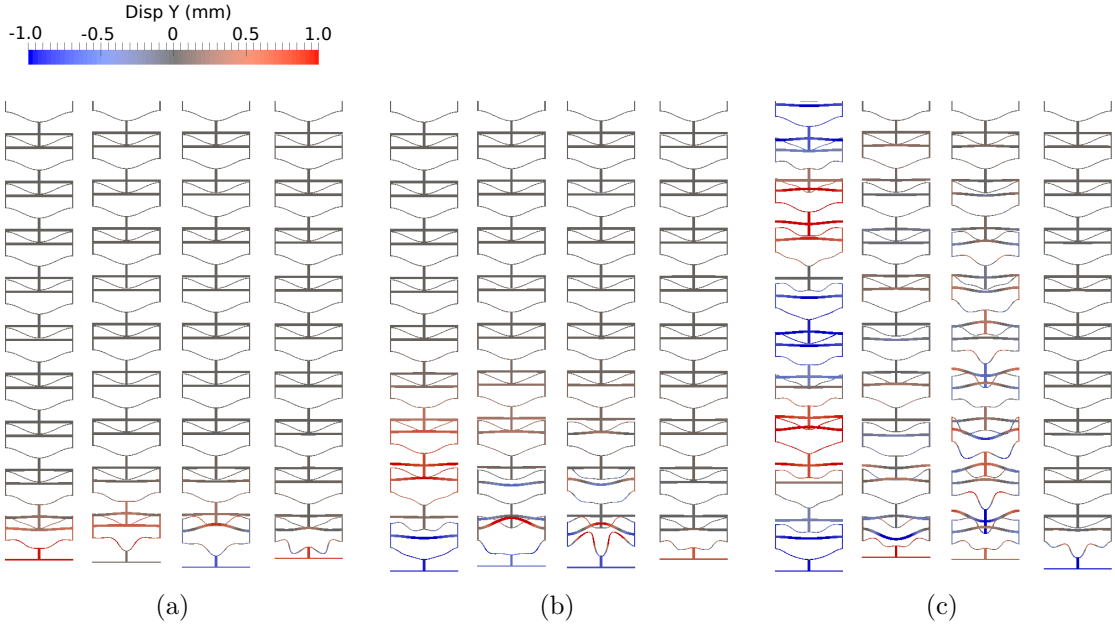

Figure 4.9. Snapshots of the semi-closed supercell excited with a harmonic prescribed displacement at times (a) $t_1 = 0.34$ms, (b) $t_1 = 1.12$ms and (c) $t_1 = 4.36$ms. At each time frame, excitation frequencies f_1 to f_4 from left to right.

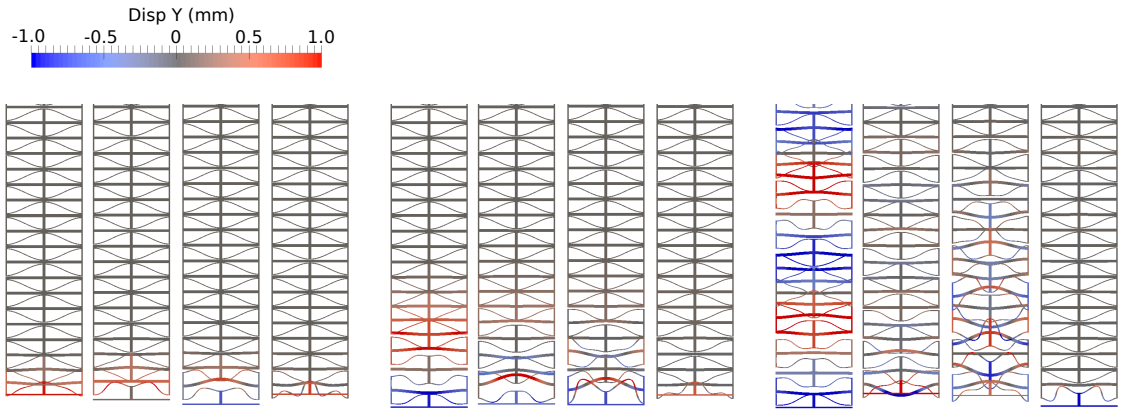

Figure 4.10. Snapshots of the closed supercell excited with a harmonic prescribed displacement at times (a) $t_1 = 0.34$ms, (b) $t_1 = 1.12$ms and (c) $t_1 = 4.36$ms. At each time frame, excitation frequencies f_1 to f_4 from left to right.

As an additional analysis, and in order to have a quantitative measure of the attenuation effectiveness of the material we computed the transmissibility in each excitation frequency and for each configuration of the unit cell. The results for each configuration are displayed in fig. 4.11 and these correspond to the ratios between maximum displacement response with respect to the amplitude imposed in the harmonic excitation. The response output was measured for a set of receivers located at the interface between adjacent cells as shown in the inset for fig. 4.11. In the f_2 case, inside a band gap, near 60% of the energy remains trapped in the first cell while in f_1 and f_3 cases, almost all the energy is transmitted from one cell to the other. The f_4 case is even more interesting, since 90% of the energy remains in the first cell. There is also a significant difference in the width of the band gaps containing f_2 and f_4. In the f_4 case, the band gap is wider than in the f_2 case. Then the attenuation capabilities of the material are more visible in f_4 case. This implies that fewer cells are needed to reach the same attenuation level when the excitation frequencies are inside wider band gaps.

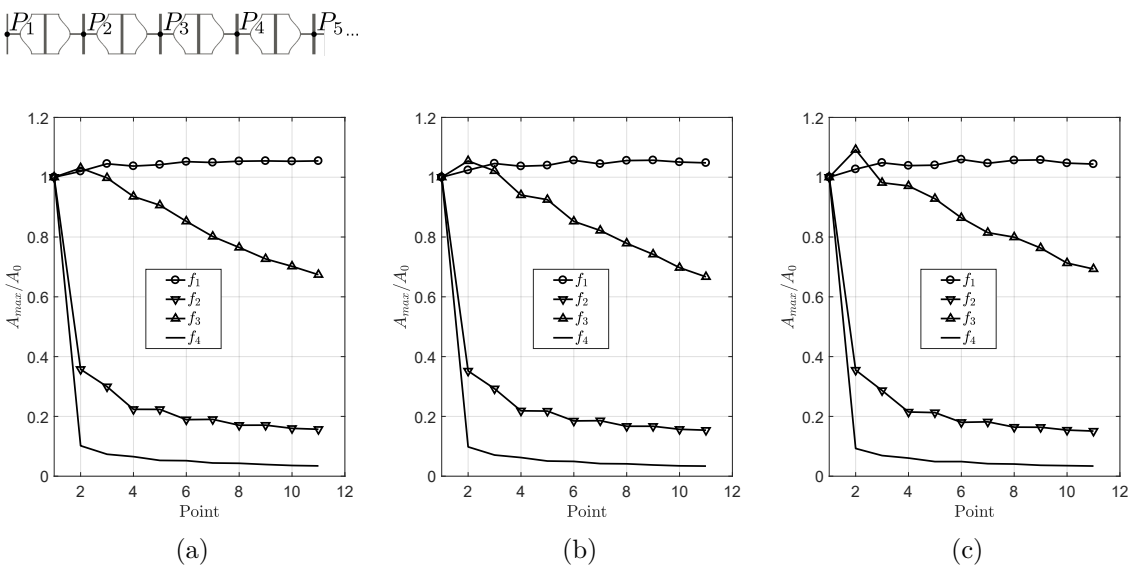

Figure 4.11. Maximum vertical displacement along some receivers in the supercells. (a) Open configuration, (b) semi-closed configuration, (c) closed configuration

4.2.4 Modal analysis and tuning of the first band gap

Transient simulations showed that the central bar moved out of phase with the sinusoidal segments for excitations in the two band gaps that were explored earlier. In this section, we investigate this connection further and use it to tune the band gaps in the $Y\Gamma$ direction for the PXCM material.

Salient mode shapes and frequencies from the modal analysis of a single unit cell in the open configuration are shown in column (b) of fig. 4.12. The motion of the unit cell is unrestrained in this analysis except the left and right edges, which are constrained to move only in the vertical direction. The modes shown here are chosen because they lie in the band gaps of the PXCM material for waves propagating in the vertical direction. We observe that the modes with frequencies $\omega_{u1} = 4823$ rad/s, $\omega_{u2} = 11243$ rad/s and $\omega_{u4} = 25389$ rad/s, all feature the central bar moving out of phase with respect to the sinusoidal beams. Two of these frequencies ($\omega_{u1} = 4823$ rad/ and $\omega_{u4} = 25389$ rad/s) are close to the band gap excitation frequencies that were used in the transient RVE simulations ($f_2 = 4500$ rad/s and $f_4 = 20000$ rad/s respectively). Recall that when the unit cell is subject to a harmonic excitation at a frequency near a natural frequency, we expect the corresponding mode to contribute significantly to the overall motion of the cell. Thus, we can establish a connection between the modes of a unit cell and band gaps in the $Y\Gamma$ direction for this PXCM.

We can take this reasoning a step further. A closer look at the modes corresponding to ω_{u1}, ω_{u2} and ω_{u4} shows that the deformation of the central bar in these modes of the unit cell is similar to that in the first three modes for a fixed-fixed beam in bending. The natural frequencies and mode shapes for these modes are shown in column (c) of figure fig. 4.12. The close correspondence between these frequencies and the band gaps in the $Y\Gamma$ direction for the PXCM suggests that these are *locally resonant bandgaps*

that arise when the frequency of excitation approaches the resonance frequencies of some structural elements in the cell (Celli & Gonella (2015); Liu et al. (2000); Sigalas & Economou (1992)). Such band gaps are associated with energy localization, which is consistent with our observations on the transient responses of the RVE in the previous section. We can now exploit the above correspondence to tune these band gaps.

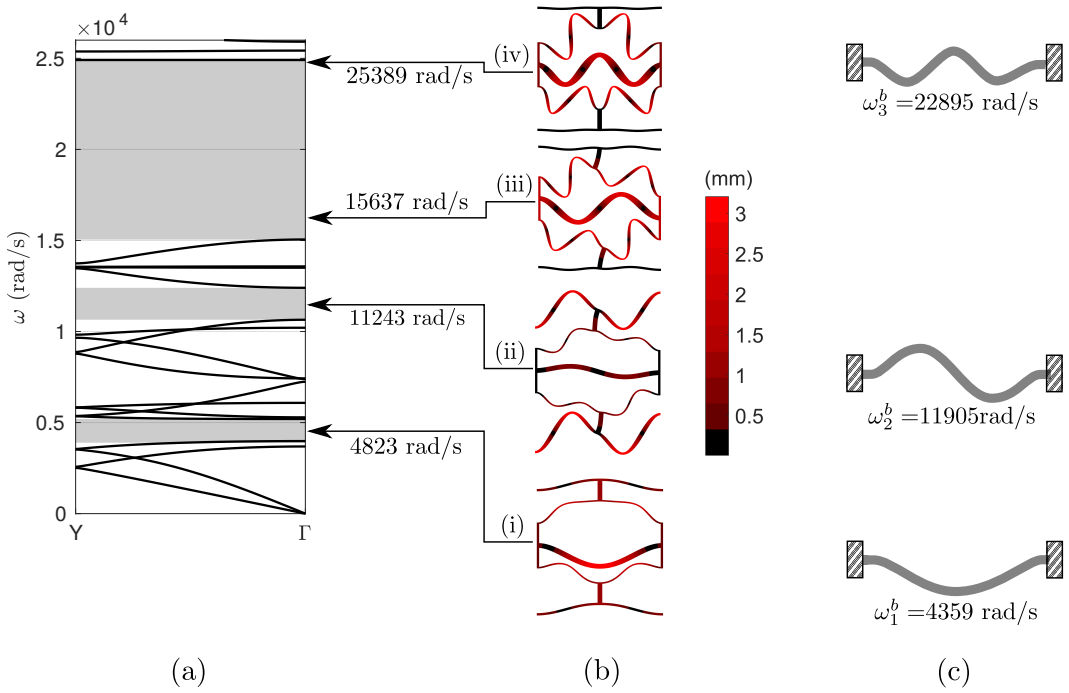

Figure 4.12. Modal response of the unit cell in the open configuration. (a) Dispersion diagram in the $Y\Gamma$ direction for open cell configuration. (b) Modal shapes and their frequency location inside the dispersion diagram. (c) First three fundamental modes of a fixed-fixed beam with geometric and material properties as the central bar.

The dynamic behavior of the central bar can be modulated by varying its material properties (e.g. modulus and density) or its geometry (e.g. cross-section dimensions, non-prismatic profile, etc.). Closed form analytical expressions can be used to estimate the natural frequencies of the central bar for any of these modifications. Thus, we can readily determine the magnitude and nature of the modifications needed to achieve a target band gap frequency for the PXCM. In this study, we chose to modulate the density of the material used for the central bar while keeping all other attributes of the central bar and the rest of the unit cell unchanged. This is indicated in fig. 4.13(a) by using a different color for the central beam as compared to the rest of the unit cell. Let ρ_c and ρ denote the densities of the materials used for the central beam and the rest of the unit cell respectively. We computed the dispersion diagrams for various values of the parameter $\bar{\rho} = \rho_c/\rho$ ratio in the range $[1.0, 10.0]$. Figure 4.13(c) shows the $Y\Gamma$ part of the dispersion diagram for salient values of this parameter. We note that a partial band gap in the $Y\Gamma$ direction does not exist around $\omega = 2000$ rad/s in

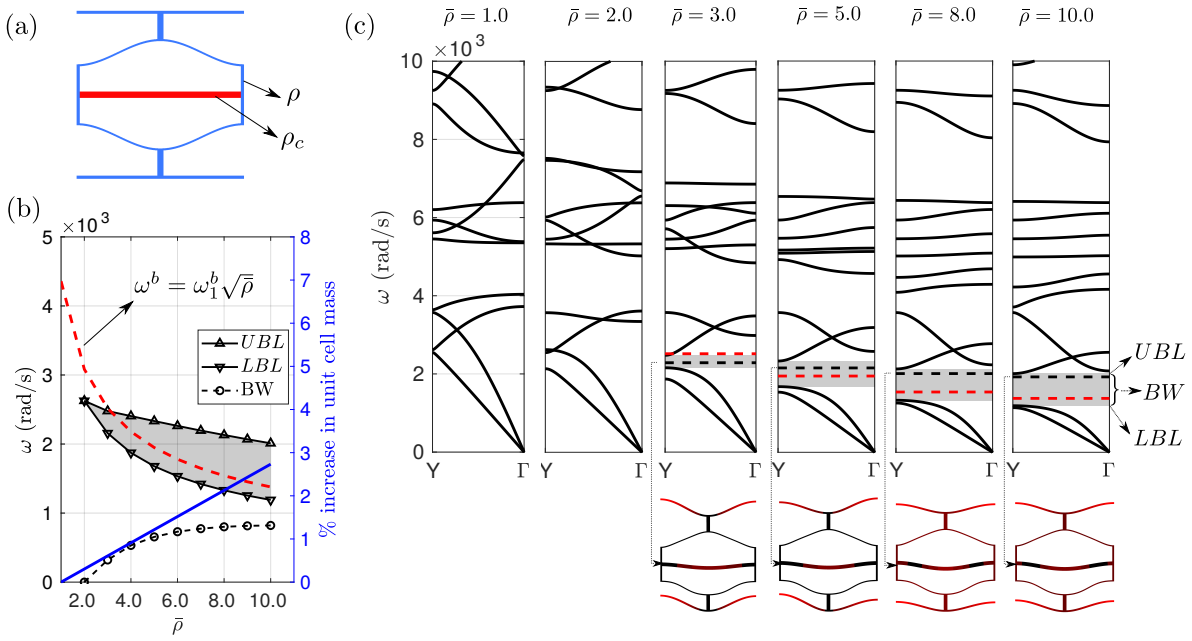

Figure 4.13. Modulating the partial band gap in the $Y\Gamma$ direction for the PXCM by varying the density of the material used for the central bar. (a) Unit cell geometry - blue region: density ρ, red region: density ρ_c. (b) Evolution of UBL, LBL and BW for the PXCM with increasing $\bar{\rho}$. (c) Dispersion relations for various values of $\bar{\rho} = \rho_c/\rho$. For values of $\bar{\rho} > 2.0$, a modal shape (which its frequency is plotted as a black dashed line inside the band gap) within the new band gap and involving the central beam, was always found. The red dashed line represents the first natural frequency of the central bar analysed as a fixed-fixed beam.

the original ($\bar{\rho} = 1.0$) unit cell; the lowest frequency band gap in the original cell is around $\omega = 4000$ rad/s. A partial band gap around $\omega = 2000$ rad/s does not appear until $\bar{\rho} > 2.0$. The band gap stretches from a lower limit of LBL to an upper limit of UBL (see fig. 4.13(c)). The band gap width is defined as $BW = UBL - LBL$. Further increases in the value of $\bar{\rho}$ beyond 2.0 lead to i) a monotonic reduction in both LBL and UBL, and ii) a concomitant monotonic increase in BW. This variation in the band gap frequency interval (especially, the LBL) closely follows the dependence of the first natural frequency for a fixed-fixed beam in bending on the density of the beam material. This dependence ($\omega^b = \omega_1^b/\sqrt{\bar{\rho}}$) is indicated on figure fig. 4.13(b) by a red dashed line.

The results in this section show that key insights gained from a step-wise deconstruction of the unit cell and transient analyses of an RVE enable us to tune the partial band gaps along the $Y\Gamma$ direction in the PXCM in a straightforward manner. Although, we illustrated this ability by tuning only the lowest band gap, it should be evident that the other resonance band gaps in the material's response can also be tuned in a similar manner.

Conclusion

We have studied the dispersive properties of a multi-stable cellular material (PXCM) in terms of its band diagrams and directional response. Such class of materials is attractive due to its inherent capability to dissipate energy by virtue of the geometric configuration of its microstructural elements which allows it to develop that ability through the phase change from one stable configuration to the other while the base material remains elastic. In addition to this appealing property the material can exhibit further dynamic attenuation introduced by its cellular periodic arrangement. To study the directional behaviour we used the novel method proposed in chapter 3, that takes information from several modes, as opposed to single mode biased methods. This new approach is useful as it allows to obtain highly representative descriptions of the directional response valid in the low and high frequency regime. We used the finite element method to conduct Bloch analysis in progressive (intermediate) geometries of the unit cell leading to the final PXCM. Based on the dispersion results, we investigated the filtering properties of the PXCM with time-domain simulations and a modal analysis. We found that band gaps along the vertical and horizontal directions of the PXCMs are explained in terms of material continuity concepts, while its properties (i.e., cut off frequencies, width, etc.) are related to the natural frequencies of local elements of the unit cell. Particularly, in the low frequency regime these band gaps are found to be controlled by the flexural modes of the central horizontal bar as suggested by super-cell and modal analyses. The material discontinuity in vertical direction and the resonant central bar, makes the PXCM suitable to be tuned in the same way that the one used in section 5.5, where we proposed a closed-form expression to control the location of a resonance band gap. Modification of the modal response of the central bar allowed us to fine-tune the associated band gaps. As a major result it was found that the dispersive properties of the PXCM remain invariant to the configuration of the cells due to its multi-stable nature. This may be understood as a good complement to the already appealing feature of the PXCM of dissipate energy through non-linear response while the base material remains elastic.

Chapter 5

Further work: some ideas to conduct a rational analysis of 2D periodic materials made up of beams

Introduction

In the preceding chapters of this work Bloch analysis was shown to be a powerful technique to study the elastodynamic response of periodic materials. We also formulated a very general computational framework in terms of a finite element implementation which was shown to be useful in conducting analysis of very general kinematic models. The framework is also powerful as it is easy to incorporate into commercial packages that admit user subroutines. With this numerical tool it is straightforward to find the dispersion relations for a predefined unit cell. In fact this set of tools was used in the analysis of the multi-stable cellular material of chapter 4. Despite of these undeniable capabilities for the analysis of periodic media, the big challenge from an engineering perspective still remains in solving the inverse problem. That is, finding a unit cell that matches prescribed dispersive properties. In this final chapter we explore and present as an approach for further work, some basic and fundamental ideas aimed at understanding the response of 2D periodic materials whose base elements are beams. The chapter does not include final nor definite results, however it is expected to pave the way for a deeper and rational exploration of popular 2D cellular materials where fine tuning capabilities are desired.

To study the basic mechanics of the frame-based 2D materials we followed a reductionist approach beginning with the review of an improved Timoshenko beam model (Timoshenko, 1921, 1922). After describing the possible propagating waves and dispersive properties of this simple fundamental material we used our numerical tools to focus on the response of a unit cell whose fundamental building block is precisely a

Timoshenko beam. Using the concepts from the single Timoshenko beam model we tried to separately control the group speed of longitudinal and transversely polarized motions. Although these motions are shown to resemble P and S waves they are not strictly P and S. From these analysis it was found that we can generate band gaps in a specific material by dropping the group speed of those motions resembling P waves. This was also shown to be achieved through what we have called *The continuity material concept*. The final part of the chapter compares the dispersive properties for a unit material cell modeled with beam elements and with plane strain idealizations. This is a natural questions as there is a great number of contributions where 2D analysis is conducted based upon this idealization. As a final result we propose a closed-form to control the location of a band gap in a specific unit cell.

Some of the unit cells analysed in this chapter have small structural elements modelled as beams. In those cases $b/L > 0.1$, then the Timoshenko model is appropriate. Periodic materials made of beams have been widely investigated since the 60's. Seminal contributions can be found in Heckl (1964); Lin & McDaniel (1969), where the authors studied dispersion in 1D periodic structures composed by beams. Some years later, Langley et al. (1997) extended the analysis to 2D periodic lattices combining theoretical, numerical and experimental techniques. More recently, Ruzzene et al. (2003); Ruzzene & Scarpa (2005) studied wave beaming effects and directional behavior of in two-dimensional cellular structures; then Gonella & Ruzzene (2008) extended the analysis to consider changes in the shape of the cellular structures, which modify the dispersive and directional behavior of the periodic material. Phani et al. (2006) studied different arrangements of 2D periodic structures made with beams. Here the authors analysed fuor different topologies of periodic structures, showing dramatic differences in their dispersion relations. Then they used homogenized properties to analyse the asymptotic values of the dispersion relations in the long wavelength regime. Finally, Liu & Hussein (2012) studied the transition between Bragg scattering and local resonance in periodic beams with different boundary conditions or periodic supports.

5.1 Wave propagation in a Timoshenko beam model

This section describes the band structure of a simple material model corresponding to a Timoshenko beam incorporating shear strains. To consider all possible motions the model is also enriched with axial deformations. From the dispersion relations for the material, which are derived from the governing equations of motion, it is observed that the material admits the propagation of 3 different types of waves, namely a longitudinal, a rotational and a bending wave . The dispersion relations are then used to find the group speeds of these possible waves.

5.1.1 Equations of motion

Figure 5.1 shows a differential element of a beam of cross section A, moment of inertia I, shear modulus G, Young's modulus E, mass density ρ and external force per unit length $q(x,t)$ undergoing transverse displacement w. In the considered Timoshenko beam

model it is assumed that plane sections normal to the neutral axis prior to deformation remain plane and at an angle ψ with the neutral axis after deformation. Note that due to the consideration of the shear strain γ_0 over the cross section, the angle ψ is given by:

$$\psi = \frac{\partial w}{\partial x} - \gamma_0. \tag{5.1}$$

This improved beam-theory model should be contrasted with the classical Euler-Bernoulli beam model where shear strains are neglected resulting in:

$$\psi = \frac{\partial w}{\partial x}.$$

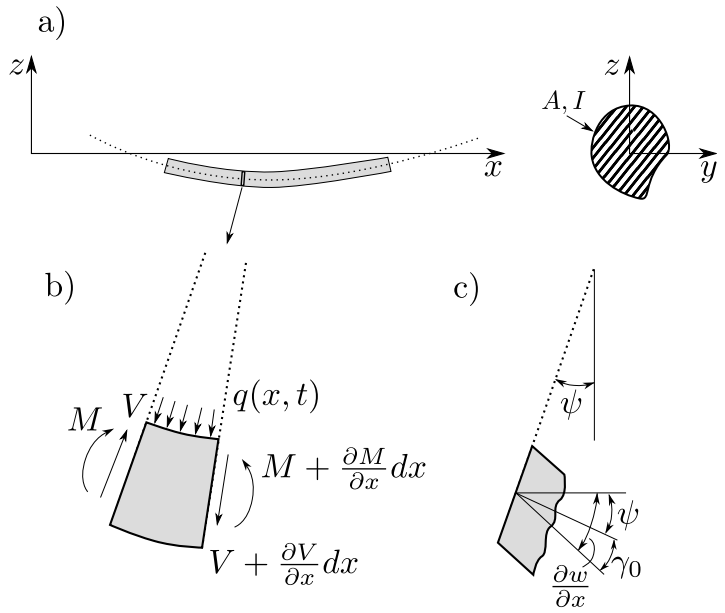

Figure 5.1. Infinite unsupported beam undergoing flexural motion. (a) Beam and cross-section with geometric properties A and I and it is restricted to symmetric shapes. (b) Differential element of the beam subjected to load. (c) Kinematical details of shearing deformation.

Consider the force and moment equilibrium for a differential element of size dx and where M and V are the internal moments and internal shear forces. Using the proper force-displacement relations these equations yield, (Graff, 1976):

$$GA\eta\left(\frac{\partial \psi}{\partial x} - \frac{\partial^2 w}{\partial x^2}\right) + \rho A \frac{\partial^2 w}{\partial t^2} = q(x,t) \tag{5.2}$$

$$GA\eta\left(\frac{\partial w}{\partial x} - \psi\right) + EI\frac{\partial^2 \psi}{\partial x^2} = \rho I \frac{\partial^2 \psi}{\partial t^2} \tag{5.3}$$

In eq. (5.2) and eq. (5.3) η is the Timoshenko shear coefficient introduced to compensate for the assumption of constant shear strain over the cross section. This coefficient can be derived for a given cross section using a force balance relation like:

$$V = G \int_A \gamma dA = (G\gamma_0 A)\eta.$$

In this work η is computed as defined by Cowper (1966). Equations (5.2) and (5.3) are the equations of motion for the Timoshenko beam theory.

For the analysis that follows, it is also convenient to consider the axial (or longitudinal) response of the beam element. The corresponding equation of motion follows from equilibrium considerations along the longitudinal direction giving:

$$E\frac{\partial^2 u}{\partial x^2} + p = \rho\frac{\partial^2 u}{\partial t^2}, \tag{5.4}$$

and where $u(x,t)$ is the axial displacement of a material point in the beam and p is an axial force per unit length.

5.1.2 Dispersion relations

Dispersion properties in terms of ω vs κ curves for the beam model can be derived after assuming that motion is a plane wave of the form

$$() = Ae^{i(\mathbf{k}x-\omega t)}.$$

with amplitude A, constant angular frequency ω and wave vector $\mathbf{k}$. Using the specific representations

$$\begin{aligned} u(x,t) &= Be^{i(\mathbf{k}x-\omega t)} \\ w(x,t) &= B_1 e^{i(\mathbf{k}x-\omega t)} \\ \psi(x,t) &= B_2 e^{i(\mathbf{k}x-\omega t)} \end{aligned}$$

in 5.4, 5.2 and 5.3 respectively yields after dropping the load terms:

$$\omega = c\mathbf{k} \tag{5.5}$$

and

$$\frac{EI}{\rho A}\mathbf{k}^4 - \frac{I}{A}\left(1 + \frac{E}{G\eta}\right)\mathbf{k}^2\omega^2 - \omega^2 + \frac{\rho I}{GA\eta}\omega^4 = 0. \tag{5.6}$$

which are the dispersion relationships associated to the axial and bending kinematic assumptions introduced previously. Note that in the derivation of the dispersion relationship associated to beam bending, the transverse motions w and section rotations ψ were assumed like independent plane waves. However, enforcing the condition:

$$\psi = \frac{\partial w}{\partial x} - \gamma_0$$

results in a single dispersion relationship from 5.2 and 5.3. The details of the computation leading to eq. (5.6) can be found in Graff (1976).

Equation 5.6 can be written in the compact form

$$C_1\mathbf{k}^4 - C_2\mathbf{k}^2\omega^2 - \omega^2 + C_3\omega^4 = 0$$

and then solved for ω^2 to arrive at the following ω vs κ relationship

$$\omega^2 = \frac{C_2\mathbf{k}^2 - 1}{2C_3} \pm \frac{1}{2C_3}\sqrt{\left(C_2\mathbf{k}^2 + 1\right)^2 - 4C_1C_3\mathbf{k}^4}. \tag{5.7}$$

Solving the dispersion relation in the form $\omega \equiv \omega(\mathbf{k})$ yields positive and negative real roots corresponding to rightward- and leftward-propagating harmonic waves. Taking the positive real solution and considering also the positive and negative internal signs results in two curves corresponding to different wave modes. These curves were plotted in fig. 5.2 for the case of an aluminium beam with properties corresponding to $E = 73\times10^{10}\text{Pa}$, $\nu = 0.325$ and $\rho = 2770\text{kg/m}^3$ and cross-sectional properties of $A = 0.01\text{m}^2$ and $I = 6.33 \times 10^{-4}\text{m}^4$. In the figure we considered also the linear relationship given in eq. (5.5) with $c = \sqrt{E/\rho}$ corresponding to the longitudinal mode associatted with the displacement component u. The remaining curves in the figure correspond to the waves associatted to the transverse displacement w and to the section rotation ψ. In what follows, we will refer to these wave modes as bending waves and rotational waves respectively.

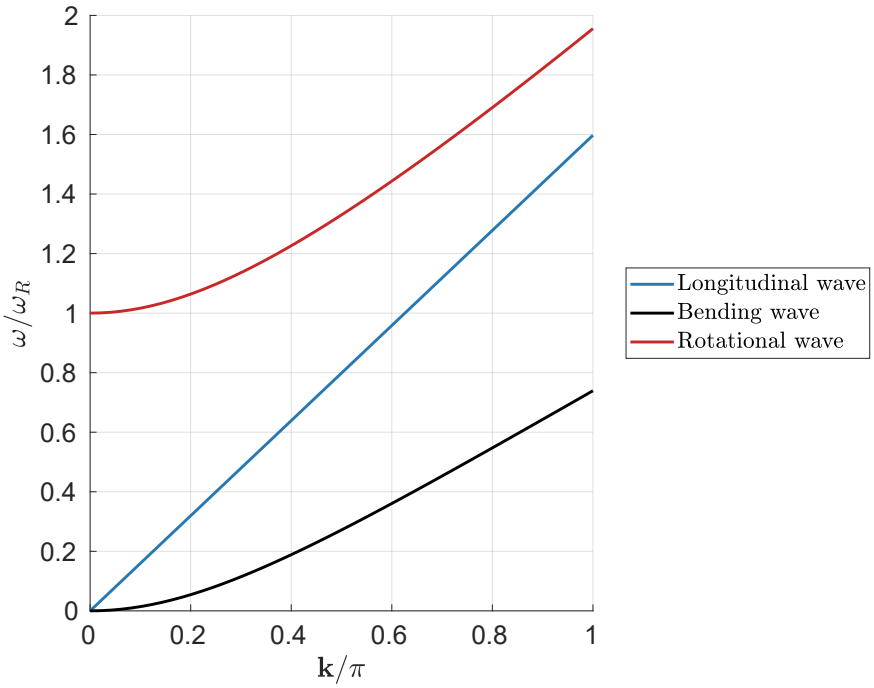

Figure 5.2. Dispersion curves for a beam made of aluminium. Longitudinal and flexural waves are depicted in the same plot.

The rotational wave associatted to ψ has a cut-off frequency

$$\omega_R = \sqrt{\frac{GA\eta}{\rho I}} \tag{5.8}$$

while for the bending wave

$$\omega_B = 0. \tag{5.9}$$

The frequencies corresponding to $\mathbf{k} = 0$ are found after solving eq. (5.7) in the long wavelength limit ($\mathbf{k} \to 0$). According to these results, a very long bending wave ($\mathbf{k} \approx 0.0$) cannot propagate through the beam since its group speed (slope of the dispersion curves) is zero.

5.1.3 Group speed

The group speeds for the waves present in the Timoshenko beam material model, can be computed from eq. (5.7) after calculating $\partial\omega/\partial\mathbf{k}$. Applying the chain rule to eq. (5.7) yields

$$\mathbf{C_{B,R}} = \frac{\partial\omega}{\partial\mathbf{k}} \equiv \frac{1}{2\omega} f'(\mathbf{k}) \tag{5.10}$$

where ω is the positive real solution of eq. (5.7) plotted in fig. 5.2 and

$$f'(\mathbf{k}) = \frac{C_2\mathbf{k}}{C_3} \pm \frac{1}{2C_3}\left[\frac{1}{2S(\mathbf{k})}\left(4C_2^2\mathbf{k}^3 + 4C_2\mathbf{k} - 16C_1C_3\mathbf{k}^3\right)\right],$$

with

$$S(\mathbf{k}) = \sqrt{\left(C_2\mathbf{k}^2 + 1\right)^2 - 4C_1C_3\mathbf{k}^4}.$$

The constants $C_\bullet$ are those implicitly defined in eq. (5.7). On the other hand, $\mathbf{C_{B,R}}$ in eq. (5.10) takes the value of group speed of the bending or rotational waves according to the sign of ω and $f'(\mathbf{k})$.

The group speeds for the longitudinal, bending and rotational waves are plotted in fig. 5.3. In the figure the wave number axis is extended by a factor n, which is useful to show the asymptotic behavior of the group speed. When the shear stiffness becomes infinite (zero shear strain) the beam behaves as an Euler-Bernoulli beam resulting in an unbounded group speed for the bending wave. As pointed out by Graff (1976) this results in an illed-condioned medium where an applied pulse inmediatly appears in the far field. The assymptotic values of the group speeds are found by making $\mathbf{k} \to \infty$ in eq. (5.10) leading to

$$\mathbf{C_R^\infty} = \mathbf{C_L}; \qquad \mathbf{C_B^\infty} = \sqrt{\frac{G\eta}{\rho}} \tag{5.11}$$

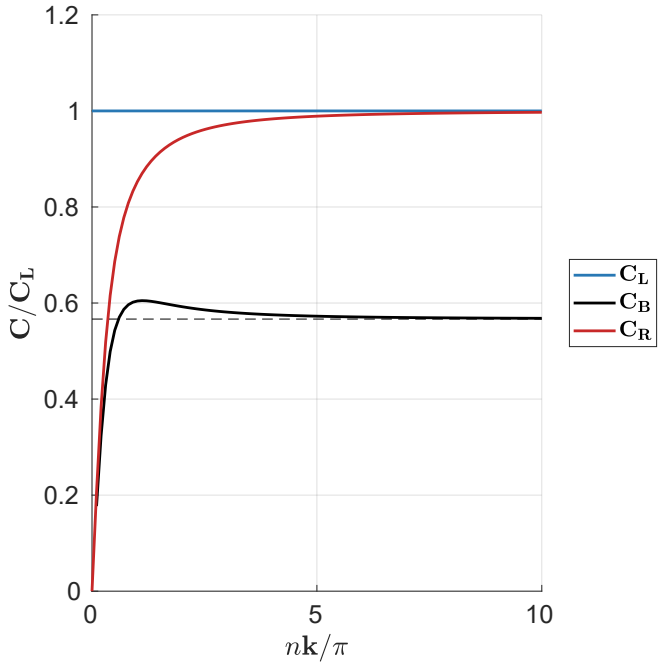

Figure 5.3. Group speed of longitudinal and flexural waves in an infinite unsupported beam. Note the asymptotic behavior of group speed.

Two observations are relevant when $\mathbf{k} \to \infty$. First, the bending and rotational wave becomes non-dispersive at long wavelengths, and second the rotational wave propagates at the same group speed as the uncoupled longitudinal wave. On the other hand, at high frequencies waves do not interact with the geometry of the beam as the wavelengths are so small in comparisson to the the beam dimensions that they propagate as in a free space.

Since the bending and rotational waves have transverse polarization when propagating through the beam, the values of A and I are expected to affect their group speed. Assume a rectangular cross section with dimension $a \times b$. From eq. (5.6), it is evident that the geometric properties are always related as I/A. Furthermore, for a rectangular cross section it folllows that $I/A \propto b^2$; then a will not have any incidence on the group speed and the only required variation is in the height parameter b. The group speeds for 3 different values of the height paramter, labeled as 1, 2 ,3 are shown in fig. 5.4.

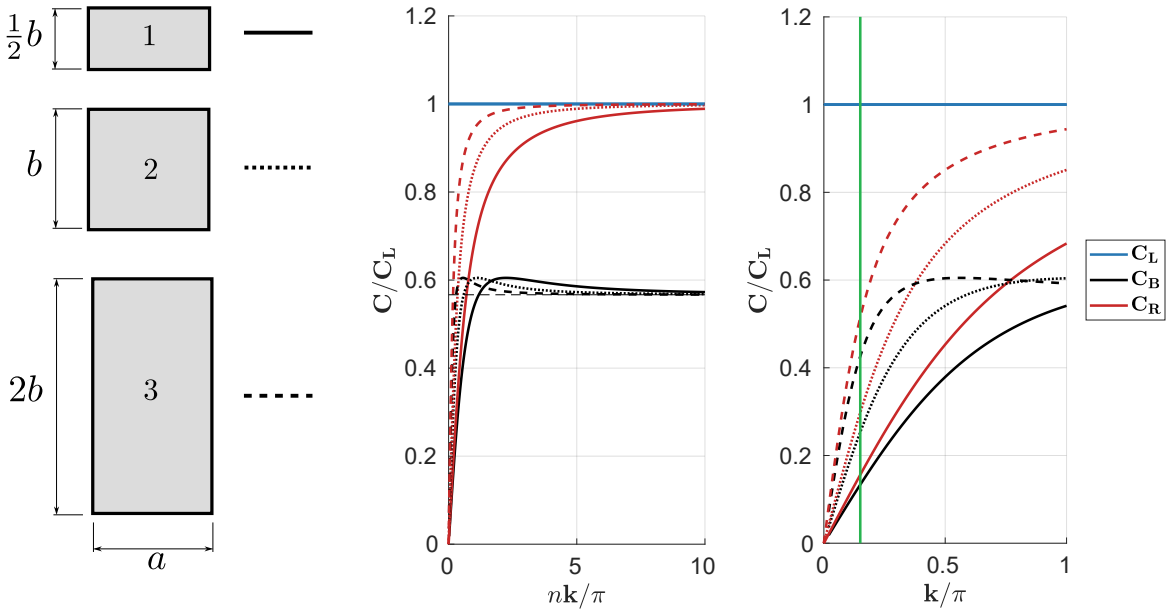

(a) Variations on b

(b) Results of the variations on b

(c) Zoom on the results

Figure 5.4. Variation of group speed of longitudinal and flexural waves in the beam for various values of cross-sectional height. A base value $b = 0.01$m was used. Following the previous color convention; blue, black and red curves represent longitudinal, bending and rotational waves respectively. Dashed line: $2b$, dotted line: b and solid line: $b/2$.

As expected, only the group speed of the bending and rotational waves waves are sensible to changes in geometric properties. In order to find a relation between changes in the cross section dimensions and changes in the group speed, we did a simple dimensional analysis of the geometric terms (A, I) appearing in eq. (5.10). It was found that for low wave number values, i.e. when the group speed is nearly linear, the slope of

eq. (5.10) is proportional to $\sqrt{I/A}$ which is equivalent to the prediction using Euler-Bernoulli theory. This last relation is valid for any cross-sectional shape as eq. (5.10) is general.

5.2 Finite element modeling of a periodic beam element

This section describes for completeness the verification of the finite element implementation of the Timoshenko beam element within the context of Bloch analysis. The numerical implementation is required in order to study periodic materials whose base elements are beams. The beam element was implemented as a user element subroutine in the finite element code FEAP. The verification problem compares the closed-form dispersion relations obtained after applying Bloch theorem to a material cell of a Timoshenko beam and the corresponding results obtained with the finite element implementation.

5.2.1 Analytical periodic beam

Conisder the infinite Timoshenko beam shown in fig. 5.5. The beam can be assumed like a periodic material model conformed by successive unitary beams of length $2d$.

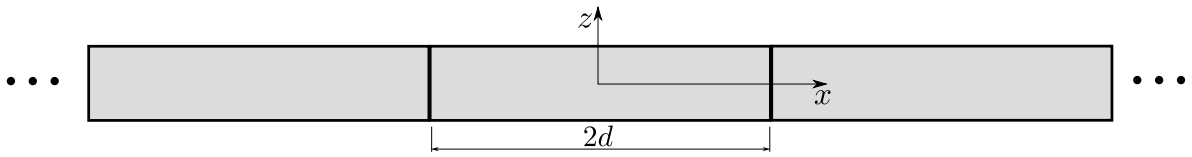

Figure 5.5. Scheme of a periodic homogeneous beam of length $2d$. The previous infinite beam is now represented as a repetition of a finite-sized beam in both directions (left and right).

The dispersion relationships for the beam considering the Bloch periodic boundary condition is obtained after using the information from different Brillouin zones of the form

$$\omega_m \equiv \omega(\mathbf{k}_m), \tag{5.12}$$

in the disepersion relations given in eq. (5.7). Here the subscript m corresponds to an integer number referring to waves coming from adjacent Brillouin zones. In the case of a unit cell from a 1D periodic material, the following definition of the wave number applies (Langlet, 1993):

$$\mathbf{k}_m = \left(k_x + \frac{m\pi}{d}\right), \tag{5.13}$$

where k_x is the wave vector and takes values $k_x = [0, \pi/2d]$ covering the first Brilloun zone. The dispersion curves considering Bloch boundary conditions are shown in fig. 5.6 for the beam of rectangular cross section. The resulting curves show information from adjacent unitary beams.

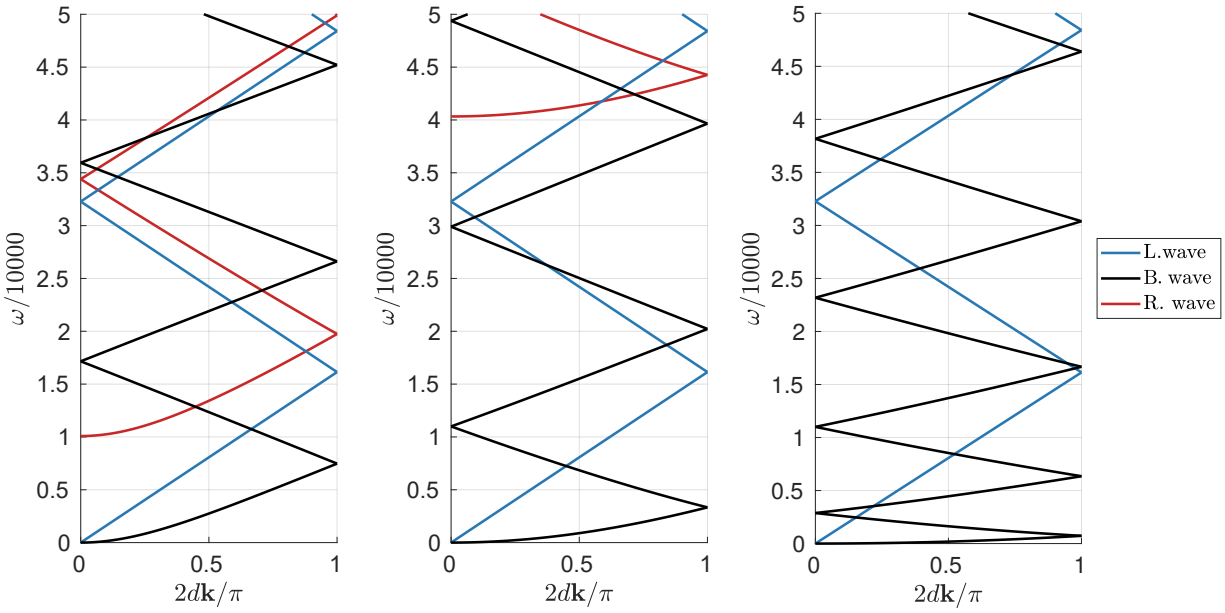

(a) $b = 1.0$m (b) $b = 0.25$m (c) $b = 0.05$m

Figure 5.6. Dispersion relations in the first Brillouin zone for a periodic beam of length $2d$. The geometric parameter b is varied to show the variation of group speed of shear waves in the dispersion relations.

5.2.2 Numerical periodic beam

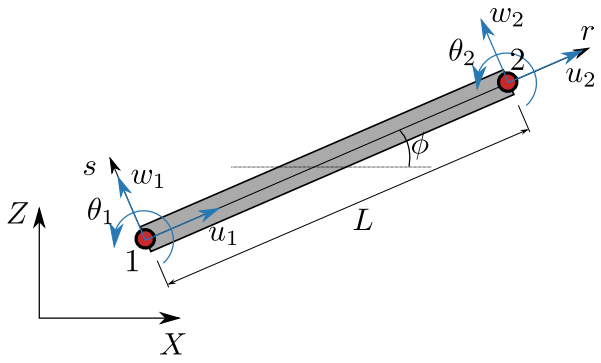

Figure 5.7. Details of the two-noded beam element implemented in FEA. It is a Timoshenko beam element coupled with a classic frame element oriented in a general angle ϕ.

The numerical framework to compute dispersion relations in periodic beams was implemented in the user element subroutine described chapter 2. The element is a displacement-based two-noded beam (fig. 5.7) following the formulation from Friedman

& Kosmatka (1993) in terms of cubic and quadratic Lagrangian polynomials to interpolate transverse and rotational displacements respectively. The element also includes axial displacements representing longitudinal waves through the beam (Przemieniecki, 1985). The numerical implementation was verified against the analytical solution using the same parameters as for the cases shown in fig. 5.6. The results from the verification are presented in fig. 5.8 and show a good agreement with the analytical solution.

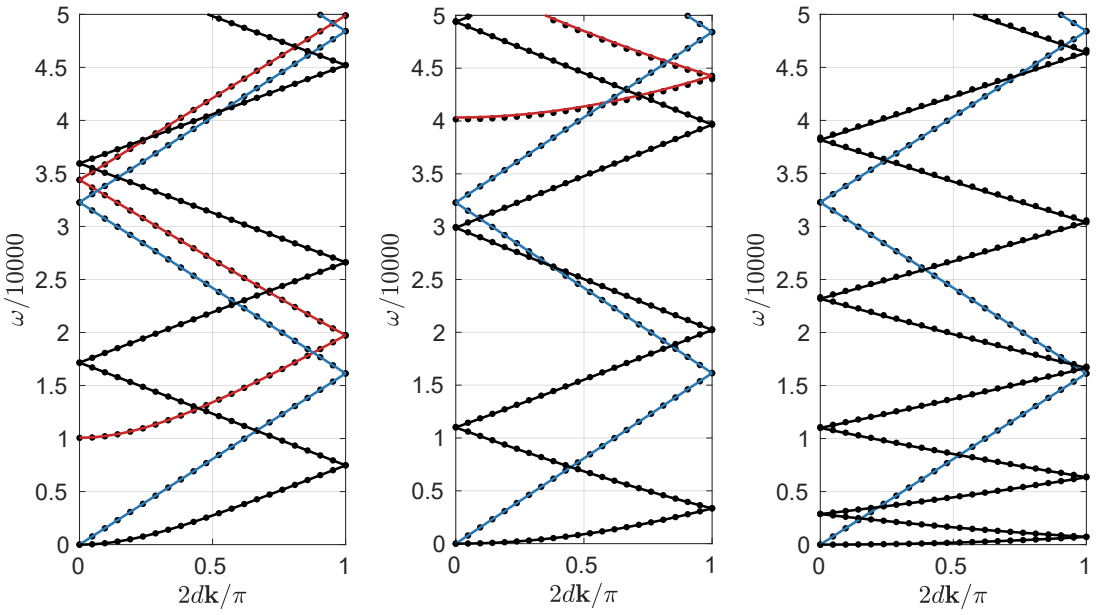

(a) $b = 1.0$m (b) $b = 0.25$m (c) $b = 0.05$m

Figure 5.8. Comparison between analytically and numerical results of dispersion in a periodic beam. Solid lines correspond to analytical solutions and dots correspond to the numerical solution. The parameters used to make this comparison were the same as in fig. 5.6.

5.3 A simple 2D periodic structure made of beams

This section is devoted to the investigation of the response of a simple bi-dimensional periodic material whose base elements are Timoshenko beams. The section starts with the definition of the unit cell and the numerical computation of the band structure for the unit cell. This dispersion characterization is then analyzed using the concepts discussed in the previous section complemented by a study of the modal response of the full cell and the local beams. The final introduces a geometric perturbation to the cell in order to obtain a target band structure.

5.3.1 Unit cell and dispersion results

The simple two-dimensional periodic material is shown in fig. 5.9a. The base elements are aluminum Timoshenko beams with a rectangular cross section $a \times b$, with $b = 0.01$m while the unit cell has dimensions $2d \times 2d$ where $2d = 1$m . Figure 5.9b-c show the unit cell geometry and its first Brillouin zone respectively. The band structure computed by the finite element based user subroutine discussed previously is shown in fig. 5.10 over the IBZ illustrated in fig. 5.9c. For simplicity all the analyses that follow are restricted to the horizontal ΓX direction.

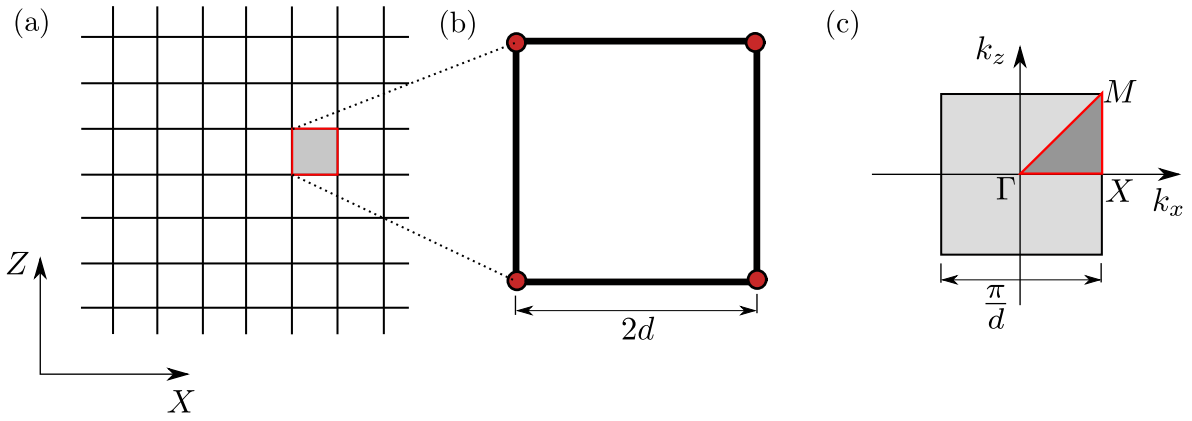

Figure 5.9. Two dimensional squared frame. (a) Periodic reticular material made of beams. (b) Unit cell composed by four beams. (c) First and Irreducible Brillouin zones in the wave number domain.

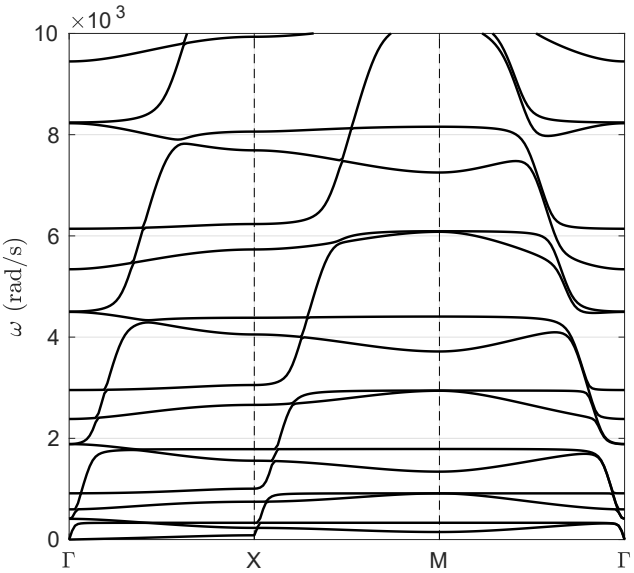

Figure 5.10. Dispersion curves for a squared frame made of beams over the IBZ. Not complete nor partial band gaps are detected.

5.3.2 Analysis of the dispersion relations in ΓX direction

The fundamental concepts identified in section 5.1 are now used in the analysis of the band diagram of the full cell using the conventions described in fig. 5.11. The left part of the figure shows a motion originally polarized in the form of a P wave along the horizontal (ΓX direction) with displacements parallel to the propagation direction. As described in the figure, this motion is expected to impart local modes corresponding to a longitudinal wave in the horizontal element and transverse modes, corresponding to bending and rotational waves in the perpendicular elements. Similarly, the figure on the right shows a motion along the horizontal ΓX direction but now polarized like an S wave. This motion is expected to impart local modes corresponding to a longitudinal waves in the elements normal to the direction of propagation, and transverse modes, corresponding to bending and rotational waves in the elements parallel to the direction of propagation. These modes are inidcated in the figure by the letters L and T placed in the corresponding elements. In general, beam elements parallel to the global polarization are excited by a local longitudinal mode and beam elements perpendicular to the global polarization are excited by a local transverse mode in the form of bending and rotational waves.

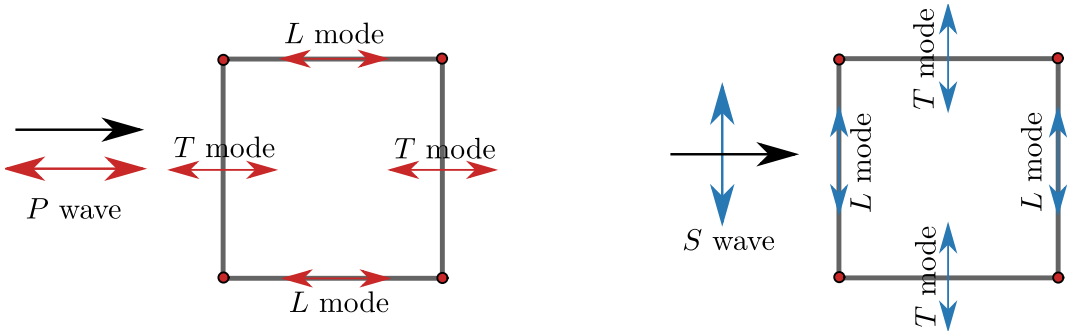

Figure 5.11. Definition of global propagating waves through the frame and effects on local beams composing the frame. A global wave (P or S) can trigger local longitudinal (L) and transverse (T) modes on the beams. The black arrows represent the direction of propagation whereas blue and red arrows represent the polarization of P and S waves respectively, propagating along ΓX direction.

Global and local vibration modes for the 2D frame are shown in fig. 5.12. The color code used in the results represents the amplitude of the displacement field in such a way that fully red or blue contours describe pure horizontal or vertical displacements respectively, while a magenta-like contour represents mixed displacement fields. The deformed frames in fig. 5.12a are the global modal shapes associated with the eigenvalues at $\mathbf{k} = 0.0$. It is observed that the first global mode, with natural frequency $\omega = 409\text{rad/s}$, shows a mixed-colored response consistent with a combination of horizontal and vertical displacement components. The remaining modal shapes exhibit a response with fully red or blue elements which is consistent with the presence of local modes. On the other hand the local modes for a fixed-fixed beam element, computed as described in the appendix, show local frequencies located at points in the band diagram where

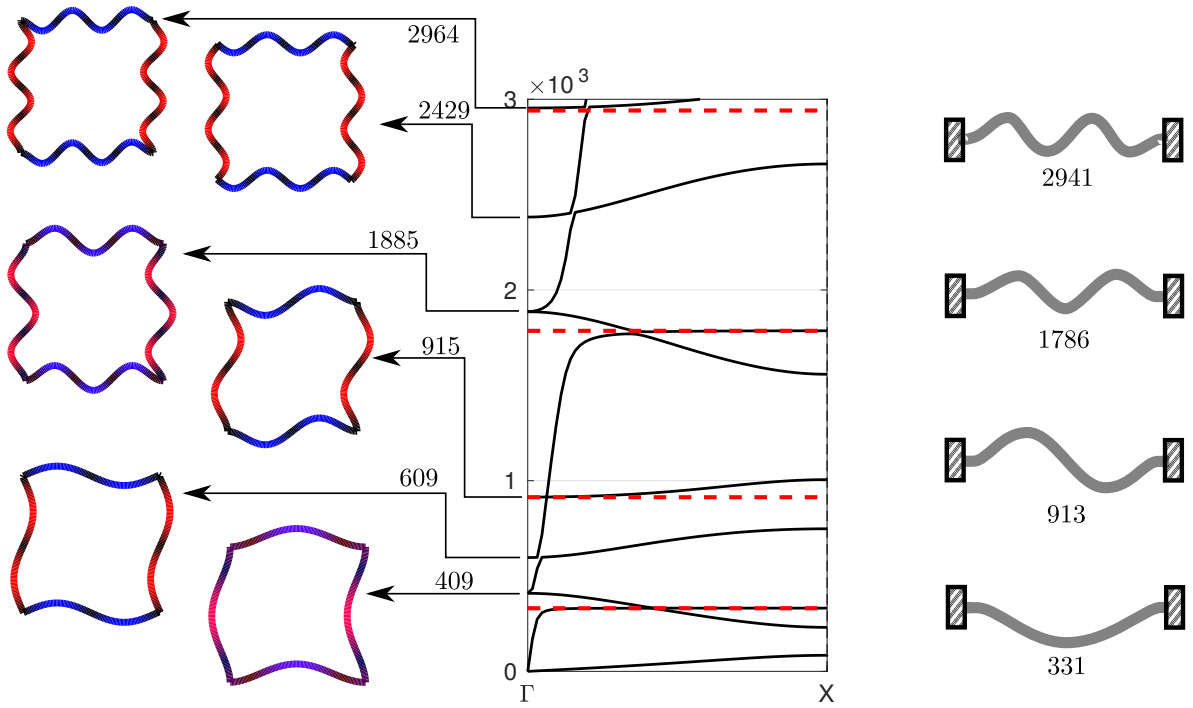

Figure 5.12. Local and global modal shapes. (a) Global modal shapes and frequencies of the frame at $\mathbf{k} = 0.0$. Red color: horizontal displacement. Blue color: vertical displacement. (b) Dispersion relations of the frame in ΓX direction. The red dashed lines correspond to the local frequencies shown in (c). (c) Local modal shapes of a fixed-fixed beam with the same properties as the beams composing the frame. All frequencies in rad/s

the group speed is zero (indicated by the red dashed line in the figure). Some of these local modes are nearly coicident with those in the global response. For instance, the second local mode at 913 rad/s is close to the global mode at 915 rad/s; the fourth local mode at 2941 rad/s is close to the global mode at 2964 rad/s. The global modes at 915 rad/s and 2964 rad/s, show the local beams conforming the frame vibrating with the same shape as the local beam at 913 rad/s and 2941 rad/s respectively.

The previous set of results suggests that every point in the dispersion relation of the periodic frame, can be expressed as a combination of local longitudinal and transverse modes corresponding to local bending and rotational waves. To verify this aspect of the response, some salient modal shapes associated with the band diagram are plotted in fig. 5.13. It shows that modal shapes consistent with an S wave branch, are always fully blue or red. On the other hand, when the modal shape belongs to a P wave branch, it results in a magenta-colored response. *This result is indicative of the fact that global S waves only trigger local transverse modes whereas global P waves can trigger both, longitudinal and transverse modes.*

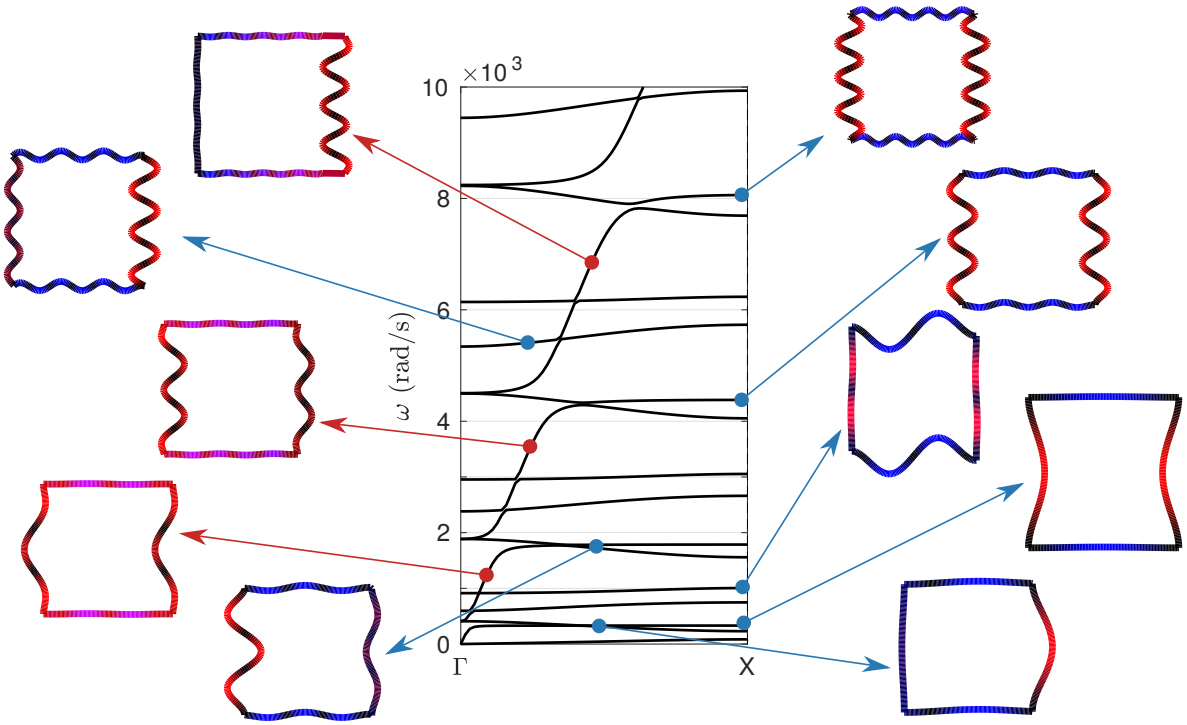

Figure 5.13. Global modal shapes of the frame with BBC applied with different values of k_x. Red color: horizontal displacement. Blue color: vertical displacement. The arrows in each modal shape point from their actual frequency in the dispersion relations. Blue and red arrows point from modal shapes related to S and P wave branches respectively. Modal shapes associated to P wave branches, always have magenta color; which means a combination of local longitudinal and transverse modes.

5.3.3 Controlling the group speed of the global P and S waves

According to the results from the single beam, the group speed of bending and rotational waves is proportional to $\sqrt{I/A}$. On the other hand, P waves were shown to be related to local longitudinal modes which are not dependent upon cross-sectional properties. Thus it can be easily concluded that it is necessary to modify the axial stiffness of the local beams in order to control the group speed of the global P wave. This can be acomplished by (i) changing the base material of the beams or (ii) changing the stiffness in a specific prescribed direction by introducing geometric changes to some specific elements.

Controlling the group speed of S waves

Figure 5.14 shows the dispersion relations for the frame using different heights b of the rectangular cross section of the local elements. The change in the group speed of the S waves is evidenced by the changes in the number of branches and in the slope of the first S branch. As expected, the group speed increases with b. It must be observed that the group speed of the P wave remains unchanged.

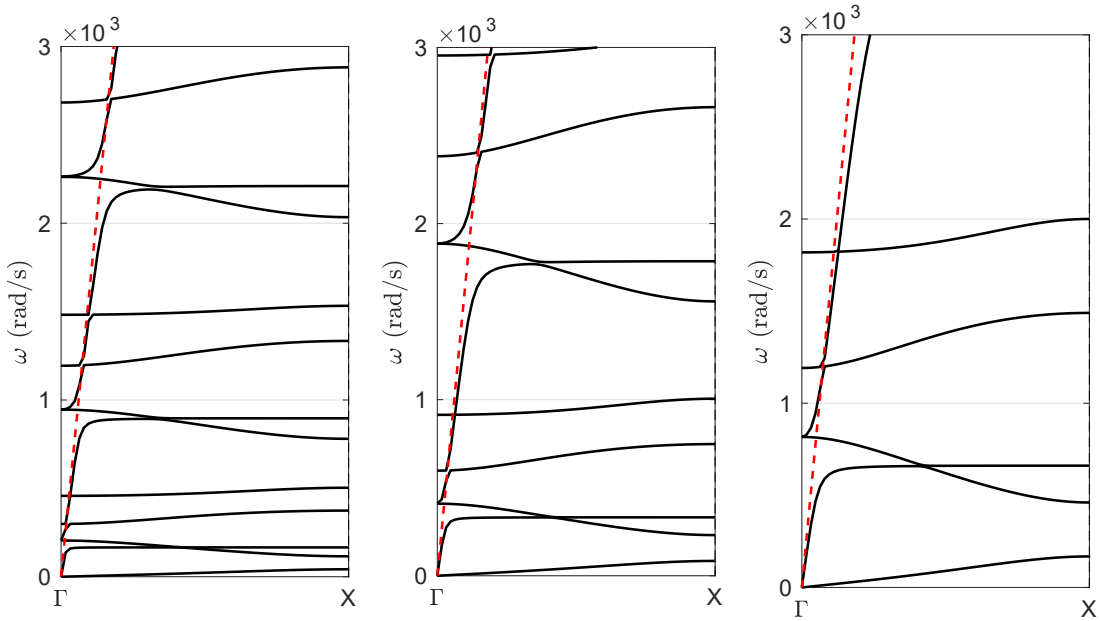

(a) $b = 0.005$m (b) $b = 0.01$m (c) $b = 0.02$m

Figure 5.14. Variation of group speed of S waves by varying the cross sectional properties. The red dashed line is a physical reference, which represents the group speed of longitudinal waves in a local beam, dictated by $\sqrt{E/\rho}$.

Controlling the group speed of P waves

To introduce changes to the group speed of the P wave, components changes are now introduced into the local elements in terms of the geometric perturbation shown in fig. 5.15. As h increases, the unit cell becomes"softer" in the horizontal direction. The dispersion results for different values of h, shown in fig. 5.16, illustrate how the group speed for the P wave branches is affected. It is evident how these branches fall down for high values of h while those for the S waves remain constant. It is clear that the geometric perturbation also modifies the path of propagation of the S waves along the original horizontal beams introducing small variations in the S wave branches. An interesting result from this analysis was found in fig. 5.16a. For $h = b$, a small band gap appears near $\omega = 2 \times 10^3$rad/s and it grows with h. This band gap is somehow affected by the geometric perturbation.

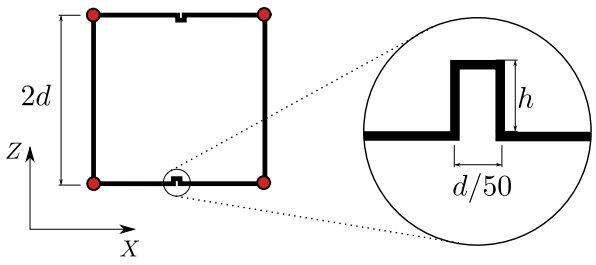

Figure 5.15. Illustration of the geometric perturbation h. The unit cell becomes softer in horizontal direction when h increases.

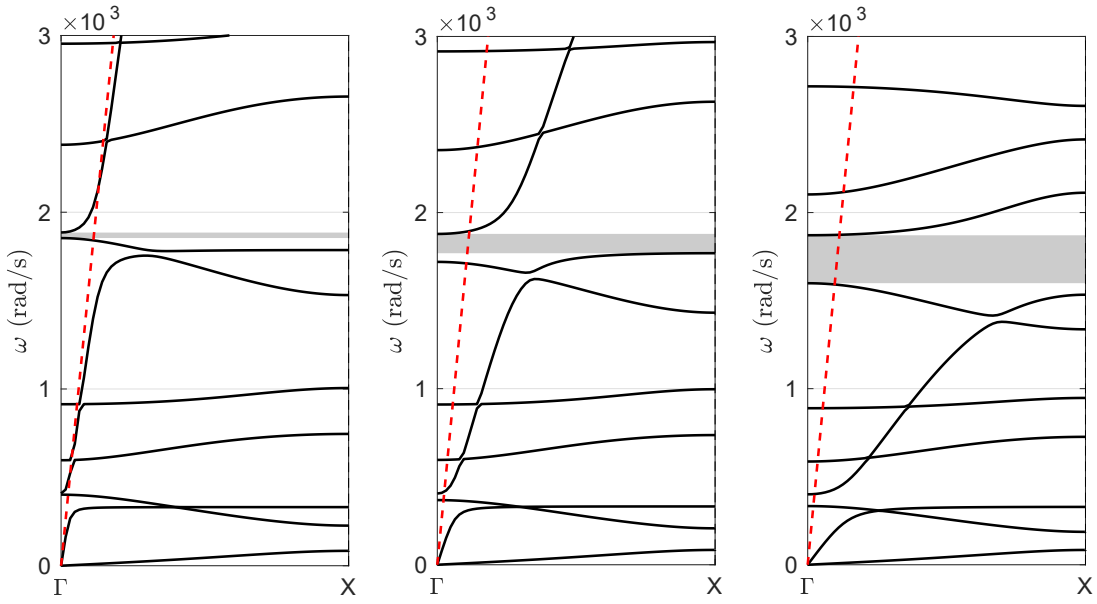

(a) $h = b$ (b) $h = 5b$ (c) $h = 10b$

Figure 5.16. Variation of group speed of P waves by modifying the global horizontal stiffness for different values of h, with $b = 0.01$m. The red dashed line is a physical reference, which represents the group speed of longitudinal waves in a local beam, dictated by $\sqrt{E/\rho}$.

5.4 Continuity material concept

Figure 5.17 depicts the progressive evolution of the geometric perturbation. The left part coresponds to the beam theory model and the right part shows its plane strain equivalent. In each case a ray representing an incident plane wave front is shown by the double-headed arrow. Depending upon the value of the parameter h the ray path migth appear interrupted. This is indicated by the green (continous) and red (interrupted) dots in each figure. The concept of material continuity is defined as follows: *If in a specific direction a ray can find a continuous propagation path, the material is continuous in that direction. If on the contrary such path does not exist, the material is discontinuous in that direction.* As an additional observation to differentiate both models note that while the plane strain model allows for in-plane particle motions the beam model does not. Notice also that in the beam model the smallest perturbation along the propagation path interrupts material continuity.

5.4.1 Beam model vs Solid model

In the beam theory model the geometric parameters do not have a direct effect in a given domain since A and I only appear in the mathematical formulation. This is

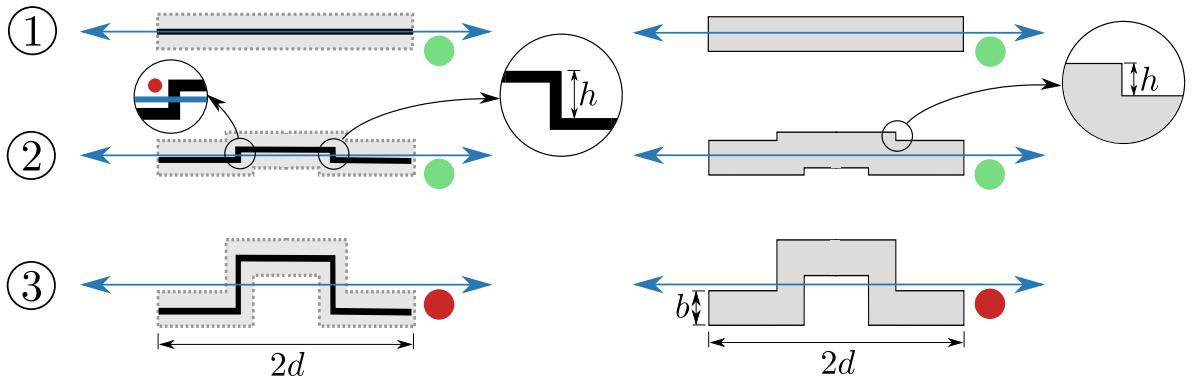

Figure 5.17. Definition and illustration of the continuity material concept. Green and red circles represent continuous and discontinuous paths of propagation respectively. Left: Beam model. The black solid line is the actual beam domain while the gray dashed line represent the virtual domain defined by the cross-sectional properties. Right: Plane strain model. In all cases the unit cell has dimensions $2d = 1\text{m}$ and $b = 0.01\text{m}$.

illustrated in fig. 5.17(left) by the black solid lines. In the same figure the plane strain equivalent is described by the gray representation of the cross section surrounding those beams. Similarly fig. 5.17(right) shows three different domains represented with plane strain.

Figure 5.18 shows the band diagrams for the periodic material explicitly using beam elements for 3 different values of the perturbation parameter h. Cases 1 and 2 correspond to $h = 0$ (no perturbation) and $h = b/5$. In these case the perturbation parameter does not interrupt the propagation path and the band diagram is complete. By contrast, case 3 which exhibits an interruption in the propagation path contains several band gaps (shown by he gray rectangles). Figure 5.19 shows equivalent results for the solid (plane strain) model.

From a physical point of view, a material discontinuity interrupts the natural propagation of a P wave through the material. Moreover in P waves, the directions of propagation and polarization are aligned and a material discontinuity prevents the flow of momentum through the particles. This implies the general result that material discontinuities generate band gaps by interrupting the propagation paths of P waves.

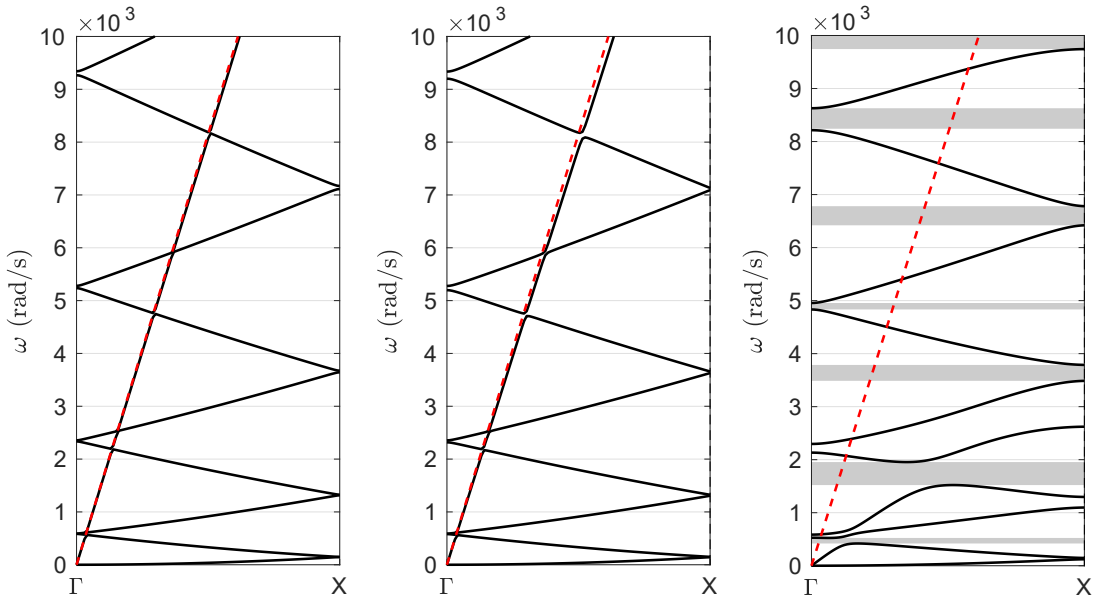

(a) $h = 0.0$ (b) $h = b/5$ (c) $h = 5b$

Figure 5.18. Material continuity concept under a beam model. The red dashed line is a physical reference, which represents the group speed of longitudinal waves in a local beam, dictated by $\sqrt{E/\rho}$. (a) (b) and (c) correspond to cases 1, 2 and 3 respectively.

The results from the beam theory and the plane strain model are highly similar with the only difference corresponding to the frequency values for the S waves. This is explained in terms of the differences in phase velocities between both models. In beam theory longitudinal waves propagate at $\alpha^2 = E/\rho$ while in the plane strain model the phase velocity is $\alpha^2 = E(1-\nu)/(\rho(1+\nu)(1-2\nu))$. Now for the cases shown in fig. 5.19a-b, the plain strain model captures the dispersive behavior of S waves, which demonstrates that a beam can be modelled with a plain strain model. However, this can be done only for low values of $b/2d$, since plain strain does not include a rotational mode of deformation in its kinematics. For thin structures like the beams and frames studied in this chapter a beam model is more suitable, because it is more efficient than a plane strain analysis from a computational point of view.

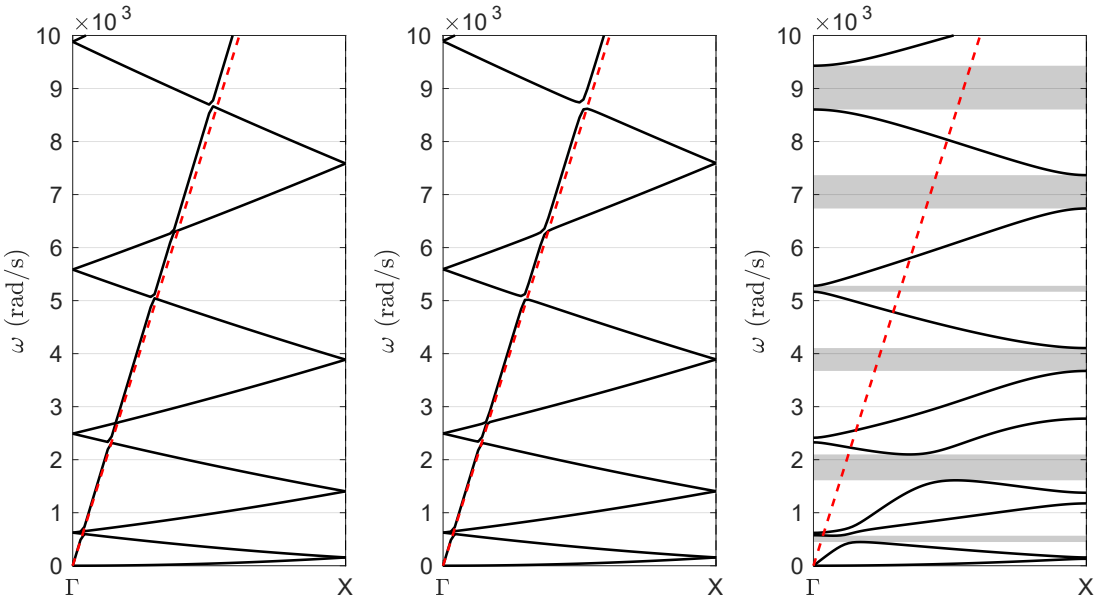

(a) $h = 0.0$ (b) $h = b/5$ (c) $h = 5b$

Figure 5.19. Material continuity concept under a plane strain model. The red dashed line is a physical reference, which represents the group speed of longitudinal waves in a local beam, dictated by $\sqrt{E/\rho}$. (a) (b) and (c) correspond to cases 1, 2 and 3 respectively.

5.4.2 A complex geometry using Plane strain

The 2D periodic material shown in fig. 5.20 was analyzed in order to test the concept of material continuity. The material is conformed by Chakana-shaped unit cells with a variable-sized squared pore as the base geometry. Depending on the size of the pore, the unit cell has material discontinuities along the vertical and horizontal directions. Stages 1-3, where $h_c < t_c$, exhibits continuity in both directions. On the contrary, when h_c becomes larger than t_c the propagation paths are interrupted and the material becomes discontinuous in both directions.

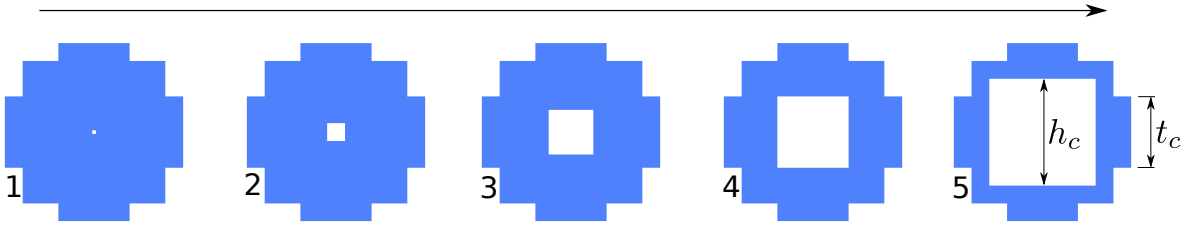

$h_c = t_c/20$ $h_c = 0.25t_c$ $h_c = 0.6t_c$ $h_c = t_c$ $h_c = 1.5t_c$

Figure 5.20. Sequence of the inclusion to illustrate the continuity material concept. Stages 4 and 5 has material discontinuities in horizontal and vertical directions.

According to the concept of material continuity more band gaps are expected in stages 4 and 5 than in stages 1 to 3. Figures 5.21 and 5.22 show the dispersion results along the IBZ for each considered unit cell. There are band gaps only in stages 4 and 5. Furthermore, the band gap of stage 5 is larger than that of stage 4. This is attributed to the size of the pore. Due to the pore shape, it generates material discontinuities in all directions in stages 4 and 5. Note that the band gaps are omnidirectional, which means waves in that frequency band can not propagate in any direction through the material. This is also consistent with the omnidirectional nature of the material discontinuity.

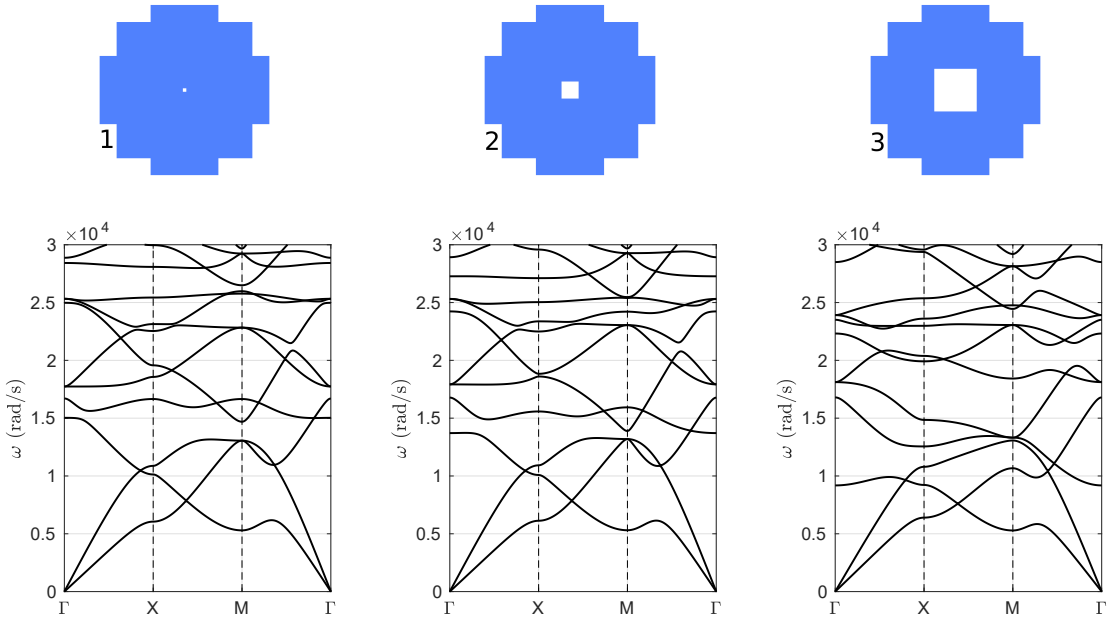

Figure 5.21. Progressive construction to evaluate the material continuity concept. Stages 1-3. Each frame contains the unit cell and its dispersion relations.

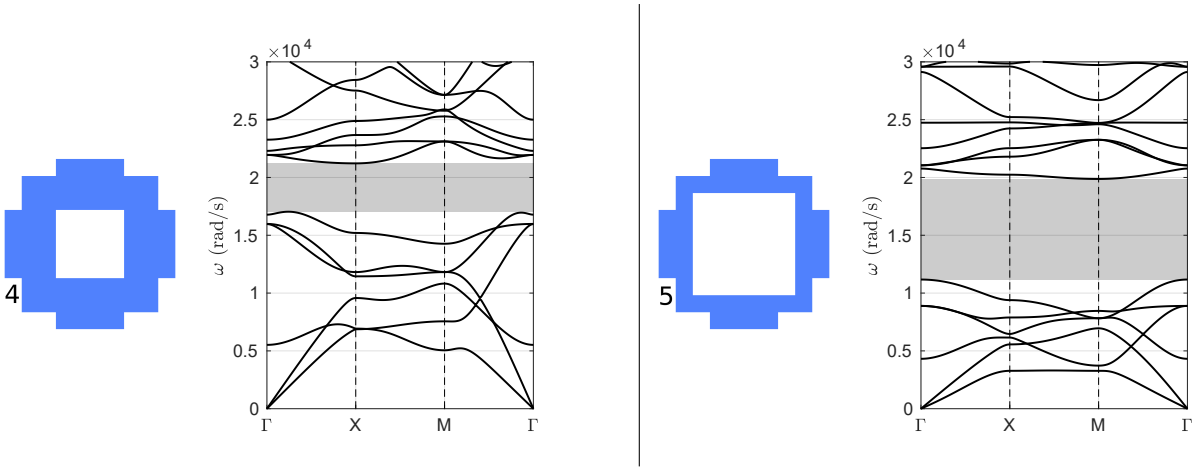

Figure 5.22. Progressive construction to evaluate the material continuity concept. Stages 4 and 5. Continuation of fig. 5.21.

As shown above, the probability of having band gaps in a periodic material is increased by the presence of material discontinuities. However there is no specific recipe to fine tunning the band gap.

5.5 A resonance band gap

The alternative of controlling the band structure of the periodic material through a material discontinuity is now revisited. In particular, a second element is added to the softening mechanism of size h as shown in fig. 5.23. The idea behid this element is to explore resonance as a mechaism to introduce band gaps. This concept has already been explored by Liu et al. (2000); Celli & Gonella (2015). In the current unit cell, the additional element connected to the frame through the softening mechanism is partially decoupled from the rest of the cell. In what follows this extra blue element is termed the resonance beam (RB). Now, conisdering the RB as a fixed-fixed element it is now possible to compute its fundamental frequency as (Blevins, 1979)

$$\omega_b = \left(\frac{3\pi}{2L}\right)^2 \sqrt{\frac{EI}{\rho A}}. \tag{5.14}$$

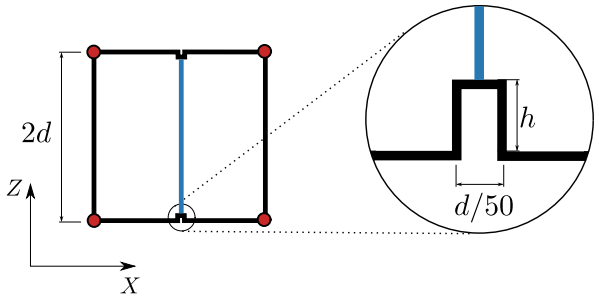

Figure 5.23. Frame with a material discontinuity and a resonant beam drawn in blue. For the analysis in this section, a value $h = 0.1$ was used.

Equation (5.14) is a closed-form expression relating material and geometric properties to the natural frequency of the beam. Although the expression is intended to predict the frequency location of a resonance band gap its most interesting application is when it is used to obtain the geometric properties of the resonant beam having a predefined frequency and a specific building material. Bloch analysis of the unit cell shown in fig. 5.23 is performed in order to verify the predictive capabilities of this expression. The unit cell has a characteristic dimension $2d = 1$m and it is made of beams with a rectangular cross section of height $b = 0.01$m. Here ρ_b denotes the mass density of the resonant beam while ρ is the density of the rest of the unit cell. The dispersion relations for various values of the parameter $\bar{\rho} = \rho_b/\rho$ are shown in fig. 5.24 where the results from applying eq. (5.14) to the resonant beam are plotted as a red dashed line. For $\bar{\rho} = 2.0$, the resonance band gap is located at $\omega = [347, 446]$ rad/s and the frequency of the resonant beam is $\omega_b = 364$ rad/s; moreover, the red line is inside the resonance band gap for all values of $\bar{\rho}$. On the other hand, the global modal shape located at the frequency of the band gap always shows the resonant beam vibrating with the first

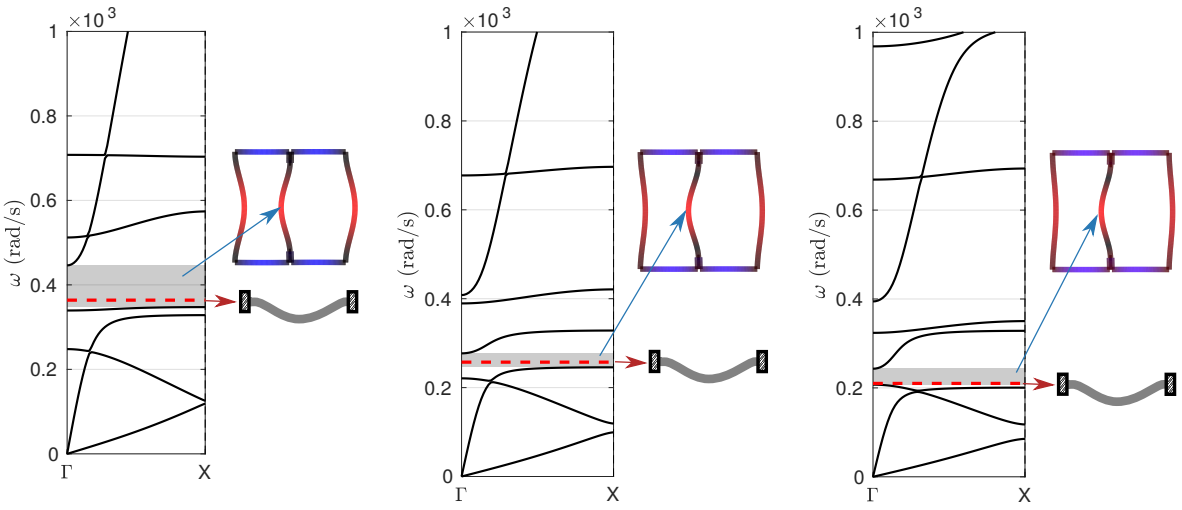

(a) $\bar{\rho} = 2.0$ (b) $\bar{\rho} = 4.0$ (c) $\bar{\rho} = 6.0$

Figure 5.24. Tuning of the resonance band gap. For each value of $\bar{\rho}$, the global vibration mode associated to the frequency of the band gap is shown. That mode always have the vertical beam vibrating with the first local modal shape. The red dotted line, plotted at the frequency calculated with eq. (5.14), is always inside the resonance band gap.

local modal shape. The global natural frequencies and the location of the resonant band gap decrease when $\bar{\rho}$ increases. These results show how the first natural vibration mode of the resonant beam can be used to tune the resonance band gap of the full unit cell.

The most appealing feature of eq. (5.14) is the possibility of obtaining the geometric properties of a resonant beam having a predefined frequency. This can be used to create fine-tuned mechanical filters based on periodic structures. In that case, the resonant beam interacts with a potential incident wave and its mechanical energy will be dissipated by resonance. Depending on the application, different ranges of frequencies are required and the resonant beams should have practical sizes and weights. Figure 5.25 presents a frequency-and-sizes analysis for resonant beams made of different engineering materials. For each material with known values of properties E and ρ, we plotted $\omega_b = \omega_b(L, b)$; where L is the length of a potential beam and b is the height of its rectangular cross section. The black lines in the plot are iso-frequency lines with its frequency value plotted in red. This series of plots is useful to have an idea of the size of a resonant beam, depending on the chosen material and the required frequency to tune the resonance band gap. For instance, if one needs a resonant beam tuned at $\omega_b = 1000$Hz, it can be achieved with a beam made of concrete with $L = 0.2$m and $b = 1$cm; or a beam made of wood with $L = 0.1$m and $b = 1$cm. Finally, the mass of the beam is determined after choosing a width for the cross section. The design has to be made considering that massive beams dissipate more energy than light beams. Another design aspect is the number of unit cells conforming the periodic structure; having in mind that larger dissipation levels are achieved as more unit cells are included. This

was illustrated in chapter 4.

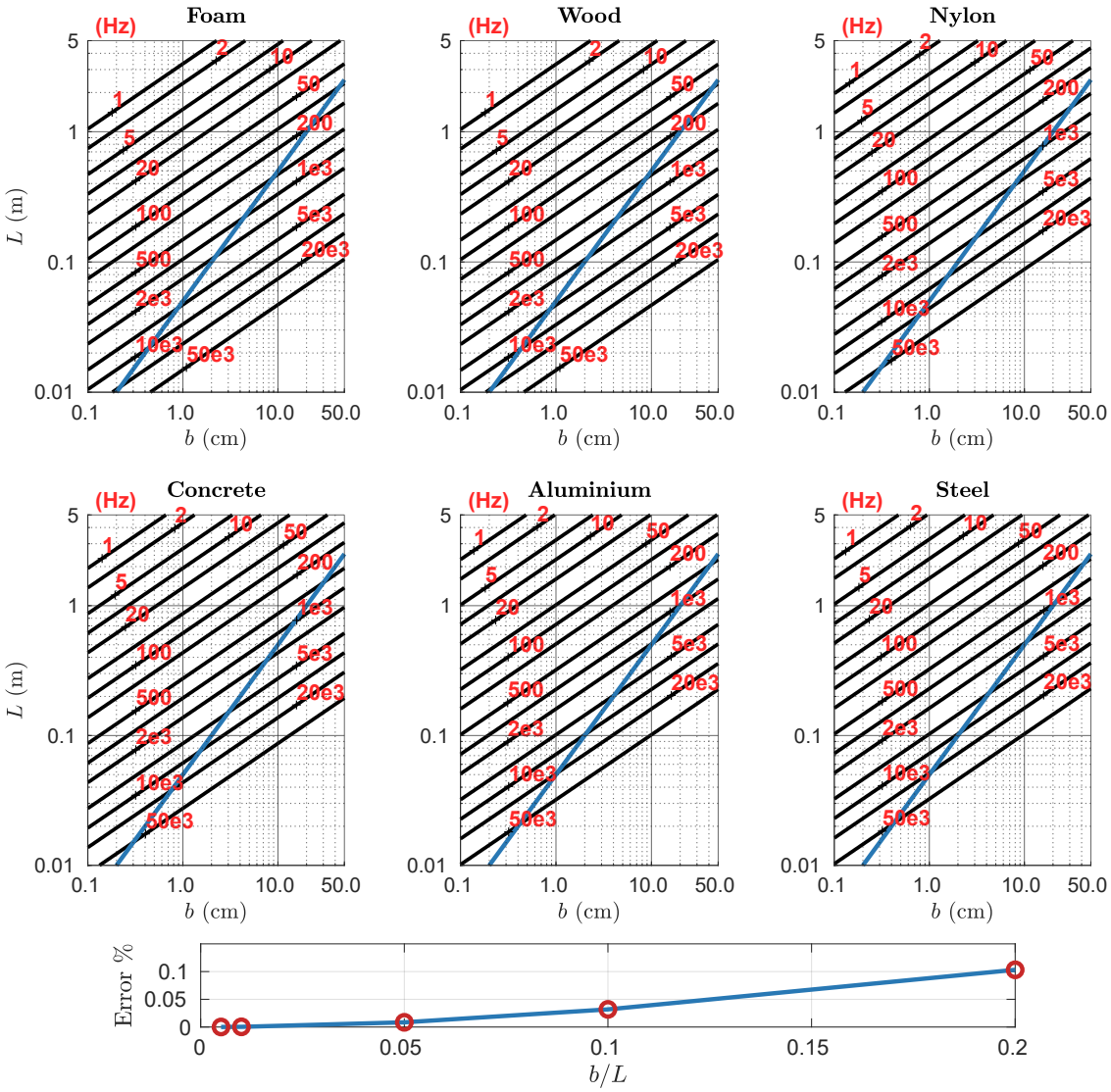

Figure 5.25. First natural frequencies calculated with eq. (5.14) for different materials. Since E and ρ have fixed values, $\omega_b = \omega_b(L, b)$ is plotted as a contour plot. For each material: the black lines are iso-frequency lines at the frequency shown in red. The blue line marks a limit for the slenderness ratio $b/L = 0.2$; below that blue line, the results are not reliable. Note that the plots are in log-log scale. All frequencies shown in Hz. Last row shows the relative error for the first natural frequency when comparing Euler-Bernoulli and Timoshenko theories for different slenderness ratios. Values computed with the first row of table A.1.

For specific applications like seismic engineering, the idea of protecting a building with periodic materials is very attractive. The design objective is to dissipate the energy coming from a seismic event ($\approx$ 10Hz) using a periodic structure below the building with a band gap around 10Hz. The plot for concrete in fig. 5.25, suggests that a resonant

beam tuned at 10Hz can be accomplished with $L = 4$m and $b = 5$cm.

Conclusion

Some fundamental concepts about the relation between the properties of a unit cell and its band structure were discussed. To that end, we used results from simple cases to explain the dispersive phenomena in more complex unit cells. First, a beam model was used due to its simplicity and analytical robustness. Later, the results for a single beam were extended to two dimensional periodic materials whose base elements were beams.

It was shown how the geometric parameters of the cross section affect bending and rotational waves only. By contrast the phase velocity of longitudinal waves depends only upon the material properties. For waves propagating through a 2D periodic material-composed by beams, it is possible to modify the group speed of global S and P waves by varying the stiffness of the material along transverse and longitudinal directions respectively. These waves can be modified independently by introducing geometric changes that affect the stiffness along one specific direction at a time. The group speed of S waves also modified by changing the cross-sectional area of the beams conforming the 2D periodic material; while group speed of P waves was modified by interrupting the continuity of the material along the longitudinal direction of the beams. The interruption of material, which cut the continuous propagation path for the P waves, allowed us to introduce the concept of material discontinuity as a tool to increase the presence of band gaps in a periodic material. A material discontinuity drops the group speed of P waves, in that case it is more probable to have band gaps in the direction where the discontinuity was introduced.

Finally, we were able to fine-tune a resonance band gap to a predefined frequency. The tuning was made through the first transversal natural frequency of a resonant beam. In order to locate a resonant band gap in a unit cell made of beams, transverse displacements have to be induced in the resonant beam. For instance, on the presented unit cell the neutral axis of the resonant beam was perpendicular to the direction of propagation (ΓX) of incident waves. This strategy is general for unit cells having two characteristics: (i) material discontinuities to drop the group speed of P waves and to increase the probabilities of having band gaps and (ii) resonant elements in which the modal frequencies can be analytically calculated.

Concluding remarks

This chapter encloses the results from all the previous chapters in a general conclusion. For specific and technical conclusions about the topics treated in the present work, please go to the conclusion section of each chapter.

The present work treated theoretical, numerical and conceptual aspects of Bloch analysis. In the first chapter, Bloch analysis was introduced and explained in a simple way. The main point there, was the illustration of the spatial aliasing present in Bloch analysis; which its intrinsic symmetry was used later in the directionality approach. After that, it was shown how to perform Bloch analysis in the finite element method (FEM). During the process of applying Bloch boundary conditions in FEM we identified some difficult challenges to deal with; that is why we proposed a novel strategy to compute dispersion relations in commercial –or available– finite element software. The new approach is general enough to deal with different mesh dimensions, kinematics and material models. An example of its versatility is shown in all the different elements implemented for the realization of this work. We implemented: (i) 1D Timoshenko beams and (ii) 2D Solid elements with anti-plane, in-plane and micropolar kinematic models. The implemented elements allowed us to analyse an important number of cases in short calculation times.

Up to that point, we had some theoretical background about Bloch analysis and an efficient way to calculate a band structure in FEM. The next challenge we found, was related to the interpretation of that band structure. We decided to go to the simple by making a conceptual study held with analytical and simple cases, which spanned from the analysis of a single one dimensional beam to a proposal to fine-tune a bang gap in a two dimensional material made of beams. During the conceptual study, three main aspects were treated: (i) the modulation of group speed of S and P waves, (ii) the concept of material continuity and (iii) the role of natural vibration modes in the dispersive behavior of a periodic material. Those concepts were studied using a Timoshenko beam model, but it was shown that they can be applied to solid domains as well.

Finally, in the case of study that we chose, all the concepts and numerical tools developed in this work were applied. For the Bloch analysis of the PXCM and the progressive construction of the unit cell, we used the strategy proposed in chapter 2. The concepts of modulation of group speed in beams and material continuity, studied in chapter 5, were used in the progressive construction of the PXCM unit cell in open configuration.

Even if the PXCM was analysed with a solid discretization, the reasoning used to fine-tune the resonant band gap was the same as in the beam case. Also, the directionality analysis was made with the new approach presented in chapter 3. The directional behavior presented for the homogeneous case and for the progressive construction of the PXCM unit cell, showed that the new approach describes the directional properties of the material in a very intuitive way. Furthermore, the results from the new metrics of directionality support the concept of material continuity. This new concept can be extended to a more general concept of *energetic paths* in a material. In the results shown in this work, it can be seen how the directions of material continuity and the preferred directions of propagation are always highly correlated.

Several ideas were born during the realization of the present work. Some of them seem highly promising and an additional effort should be made to develop them. One of them is the idea of making periodic structures to protect a building from a seismic event, presented in chapter 5. Currently, some studies have been made to find periodic materials with band gaps in very low frequencies (10Hz). The main practical limitations for such periodic materials is the size of the unit cells. Further work is required in order to reduce the size of a potential unit cell or to find practical applications using such large dimensions. Another idea that deserves a deeper study is the new directionality metrics and its relation with the concept of material continuity. With a combination of those concepts and anisotropy factors reported in literature, the directionality approach could become a quantitative tool to measure the distribution of energy along continuous and discontinuous propagation paths in a periodic material.

References

Åberg, M. & Gudmundson, P., 1997. The usage of standard finite element codes for computation of dispersion relations in materials with periodic microstructure, *The Journal of the Acoustical Society of America*, **102**(4), 2007–2013.

Achenbach, J., 2012. *Wave propagation in elastic solids*, vol. 16, Elsevier.

Auld, B. A., 1973. *Acoustic fields and waves in solids*, John Wiley & Sons.

Banerjee, B., 2011. *An Introduction to Metamaterials and Waves in Composites*, CRC Press.

Blevins, R. D., 1979. *Formulas for natural frequency and mode shape / Robert D. Blevins*, Van Nostrand Reinhold Co New York.

Bloch, F., 1929. Über die quantenmechanik der elektronen in kristallgittern, *Zeitschrift für physik*, **52**(7-8), 555–600.

Brillouin, L., 1953. *Wave propagation in periodic structures*, NY: Dover.

Casadei, F. & Rimoli, J., 2013. Anisotropy-induced broadband stress wave steering in periodic lattices, *International Journal of Solids and Structures*, **50**(9), 1402–1414.

Celli, P. & Gonella, S., 2015. Manipulating waves with LEGO® bricks: A versatile experimental platform for metamaterial architectures, *Applied Physics Letters*, **107**(8), 081901.

Correa, D. M., Klatt, T., Cortes, S., Haberman, M., Kovar, D., & Seepersad, C., 2015. Negative stiffness honeycombs for recoverable shock isolation, *Rapid Prototyping Journal*, **21**(2), 193–200.

Cosserat, E., Cosserat, F., et al., 1909. Théorie des corps déformables.

Cowper, G., 1966. The shear coefficient in timoshenko's beam theory, *Journal of applied mechanics*, **33**(2), 335–340.

Craster, R., Antonakakis, T., Makwana, M., & Guenneau, S., 2012. Dangers of using the edges of the brillouin zone, *Physical Review B*, **86**(11), 115130.

Debeau, D. A., Seepersad, C. C., & Haberman, M. R., 2018. Impact behavior of negative stiffness honeycomb materials, *Journal of Materials Research*, **33**(3), 290–299.

Ferreira, A. J., 2008. *MATLAB codes for finite element analysis: solids and structures*, vol. 157, Springer Science & Business Media.

Frazier, M. J. & Kochmann, D. M., 2017. Band gap transmission in periodic bistable mechanical systems, *Journal of Sound and Vibration*, **388**, 315–326.

Friedman, Z. & Kosmatka, J. B., 1993. An improved two-node timoshenko beam finite element, *Computers & structures*, **47**(3), 473–481.

Goldsberry, B. M. & Haberman, M. R., 2018. Negative stiffness honeycombs as tunable elastic metamaterials, *Journal of Applied Physics*, **123**(9), 091711.

Gonella, S. & Ruzzene, M., 2008. Analysis of in-plane wave propagation in hexagonal and re-entrant lattices, *Journal of Sound and Vibration*, **312**(1-2), 125–139.

Graff, K. F., 1976. *Wave motion in elastic solids*, Dover publications, INC.

Guarín-Zapata, N. & Gomez, J., 2014. Evaluation of the spectral finite element method with the theory of phononic crystals, *Journal of Computational Acoustics*.

Gupta, G. S., 1970. Natural flexural waves and the normal modes of periodically-supported beams and plates, *Journal of Sound and Vibration*, **13**(1), 89–101.

Haghpanah, B., Salari-Sharif, L., Pourrajab, P., Hopkins, J., & Valdevit, L., 2016. Multistable shape-reconfigurable architected materials, *Advanced Materials*, **28**(36), 7915–7920.

Han, S. M., Benaroya, H., & Wei, T., 1999. Dynamics of transversely vibrating beams using four engineering theories, *Journal of Sound and vibration*, **225**(5), 935–988.

Haque, A. T. & Shim, J., 2016. On spatial aliasing in the phononic band-structure of layered composites, *International Journal of Solids and Structures*, **96**, 380–392.

Harrison, J., Kuchment, P., Sobolev, A., & Winn, B., 2007. On occurrence of spectral edges for periodic operators inside the brillouin zone, *Journal of Physics A: Mathematical and Theoretical*, **40**(27), 7597.

Heckl, M. A., 1964. Investigations on the vibrations of grillages and other simple beam structures, *The Journal of the Acoustical Society of America*, **36**(7), 1335–1343.

Hibbett, Karlsson, & Sorensen, 1998. *ABAQUS/standard: User's Manual*, vol. 1, Hibbitt, Karlsson & Sorensen.

Hiett, B., Generowicz, J., Cox, S., Molinari, M., Beckett, D., & Thomas, K., 2002. Application of finite element methods to photonic crystal modelling, *IEE Proceedings-Science, Measurement and Technology*, **149**(5), 293–296.

Howell, L. L., 2001. *Compliant mechanisms*, John Wiley & Sons.

Howell, L. L., Rao, S., & Midha, A., 1994. Reliability-based optimal design of a bistable compliant mechanism, *Journal of Mechanical Design*, **116**(4), 1115–1121.

Huang, T., 1961. The effect of rotatory inertia and of shear deformation on the frequency and normal mode equations of uniform beams with simple end conditions, *Journal of Applied Mechanics*, **28**(4), 579–584.

Hussein, M. I., Leamy, M. J., & Ruzzene, M., 2014a. Dynamics of phononic materials and structures: Historical origins, recent progress, and future outlook, *Applied Mechanics Reviews*, **66**(4), 040802.

Hussein, M. I., Leamy, M. J., & Ruzzene, M., 2014b. Dynamics of phononic materials and structures: Historical origins, recent progress, and future outlook, *Applied Mechanics Reviews*, **66**(4), 040802.

Johnson, S. G., 2010. Notes on the algebraic structure of wave equations, Tech. rep., Massachusetts Institute of Technology.

Kadic, M., Bückmann, T., Schittny, R., & Wegener, M., 2013. Metamaterials beyond electromagnetism, *Reports on Progress in physics*, **76**(12), 126501.

Kittel, C. et al., 1976. *Introduction to solid state physics*, vol. 8, Wiley New York.

Kocatürk, T. & Şimşek, M., 2005. Free vibration analysis of timoshenko beams under various boundary conditions, *Sigma*, **1**, 30–44.

Kreyszig, E., 1978. *Introductory functional analysis with applications*, vol. 1, wiley New York.

Langlet, P., 1993. *Analyse de la propagation des ondes acoustiques dans les matériaux périodiques à l'aide de la méthode des éléments finis*, Ph.D. thesis, Valenciennes.

Langlet, P., Hladky-Hennion, A.-C., & Decarpigny, J.-N., 1995. Analysis of the propagation of plane acoustic waves in passive periodic materials using the finite element method, *The Journal of the Acoustical Society of America*, **98**(5), 2792–2800.

Langley, R., Bardell, N., & Ruivo, H., 1997. The response of two-dimensional periodic structures to harmonic point loading: a theoretical and experimental study of a beam grillage, *Journal of Sound and Vibration*, **207**(4), 521–535.

Lee, J. & Schultz, W., 2004. Eigenvalue analysis of timoshenko beams and axisymmetric mindlin plates by the pseudospectral method, *Journal of Sound and Vibration*, **269**(3-5), 609–621.

Leroy, V., Strybulevych, A., Lanoy, M., Lemoult, F., Tourin, A., & Page, J. H., 2015. Superabsorption of acoustic waves with bubble metascreens, *Physical Review B*, **91**(2), 020301.

Lin, Y.-K. & McDaniel, T., 1969. Dynamics of beam-type periodic structures, *Journal of Engineering for Industry*, **91**(4), 1133–1141.

Liu, L. & Hussein, M. I., 2012. Wave motion in periodic flexural beams and characterization of the transition between bragg scattering and local resonance, *Journal of Applied Mechanics*, **79**(1), 011003.

Liu, Z., Zhang, X., Mao, Y., Zhu, Y., Yang, Z., Chan, C. T., & Sheng, P., 2000. Locally resonant sonic materials, *science*, **289**(5485), 1734–1736.

Lu, M.-H., Feng, L., & Chen, Y.-F., 2009. Phononic crystals and acoustic metamaterials, *Materials today*, **12**(12), 34–42.

Maurin, F., Claeys, C., Deckers, E., & Desmet, W., 2018. Probability that a band-gap extremum is located on the irreducible brillouin-zone contour for the 17 different plane crystallographic lattices, *International Journal of Solids and Structures*, **135**, 26–36.

Mazzoni, S., McKenna, F., Scott, M. H., Fenves, G. L., et al., 2006. Opensees command language manual, *Pacific Earthquake Engineering Research (PEER) Center*, **264**.

McGrath, D. T. & Pyati, V. P., 1994. Phased array antenna analysis with the hybrid finite element method, *Antennas and Propagation, IEEE Transactions on*, **42**(12), 1625–1630.

McGrath, D. T. & Pyati, V. P., 1996. Periodic structure analysis using a hybrid finite element method, *Radio Science*, **31**(5), 1173–1179.

Meaud, J. & Che, K., 2017. Tuning elastic wave propagation in multistable architected materials, *International Journal of Solids and Structures*, **122**, 69–80.

Michel, J., Moulinec, H., & Suquet, P., 1999. Effective properties of composite materials with periodic microstructure: a computational approach, *Computer methods in applied mechanics and engineering*, **172**(1), 109–143.

Mousanezhad, D., Babaee, S., Ghosh, R., Mahdi, E., Bertoldi, K., & Vaziri, A., 2015. Honeycomb phononic crystals with self-similar hierarchy, *Physical Review B*, **92**(10), 104304.

Nadkarni, N., Daraio, C., & Kochmann, D. M., 2014. Dynamics of periodic mechanical structures containing bistable elastic elements: From elastic to solitary wave propagation, *Physical Review E*, **90**(2), 023204.

Norris, A. N. & Haberman, M. R., 2012a. Introduction to the special issue on acoustic metamaterials, *The Journal of the Acoustical Society of America*, **132**(4), 2783–2783.

Norris, A. N. & Haberman, M. R., 2012b. Introduction to the special issue on acoustic metamaterials, *The Journal of the Acoustical Society of America*, **132**(4), 2783–2783.

Nowacki, W., 1986. *Theory of asymmetric elasticity*, Pergamon Press, Headington Hill Hall, Oxford OX 3 0 BW, UK.

Pask, J. & Sterne, P., 2005. Finite element methods in ab initio electronic structure calculations, *Modelling and Simulation in Materials Science and Engineering*, **13**(3), R71.

Phani, A. S., Woodhouse, J., & Fleck, N., 2006. Wave propagation in two-dimensional periodic lattices, *The Journal of the Acoustical Society of America*, **119**(4), 1995–2005.

Porter, R. & Porter, D., 2003. Scattered and free waves over periodic beds, *Journal of Fluid Mechanics*, **483**, 129–163.

Przemieniecki, J. S., 1985. *Theory of matrix structural analysis*, Courier Corporation.

Qiu, J., Lang, J. H., & Slocum, A. H., 2004. A curved-beam bistable mechanism, *Journal of microelectromechanical systems*, **13**(2), 137–146.

Reddy, J. N., 1986. *Applied functional analysis and variational methods in engineering*, Mcgraw-Hill College.

Restrepo, D., Mankame, N. D., & Zavattieri, P. D., 2015. Phase transforming cellular materials, *Extreme Mechanics Letters*, **4**, 52–60.

Ruzzene, M. & Scarpa, F., 2005. Directional and band-gap behavior of periodic auxetic lattices, *physica status solidi (b)*, **242**(3), 665–680.

Ruzzene, M., Scarpa, F., & Soranna, F., 2003. Wave beaming effects in two-dimensional cellular structures, *Smart materials and structures*, **12**(3), 363.

Schaeffer, M. & Ruzzene, M., 2015. Wave propagation in multistable magneto-elastic lattices, *International Journal of Solids and Structures*, **56**, 78–95.

Shan, S., Kang, S. H., Raney, J. R., Wang, P., Fang, L., Candido, F., Lewis, J. A., & Bertoldi, K., 2015. Multistable architected materials for trapping elastic strain energy, *Advanced Materials*, **27**(29), 4296–4301.

Sigalas, M. M. & Economou, E. N., 1992. Elastic and acoustic wave band structure, *Journal of Sound Vibration*, **158**, 377–382.

Sukumar, N. & Pask, J., 2009. Classical and enriched finite element formulations for bloch-periodic boundary conditions, *International Journal for Numerical Methods in Engineering*, **77**(8), 1121–1138.

Taylor, R. L., 2011. *FEAP - A Finite Element Analysis Program, Version 8.3 User Manual*.

Timoshenko, S. P., 1921. Lxvi. on the correction for shear of the differential equation for transverse vibrations of prismatic bars, *The London, Edinburgh, and Dublin Philosophical Magazine and Journal of Science*, **41**(245), 744–746.

Timoshenko, S. P., 1922. X. on the transverse vibrations of bars of uniform cross-section, *The London, Edinburgh, and Dublin Philosophical Magazine and Journal of Science*, **43**(253), 125–131.

Trainiti, G., Rimoli, J. J., & Ruzzene, M., 2016. Wave propagation in undulated structural lattices, *International Journal of Solids and Structures*, **97**, 431–444.

Vangbo, M., 1998. An analytical analysis of a compressed bistable buckled beam, *Sensors and Actuators A: Physical*, **69**(3), 212–216.

Appendices

Appendix A

A.1 Calculation of natural frequencies in Timoskenko beams

In the case of flexural waves, it is not generally possible to obtain a closed form solution to calculate the natural frequencies of a Timoshenko beam (Blevins, 1979). However, several numerical approaches have been developed to that end. See for example Han et al. (1999); Lee & Schultz (2004); Kocatürk & Şimşek (2005); Ferreira (2008). Here we used the approach and the MATLAB subroutines proposed by Ferreira (2008), who solved the problem using finite element analysis. Table A.1 presents the non-dimensional natural frequencies for a fixed-fixed beam with rectangular cross section given by:

$$\beta_i^2 = \omega_i^F \sqrt{\frac{\rho A L^4}{EI}} \tag{A.1}$$

where ω_i^F is the natural frequency of the i-th mode for flexural waves. In this expression L denotes the length of the beam.

Mode	E-B	b/L				
		0.005	0.01	0.05	0.1	0.2
1	4.73004	4.72963	4.7284	4.68991	4.57955	4.24201
2	7.8532	7.85163	7.8469	7.70352	7.33122	6.41794
3	10.9956	10.9917	10.9800	10.6401	9.85611	8.28532
4	14.1372	14.1294	14.1062	13.4611	12.1454	9.90372
5	17.2788	17.2651	17.2246	16.159	14.2324	11.3487
6	20.4204	20.3985	20.3338	18.7318	16.1487	2.6402
7	23.5619	23.5292	23.4325	21.1825	17.9215	13.4567

Table A.1. β values for the first 7 modes of a fixed-fixed beam for different slenderness ratios b/L. The second column correspond to natural frequencies calculated using classic Euler-Bernoulli theory.

The results listed in table A.1 show that the Timoshenko beam results are very close

to the Bernoulli–Euler results when b/L is less than 0.01. As b/L gets larger, the calculated values show significant differences from the Euler-Bernoulli results; showing larger difference for high frequency modes. For instance, for $b/L = 0.2$, the relative difference for mode 1 is 10%; while it reaches 40% for mode 7. On the other hand, for longitudinal waves in a fixed-fixed beam, natural frequencies can be calculated using the exact expression (Blevins, 1979)

$$\omega_i^L = i\frac{\pi}{L}\sqrt{\frac{E}{\rho}}, \tag{A.2}$$

where the superscript L in ω_i^L means longitudinal. It must not be confused with the length of the beam L.